1996

Improving Dose Calculations In Electron-beam Radiation Therapy

John McLellan

Improving Dose Calculations in Electron-Beam Radiation Therapy

by

John McLellan

Department of Medical Biophysics

Submitted
in Partial Fulfilment of the Requirements
for the Degree of

DOCTOR OF PHILOSOPHY

Faculty of Graduate Studies
The University of Western Ontario
London, Ontario
March 1996

ISBN 0-612-15069-0

Abstract

The finite range of electrons in tissue makes electron beams a useful radiation treatment modality for many tumour sites. However, the simplistic methods of dose calculation in current clinical use lack sufficient accuracy in many situations of clinical importance. This thesis rests on the premise that a more accurate dose calculation method must incorporate all the major physical processes which shape the dose distribution.

The thesis unites the important transport processes of electron energy loss and angular scattering in a single mathematical model known as the compound Poisson process (CPP). CPP-based calculations of energy-loss spectra for 10, 20 and 30 MeV electrons incident on graphite and aluminum absorbers agreed within 1% with Monte Carlo simulations for electrons travelling path lengths less than 0.5 g/cm^2. Similarly, calculations of angular distributions agreed with Monte Carlo simulations within 2% for 5 and 10 MeV electrons traversing water slabs up to 0.5 cm thick.

The evolution and Monte Carlo methods of dose calculation can both incorporate the CPP model into a complete transport calculation. An analysis of the convergence of the two methods reveals that: (i) the number of histories in a Monte Carlo simulation is analogous to the number of discrete bins in the evolution method, (ii) the convergence of the evolution method depends on the dimensionality of the problem while the convergence of the Monte Carlo method does not, and (iii) for the full six dimensional transport problem, the ratio of the error in the evolution method to that in the Monte Carlo method is proportional to $N^{1/6}$ where N is the number of histories or bins.

Since the convergence of the evolution method improves with fewer dimensions, an approximate "dimensionally-reduced" evolution method is proposed. Preliminary calculations of dose distributions in a homogeneous water phantom achieved reasonable agreement with Monte Carlo simulations for incident 10 and 20 MeV electron beams. The least accurate result underestimated the dose by 5% at the depth of dose maximum and overestimated the width of the 10% isodose line by 8 mm. These early results indicate that the dimensionally-reduced evolution method merits further investigation.

Keywords: Radiation Therapy, Electron Beams, Energy-Loss, Angular Scattering, Compound Poisson Process, Phase Space Evolution, Monte Carlo

Acknowledgements

The work presented here was carried out at the London Regional Cancer Centre of the Ontario Cancer Treatment and Research Foundation. Financial support was received from the National Cancer Institute, the Medical Research Council of Canada and the University of Western Ontario. I would like to sincerely thank our collaborators at the University of Indiana Medical School, Dr. Lech Papiez and Dr. George Sandison.

Of course this work would not have been possible without the wise and patient guidance of my supervisor, Prof. Jerry Battista. Sage advice was also offered by the members of my advisory committee, Dr. Froelich, Dr. Cunningham and Dr. Taylor.

I would also like to thank my fellow graduate students at the London Regional Cancer Centre for stimulating discussions and plenty of lunch-time entertainment.

Lastly (and most importantly), I would like to thank my wife, Yvonne, for her patience and encouragement. Without her, I never would have finished this *magnum opus*.

Table of Contents

List of Figures

Chapter 1. Introduction

1.1 The Radiation Therapy Problem

1.1.1 The Use of Radiation in Cancer Treatment

Radiation therapy aims to maximize the radiation dose to malignant tissues while keeping the dose to normal tissues within tolerance limits. Although the probability of controlling a tumour increases with increasing dose, the potential for side effects also increases due to damage to near-by normal tissues (Emami et al., 1991). Therefore, the radiation oncologist must weigh the increased likelihood of tumour control against the increased risk of side effects. A judgement of the quality of a proposed treatment thus requires an accurate knowledge of the distribution of radiation dose within all the exposed tissues as well as radiobiological data on the radiation sensitivity of the tissues.

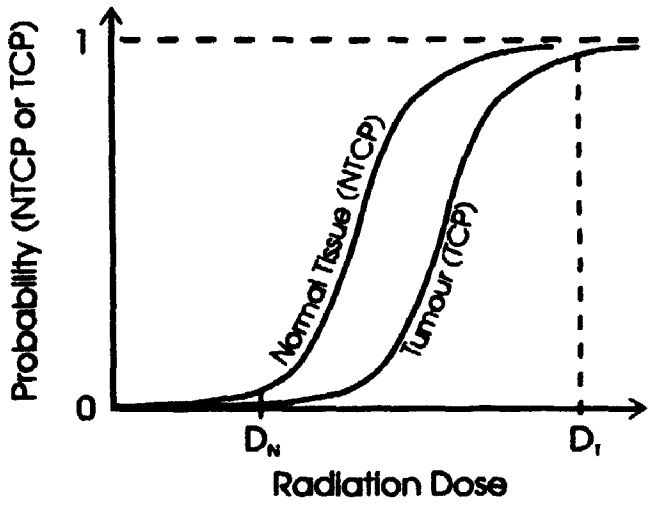

Figure 1-1: Typical Dose Response Curves

The vertical axis represents the probability of a given effect while the horizontal axis represents the dose delivered. The goal of radiation therapy is to deliver a large tumour dose (D_T) while maintaining a reduced dose to normal tissues (D_N).

A typical "dose response curve" is shown in Figure 1-1. The curve represents the probability of observing a radiobiological effect (*eg* killing all the cells in a tumour or

observing a normal tissue complication) as a function of the radiation dose delivered. Typically, on the steep portion of the curve, a 1% change of dose can lead to a 5% change in either the normal tissue complication probability (NTCP) or the tumour control probability (TCP) (Burman et al., 1991). In view of the slope and proximity of the dose response curves, the International Commission on Radiation Units and Measurements (ICRU, 1976) recommends that the overall uncertainty in local dose not exceed 5%. This figure represents a compromise between the above-mentioned radiobiological concerns and the accuracy which is practically achievable in the clinic. To allow for other sources of dose uncertainty in treatment delivery, the error in dose *calculation* should not exceed 3% (see also Brahme, 1984).

Several methods of delivering a radiation dose to the target region are available. These methods fall into one of two general categories: brachytherapy and teletherapy. The first category takes its name from the Greek word, "brachy", meaning "at close range". It involves either the surgical implantation of encapsulated radioactive sources directly into the target region or the injection of a radioactive liquid which preferentially accumulates in the target region. In teletherapy, a target region receives dose from beams of radiation originating some distance (usually about 1 meter) from the patient (hence the use of the Greek word, "tele", meaning "at long range").

Orthovoltage x-ray generators provided the earliest form of teletherapy treatments. However, these types of treatment machines produce photon energies in the range 100 to 200 keV and are useful only for lesions at depths of a few millimetres. Target volumes at larger depths require megavoltage radiation (*ie* energies above 1 MeV).

The use of a cobalt 60 (Co^{60}) source together with a collimating system provides the simplest means of producing a beam of megavoltage photons. The average energy of the photons emitted by Co^{60} is 1.25 MeV giving a depth of penetration (50% dose level) of approximately 10 cm. Although multiple "crossed" beams of Co^{60} photons may be used to treat deep target volumes, the use of higher photon energies can improve the dose distribution due to increased penetration and improved skin sparing.

Higher photon energies necessitate the use of electron accelerators such as betatrons, microtrons (Brahme et al., 1975; Brahme et al., 1980) or linear accelerators

(linacs) (Karzmark et al., 1993). Betatrons and microtrons are "orbital" accelerators which use magnetic fields to constrain the electrons to roughly circular orbits during the acceleration process. Linacs, on the other hand, accelerate electrons in a straight line down a radio-frequency wave-guide. All these accelerators are capable of producing clinically useful beams of x-rays or electrons. In the case of an x-ray beam, the narrow electron beam emerging from the accelerator strikes a thick high-atomic-number target to produce bremsstrahlung photons. An appropriately shaped flattening filter converts the forward-directed bremsstrahlung beam into a clinically-useful beam of uniform intensity. In the case of an electron beam, the x-ray target is removed and the emerging electrons are scanned magnetically or scattered in foils to produce a uniform broad beam. Most radiation therapy facilities have high energy linacs capable of producing both x-ray and electron beams. Thus, Radiation Oncologists have both these treatment modalities at their disposal in the design of an optimal treatment.

1.2 The Role of Electron Beams

1.2.1 Depth Dose Characteristics

Figure 1-2 demonstrates the very different character of electron and photon beam depth dose distributions. Photons interact in a medium relatively infrequently and, as a result, a photon beam depth dose curve exhibits a long exponentially decaying "tail". In contrast, electrons have a well defined range due to **nearly** continuous interactions between the penetrating electrons and the orbital electrons of the scattering medium. Thus, an electron beam depth dose curve falls off rapidly at a distance equal to the range of the penetrating electrons (*eg* 5 cm for the electrons in Figure 1-2). This property of electron beams provides dose distributions which, in many instances, cannot be achieved even with multiple photon beams.

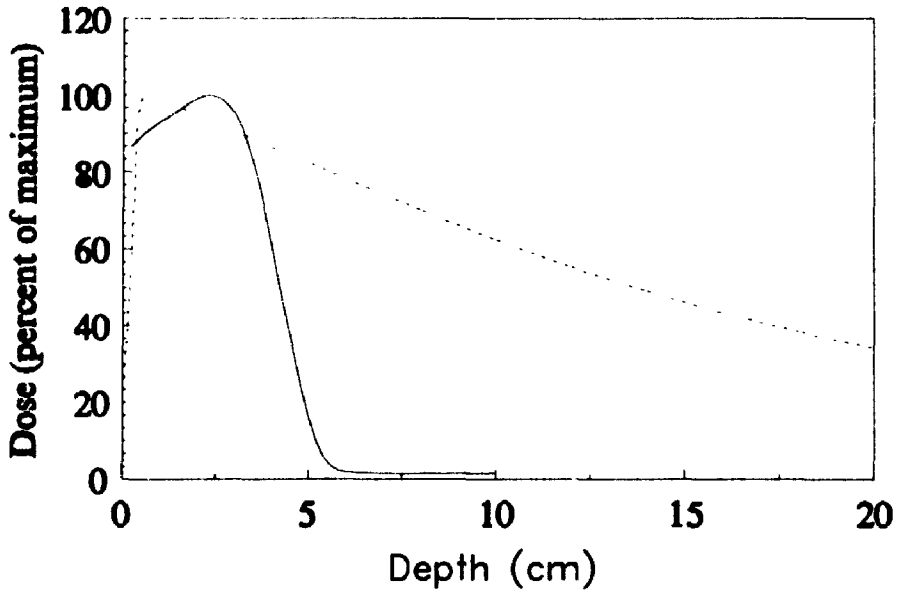

Figure 1-2: Depth Dose Curves for Electrons and Photons

The depth dose distribution of a Co^{60} beam (20x20 cm^2, 100 cm SSD) is compared with that of a broad beam of 10 MeV electrons. The Co^{60} data is from Johns and Cunningham (1983).

1.2.2 Clinical Applications

Using electron beams, tumours close to the skin's surface may be irradiated while deeper normal tissues are spared. This property of electron beams has found application in many tumour sites (Brady et al., 1992). One of the most obvious applications is the irradiation of skin lesions using either small fields for localized tumours or large multiple fields for total skin irradiation. However, tumours of the head and neck, breast, upper respiratory track and digestive passages have also been treated using electron beams. In addition, arc electron beams lend themselves to irradiation of the chest wall in breast cancer. The combination of photon and electron beams is also common. For instance, electron beams may be used to "boost" the dose to the lymph nodes surrounding the breast following photon irradiation for breast cancer.

The use of electron beams is not limited to treatment of "shallow" targets,

however. Gosselin et al. (1993) have developed a technique using high energy (20 MeV) parallel opposed electron beams to irradiate a mass in the mediastinum. Ironically, the authors exploited the angular scattering properties of electrons to shield a structure close to the surface (the spinal cord in this case) while delivering a uniform dose to deeper structures.

1.2.3 Clinical Methods of Dose Calculation

All the clinical uses of electron beams mentioned in Section 1.2.2 necessitate methods of accurately calculating the distribution of radiation dose in the tissues. This section summarizes the various techniques which are currently in clinical use.

Broad Beam Methods

The simplest form of dose calculations, the ray-line method, relies on the assumption that electrons travel in straight lines. Several authors have formulated the ray-line method in different ways with different assumptions (Laughlin, 1965; Boone et al., 1967; Almond et al., 1967; Bagne, 1976) but the basic approach is the same in all instances. The electrons are assumed to travel along ray-lines originating from a single "virtual" source. An appropriate shift of the percentage depth dose curve (as measured for a broad beam in a homogeneous water phantom) along these ray-lines accounts for the effects of inhomogeneities in tissue density.

Dose distributions calculated in this manner reflect neither the lateral scattering of electrons near the edge of inhomogeneities (Shortt et al., 1986; Shiu et al., 1992) nor the back-scattering of electrons at interfaces between media (Werner, 1985). Since these effects lead to considerable dose perturbations (up to 50%, see Shortt et al., 1986), the ray-line method has been largely supplanted by the pencil beam summation method.

Pencil Beam Methods

The pencil beam summation method relies on the fact that radiation transport is a linear process. As shown in Figure 1-3, the method represents a broad beam of electrons as a superposition of elemental "pencil beams". The dose, $D(\mathbf{r})$, at any point,

$\mathbf{r}$, in a medium is the summation of the dose contributions from each pencil beam:

$$D(\mathbf{r}) = \int_S F(\mathbf{r}') \cdot d(\mathbf{r};\mathbf{r}')\, d\mathbf{r}' \qquad (1.1)$$

The superposition integral extends over some specified entrance surface, S, at the patient. The function, $F(\mathbf{r}')$, represents the incident electron beam fluence for each point, $\mathbf{r}'$, on the surface, S. The "kernel" function, $d(\mathbf{r};\mathbf{r}')$, represents the dose contribution to a point, $\mathbf{r}$, in the medium from a pencil beam originating at a point, $\mathbf{r}'$.[1]

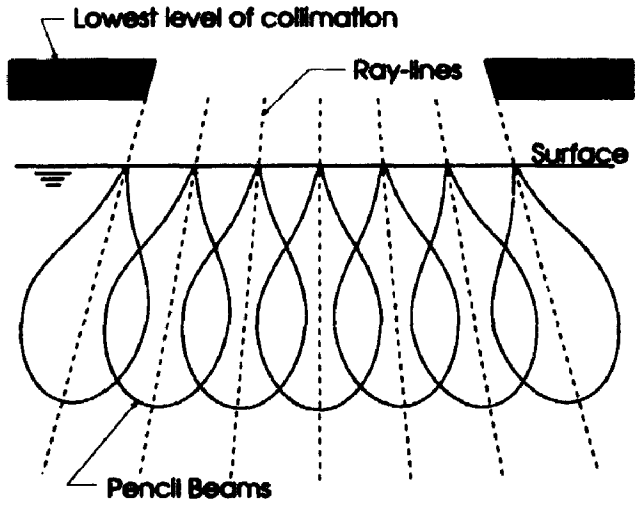

Figure 1-3: Pencil Beam Dose Calculations

The pencil beam summation method of dose calculation treats a broad beam of electrons as if it were composed of an infinite number of individual pencil beams (for practical calculations, the number of pencil beams is finite, but the principle is the same). The figure shows a few representative pencil beams.

Clearly, the shape of a particular pencil beam, $d(\mathbf{r};\mathbf{r}')$, will depend on the energy and angular spread of the incident electrons and the presence of any inhomogeneities near the pencil beam. The various implementations of the pencil beam approach differ in the way they obtain the pencil beam dose distribution and the way the pencil beams are distorted to account for tissue inhomogeneities.

---

[1]This approach to electron beam dose calculations is akin to the superposition method of **photon** beam dose calculations (Mackie, 1987; Battista and Sharpe, 1992).

The idea of using pencil beams to represent a broad beam of electrons is not new. Lillicrap et al. (1975) measured the dose distributions from very narrow beams and used these to reconstruct broad beam distributions. Osman (1976) took a similar approach but used multiple scattering theory to derive the pencil beam dose distributions. However, neither report considered the effects of tissue inhomogeneities.

Monte Carlo simulation (Berger, 1963; Andreo 1991) can also yield accurate pencil beam dose distributions, $d(\mathbf{r};\mathbf{r}')$, for use in the superposition method (Lax et al., 1983; Mackie, 1987; Altschuler et al., 1992). More commonly, however, investigators have used the Fermi-Eyges theory of electron transport (Rossi and Greissen, 1941; Eyges, 1948; Rossi, 1952; Jette et al., 1983) to construct pencil beam dose distributions. This theory provides analytical expressions which describe the electron fluence at any point in a "slab-type" medium for an incident pencil beam. The term "slab-type" indicates a medium in which any inhomogeneities are slabs extending infinitely in the directions perpendicular to the incident beam. The convenient analytical form of the solutions simplifies the computer implementation of the pencil beam method.

Although the simplicity of this approach is attractive, the Fermi-Egyes theory must be supplemented with empirical data in order to overcome the limiting assumptions of the theory (Hogstrom et al., 1981). In particular, the theory assumes (i) that individual scattering events result only in small angle deflections, (ii) that the electrons' cumulative angle of travel remains small and (iii) that the electrons' kinetic energy varies only as a function of depth in the scattering medium. Even with the addition of measured data, the assumptions (i) to (iii) lead to unacceptably large (see Section 1.1.1, page 2) dose calculation errors -- upto 40% -- in the vicinity of small inhomogeneities (Cygler et al., 1987; Mah et al., 1989).

Several investigators have modified the Fermi-Eyges theory to further improve the agreement with measured dose distributions. Some reports present modifications to the lateral pencil beam spread (Werner et al., 1982; Bruinvis et al., 1983; Van Gasteren, 1987; McParland et al., 1988; Bruinvis et al., 1989; Sandison et al., 1989) while others modify the Fermi-Eyges transport equation itself (Papiez and Sandison, 1990; Sandison

and Papiez, 1990; McLellan et al., 1991). Jette has, to some extent, relaxed the assumption (ii) above by including second-order angular scattering terms in the transport equation (Jette, 1985; Jette and Bielajew, 1989). Hemmer and Farquhar (1968) have gone still further by allowing angular scattering terms of arbitrarily large order. Although this approach allows large **cumulative** angles of travel, it does not account for **single** large-angle scattering events. However, Jette and Walker (1992) have done some preliminary work to include such events in the Fermi-Eyges theory.

Regardless of how the pencil beam dose distribution is obtained, any practical pencil beam algorithm should account for the presence of tissue inhomogeneities. Since an inhomogeneity alters the angular scattering and energy loss of the electrons, the shape of the pencil beam is altered both within and beyond the inhomogeneity. There exists no simple prescription to predict the distortion of a pencil beam in response to the presence of an inhomogeneity.

Figure 1-4 describes an approximate method of inhomogeneity correction known as the "slab approximation". The pencil beam is assumed to "see" an infinite slab of material lying perpendicular to the broad beam's central axis. The thickness of the slab is equal to the vertical distance traversed by the central ray of the pencil beam through the inhomogeneity. In the case of Fermi-Eyges-based pencil beam dose calculations, the Fermi-Eyges theory provides explicit equations describing the shape of a pencil beam in a slab-type medium. In the case of Monte-Carlo-generated pencil beams, there is no clear method to alter the shape of the pencil beam since the pencil beam dose distribution provides no information regarding the angular distribution of electrons. However, Lax and Brahme (1985) present an approximate method which makes assumptions about the angular distribution of electrons.

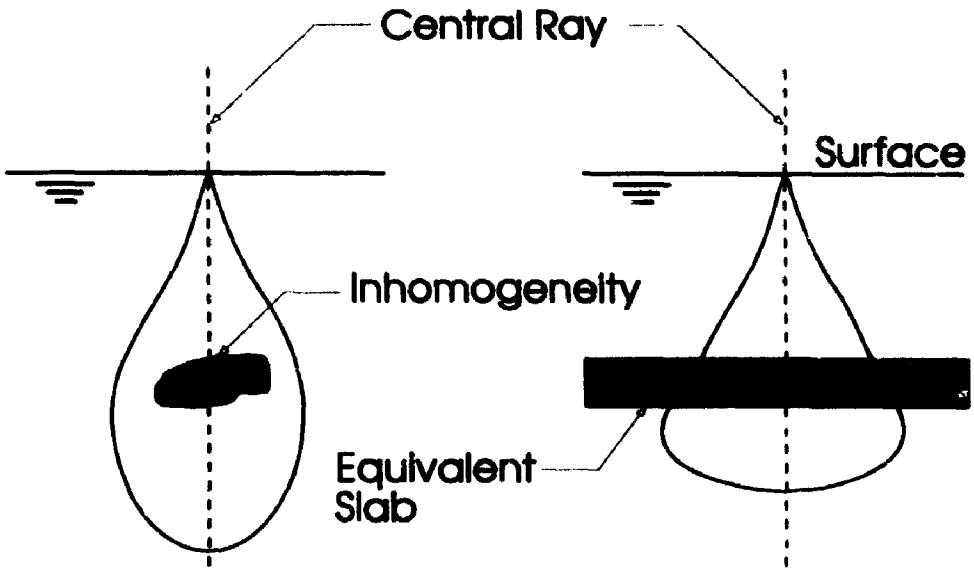

Figure 1-4: The Equivalent Slab Approximation

On the left, an inhomogeneity lies on the central ray of a pencil beam. To calculate the distortion of the pencil beam due to the presence of the inhomogeneity, an "equivalent" slab of material is used to approximate the inhomogeneity (shown on the right). In this example, the inhomogeneity is denser than the surrounding medium and produces more lateral scattering and energy loss. Thus, the lateral spread of the pencil beam is increased and the electrons' depth of penetration is reduced.

Provided the inhomogeneity is wider than the width of the pencil beam (about one half the range of the electrons) and the long axis of the inhomogeneity is perpendicular to the pencil beam's central ray, then the slab approximation is acceptable. However, for small inhomogeneities at large depths (where the pencil beam is broadest), the approximation leads to considerable error in the calculated dose distribution (Lax, 1986). Other researchers (Cygler et al., 1987; Mah et al., 1989) have shown that dose calculation errors can be large even when the inhomogeneity lies close to the surface of the scattering medium.

Yu et al. (1988) and Perry and Holt (1980) have presented a more general technique to modify pencil beams in the presence of small inhomogeneities. The method scales the pencil beam dose distribution along "mean electron paths" rather than simply along the pencil beam's central ray. However, the method depends on the Fermi-Eyges model of electron transport and it is still limited by the underlying assumptions of that

model (including the small angle assumption).

As noted earlier, the pencil beam approach is most accurate when the width of the pencil beams is small compared with the size of an inhomogeneity. Conventional pencil beam techniques divide a broad beam into narrow pencil beams at the surface of the scattering medium and the width of the pencil beams grows with depth. The pencil beam redefinition method (Storchi and Huizenga, 1985; Storchi and Van der Linden, 1989; Shui and Hogstrom, 1991) described in Figure 1-5 breaks the beam into a new set of pencil beams at regular depth intervals. In this way, the pencil beams are forced to remain narrow and the accuracy of dose calculations near small inhomogeneities is improved. However, the pencil beam redefinition method is still based on the Fermi-Eyges theory and is limited by the underlying assumptions of that theory. In addition, there exists no clear way to incorporate measured dose data to offset these fundamental limitations.

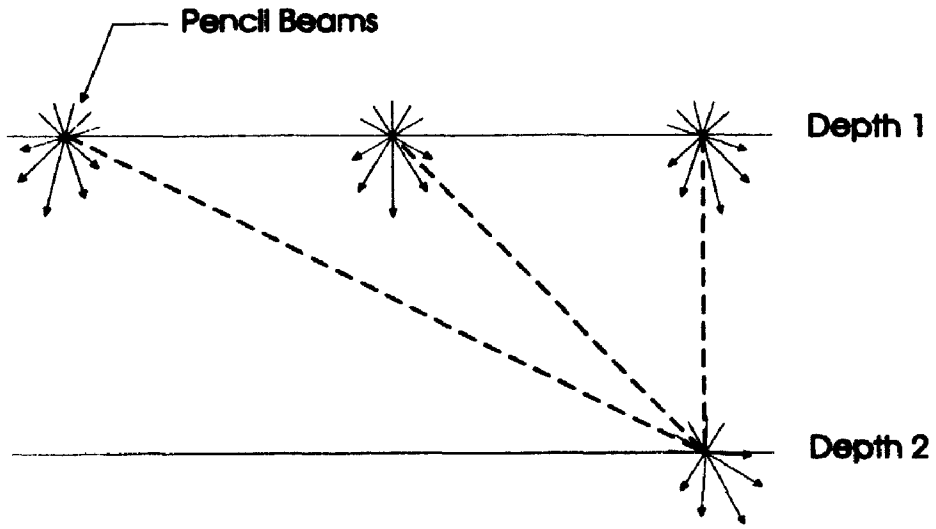

Figure 1-5: The Pencil Beam Redefinition Method

The pencil beams at depth 1 each contribute to a new pencil beam at depth 2. By tallying the number of electrons arriving at the new position from each angle, the first few moments of the angular distribution may be calculated and used to define the new pencil beam. Repetition of this procedure for each point at depth 2 allows the calculation of a new set of narrow pencil beams which may be used for transport calculations for the next increment of depth.

The various dose calculation techniques discussed above cannot accurately calculate the dose distribution in all situations of clinical interest. The ray line method

completely neglects the effect of angular scattering while the Fermi-Eyges-based methods make restricting approximations regarding the angular scattering and energy-loss processes. Although the pencil beam method provides accurate dose predictions in a **homogeneous** medium, **heterogeneous** media require the application of the slab approximation which is poor in the case of small inhomogeneities. Clearly, a more general approach is required.

1.3 The Transport Problem

The common failing of all the dose calculation methods described in section 1.2.3 is the failure to account for all the major aspects of electron transport in heterogeneous as well as homogeneous media. A more general computational technique -- one applicable to a greater variety of clinical situations -- requires the accurate modelling of all the physical processes which shape the dose distribution. The linear Boltzmann (or transport) equation achieves this required objective and, therefore, serves as a reasonable starting point in the discussion of more general dose calculation methods.

1.3.1 Time Dependent Transport Problem

The Boltzmann (or transport) equation is a linear integro-differential equation which describes the transport of particles through a scattering medium (Duderstadt and Martin, 1979). If $f(\boldsymbol{r}, \Omega, E; t)$ represents the density of penetrating electrons in a particular "state" (*ie* a particular position, $\boldsymbol{r}$, direction, Ω, and energy, E) at a particular time, t, then the time-dependent transport equation gives the time rate of change of $f(\boldsymbol{r}, \Omega, E; t)$:

$$\frac{df}{dt} = -\lambda(\boldsymbol{r},E)\,v(E)\,f(\boldsymbol{r},\boldsymbol{\Omega},E;t) - v(E)\,\nabla_{\boldsymbol{r}}\cdot\boldsymbol{\Omega}\,f(\boldsymbol{r},\boldsymbol{\Omega},E;t) + \int_{4\pi}\int_{E}^{E_{max}} v(E')\,f(\boldsymbol{r},\boldsymbol{\Omega}',E';t)\,\lambda(\boldsymbol{r},E')\,\omega_{\boldsymbol{r}}(\boldsymbol{\Omega},E;\boldsymbol{\Omega}',E')\,dE'd\boldsymbol{\Omega}' \quad (1.2)$$

where $\lambda(\boldsymbol{r},E)$ is the average number of angular-scattering and energy-loss events per unit path length; $v(E)$ is the speed of the penetrating electrons; $\omega_{\boldsymbol{r}}(\ldots)$ is the cross section, differential in both energy and angle, normalized such that its integral over all energies and directions is unity. The subscript, $\boldsymbol{r}$, indicates that the cross section depends on position since the scattering medium may contain inhomogeneities. The energy loss and angular scattering processes are discussed in Chapters 2 and 3 and specific cross sections are given in the appendices of the chapters.

The first term on the right hand side of Equation (1.2) represents the rate at which electrons leave the state, $(\boldsymbol{r},\boldsymbol{\Omega},E)$, due to energy-loss and angular scattering. The second term describes the "flow" (or divergence) of the electrons away from the point, $\boldsymbol{r}$. Finally, the last term represents the rate at which electrons scatter into the state, $(\boldsymbol{r},\boldsymbol{\Omega},E)$, from all other states. Therefore, Equation (1.2) implies that the sum of all three contributions must be the net rate at which electrons enter the state, $(\boldsymbol{r},\boldsymbol{\Omega},E)$.

Terms representing independent electron sources (*eg* beta-particles emitted from a radionuclide, Compton electrons from an external photon beam) and the production of secondary electrons (delta rays) may also be included in equation (1.2). For our purposes, we will concentrate on the transport of **primary** electrons only.

The problem of electron transport reduces to finding the solution of the transport equation (1.2) with appropriate initial and boundary conditions. For instance, the initial condition may be a "pulse" of electrons, $f(\boldsymbol{r},\boldsymbol{\Omega},E;0)$, from an electron linear accelerator incident on the surface of a patient at time, $t=0$. A reasonable boundary condition might be that the density of penetrating electrons, $f(\boldsymbol{r},\boldsymbol{\Omega},E;t)$, is zero on the surface of the patient for all times, $t>0$, and for all directions which would carry electrons into the patient (*ie* electrons can scatter out of the patient but cannot scatter back in).

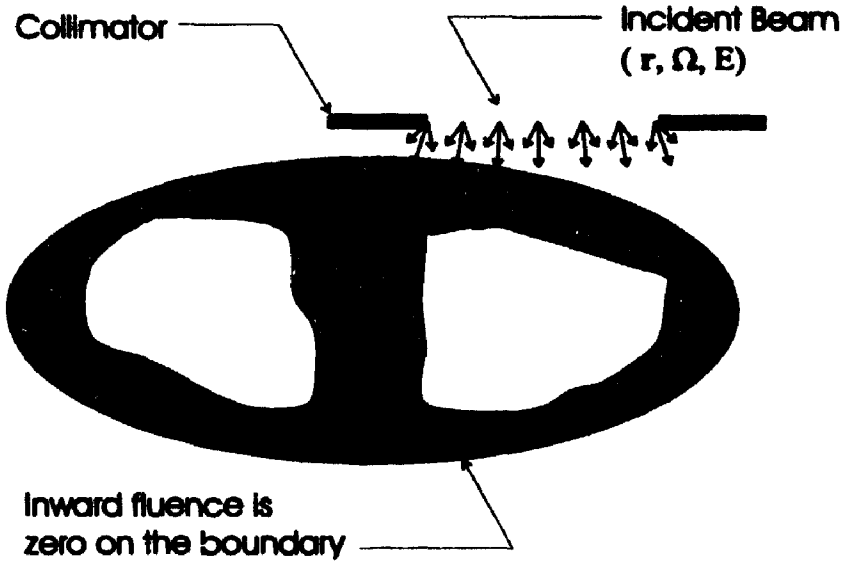

Figure 1-6: The Electron Transport Problem

The time dependent electron transport problem comprises three elements: (i) the initial condition, (ii) the boundary conditions, and (iii) the transport equation. In radiation therapy, the incident beam becomes the initial condition while the tissue-air interface approximates a vacuum boundary condition (*ie* electrons may leave the patient but cannot scatter back in).

The initial condition which describes a point monodirectional, monoenergetic beam of electrons is the Dirac delta-function[2],

$$f(\boldsymbol{r}, \Omega, E; t_0) = \delta(\boldsymbol{r}-\boldsymbol{r}_0)\ \delta_\Omega(\Omega\cdot\Omega_0)\ \delta(E-E_0) \qquad (1.3)$$

The solution of the transport equation (1.2) with this initial condition and some set of boundary conditions will be denoted $G_{t-t_0}(\boldsymbol{r}, \Omega, E; \boldsymbol{r}_0, \Omega_0, E_0)$ and is termed the "impulse response", "Green's function" or "kernel". Since Equation (1.2) is linear[3], the

---

[2]By definition, the angular Dirac delta function satisfies the relation,

$$\int_\omega \delta_\Omega(\Omega\cdot\Omega_0)\, g(\Omega)\, d\Omega = g(\Omega_0)$$

for any choice of neighbourhood, ω, of the point, Ω_0, and continuous function, $g(\Omega)$.

[3]If $g(\boldsymbol{r}, \Omega, E; t)$ and $h(\boldsymbol{r}, \Omega, E; t)$ both satisfy Equation (1.2), then so does $f(\boldsymbol{r}, \Omega, E; t) = A\cdot g(\boldsymbol{r}, \Omega, E; t) + B\cdot h(\boldsymbol{r}, \Omega, E; t)$ where A and B are constants.

solution for any arbitrary initial condition may be written as a superposition:

$$f(\boldsymbol{r}, \Omega, E; t) = \int_D f(\boldsymbol{r}_0, \Omega_0, E_0; t_0)\, G_{t-t_0}(\boldsymbol{r}, \Omega, E; \boldsymbol{r}_0, \Omega_0, E_0)\, d\boldsymbol{r}_0 d\Omega_0 dE_0 \qquad (1.4)$$

where the limit of integration, D, represents the domain of all possible positions, directions and energy. This last equation represents a linear superposition of impulse response functions weighted according to the initial condition, $f(\boldsymbol{r}_0, \Omega_0, E_0; t_0)$.

1.3.2 Time-Independent Transport Problem

The task of calculating a dose distribution in radiation therapy constitutes a time-independent problem; the quantity sought is the dose accumulated over the duration of the radiation exposure (the exposure time is about one minute and an electron takes about 10^{-9} seconds to come to rest in tissue). Therefore, the time-independent (or steady-state) transport equation is of particular significance in radiation therapy dose calculations. It derives from the time-dependent case simply by setting df/dt to zero in Equation (1.2). Since, the time-independent case requires no initial condition, we instead make the incident beam of electrons a source term (*ie* an inhomogeneous term) in the transport equation. Thus, we have,

$$\lambda(\boldsymbol{r}, E)\, f(\boldsymbol{r}, \Omega, E) + \nabla_r \cdot \Omega\, f(\boldsymbol{r}, \Omega, E) = Q(\boldsymbol{r}, \Omega, E) + \int_{4\pi} \int_{E}^{E_{max}} \gamma(E', E)\, f(\boldsymbol{r}, \Omega', E')\, \lambda(\boldsymbol{r}, E')\, \omega_r(\Omega, E; \Omega', E')\, dE' d\Omega' \qquad (1.5)$$

where γ is the ratio[4] $v(E')/v(E)$ and $Q(\boldsymbol{r}, \Omega, E)$ is the total number of electrons set in motion in a given state per unit volume per unit solid angle per unit energy. If $Q(\boldsymbol{r}, \Omega, E)$ is normalized such that its integral over all position, direction and energy

[4]The ratio, γ, does not appear if the transport equation is written in terms of the "flux", $\phi(\boldsymbol{r}, \Omega, E) = v f(\boldsymbol{r}, \Omega, E)$.

is unity, then $f(\boldsymbol{r}, \Omega, E)$ will represent a probability density.

In the time-independent case, the Green's function, $G(\boldsymbol{r}, \Omega, E; \boldsymbol{r}_0, \Omega_0, E_0)$, represents the response to a Dirac delta-function source (*ie* a monoenergetic, monodirectional pencil beam at a point in the scattering medium),

$$Q_\delta(\boldsymbol{r}, \Omega, E) = \delta(\boldsymbol{r}-\boldsymbol{r}_0)\ \delta_\Omega(\Omega\cdot\Omega_0)\ \delta(E-E_0) \qquad (1.6)$$

The solution for any arbitrary source, $Q(\boldsymbol{r}, \Omega, E)$, is then,

$$f(\boldsymbol{r}, \Omega, E) = \int_D Q(\boldsymbol{r}_0, \Omega_0, E_0)\, G(\boldsymbol{r}, \Omega, E; \boldsymbol{r}_0, \Omega_0, E_0)\, d\boldsymbol{r}_0 d\Omega_0 dE_0 \qquad (1.7)$$

This last equation is a generalization of the pencil beam summation (or superposition) technique for the calculation of dose described above.

1.4 Transport-Based Dose Calculation Methods

Even in relatively simple cases, exact analytical solutions to Equations (1.2) and (1.5) are not possible and approximate methods of solution are required. Any such method intended for clinical use must be both fast and accurate. There are two methods of dose calculation which include the relevant physical processes and which have the potential for use in clinical treatment planning: the Monte Carlo method and the evolution transport method. Since both these approaches solve the Boltzmann transport equation, they will be termed "transport-based dose calculation methods".

1.4.1 The Monte Carlo Method

This section is not meant as an exhaustive review of the Monte Carlo method (see instead Raeside, 1976; Mackie, 1990; Andreo, 1991) but will instead concentrate on the theoretical aspects of the method. Three different forms of the Monte Carlo method have been implemented: analog, condensed history and "macro". These three forms relate to the transport equations (1.2) and (1.5) in different ways.

Analog Monte Carlo

In its purest form, the Monte Carlo method (Berger, 1963; Andreo, 1991) simulates each discrete electron interaction. Given an electron with a particular position, direction, and energy, analog Monte Carlo (i) samples the distance to the next interaction from an exponential distribution, (ii) selects the type of interaction, and (iii) determines the new direction and energy by sampling the appropriate cross section. The interaction cross sections are sampled randomly by calculating pseudo-random deviates with appropriate probability distributions (Cormack and Shuter, 1991). Incident electrons are followed *one at a time* to the end of their trajectories (until either the electron energy drops below a pre-determined cut-off or the electron leaves the calculation volume). A single simulated trajectory is termed a "history".

Each electron history is consistent with the transport equation in the sense that each electron "obeys" the interaction cross section, $\omega_t(\ldots)$, and satisfies the boundary conditions. In addition, the start of each history is sampled according to the specified initial condition, $f(\boldsymbol{r}, \boldsymbol{\Omega}, E; t_0)$. As a result, a single history is one realization of a stochastic process whose probability density is the solution of the transport equation (1.2) with the specified initial condition. The superposition of many histories provides an estimate of this probability density.

Analog Monte Carlo always solves the time-dependent problem whether this information is explicitly used or not; a history begins at a certain point and evolves to a final destination. Often, path length rather than time plays the role of the variable of evolution, but there is a correspondence between time and path length. Thus, the use of path length is equivalent to a change of variables in the time-dependent transport equation (specifically, time, t, may be replaced by the path length, s, via the substitution, $s = \int_0^t v(t')\,dt'$).

Condensed History Monte Carlo

Although the analog Monte Carlo method has been applied to the calculation of energy-loss straggling in thin gas layers (Cobb et al., 1976; Ermilova et al., 1977) and

problems in radiation dosimetry (Bielajew et al., 1993), the method tends to be very time consuming and impractical for clinical dose calculations[5]. A technique known as the condensed history Monte Carlo method greatly reduces the calculation time by grouping (or condensing) many individual interactions into a single "transport step" (Berger, 1963). Partial (and usually approximate) solutions to the transport equation govern the change of an electron's position, direction and energy over a single transport step. The transport of an electron over a single step is determined by sampling the Green's function, $G_{step}(\boldsymbol{r}, \Omega, E; \boldsymbol{r}', \Omega', E')$, which represents the probability per unit volume, per unit solid angle, per unit energy that an electron starting in the state, $(\boldsymbol{r}', \Omega', E')$, will arrive in the state, $(\boldsymbol{r}, \Omega, E)$, in a single transport step.

For instance, the Monte Carlo code ETRAN (Berger, 1969) defines a transport step by specifying the path length travelled in the step. The change in angle is calculated according to the Goudsmit-Saunderson theory (Goudsmit and Saunderson, 1940; see Chapter 3) while the change in energy is calculated using Landau's theory (Landau, 1944; see Chapter 2). The code assumes that the electron travels in a straight line over a small increment of path length, Δs. Thus, the electron arrives at a position $\boldsymbol{r} = \boldsymbol{r}' + \Omega' \Delta s$ at the end of a transport step provided it started at the position, $\boldsymbol{r}'$, with the direction, Ω'. In this case, the Green's function is represented by,

$$\begin{aligned} & G_{step}(\boldsymbol{r}, \Omega, E; \boldsymbol{r}', \Omega', E') \\ & = f_{GS}(\Delta s, \Omega \cdot \Omega')\, f_L(\Delta s, E' - E)\, \delta(\boldsymbol{r} - \boldsymbol{r}' - \Omega' \Delta s) \end{aligned} \qquad (1.8)$$

where $f_{GS}(...)$ is the angular transition density predicted by the Goudsmit-Saunderson theory and $f_L(...)$ is the energy transition density predicted by Landau's theory.

Condensed history Monte Carlo comprises two categories dubbed class I and class II by Berger (1963). Class I Monte Carlo condenses **all** electron interactions into a single transport step. Class II Monte Carlo, on the other hand, explicitly simulates any

[5]A 10 MeV electron incident on water undergoes between 10^5 and 10^6 collisions before finally stopping.

"catastrophic" interactions which occur (*eg* production of an energetic delta ray). For instance, the Monte Carlo code, EGS4, (Nelson et al., 1985) groups all angular scattering as well as soft energy-losses (*ie* those below a predefined energy-loss cut-off) in a single transport step while catastrophic energy-losses are explicitly simulated. The Monte Carlo code developed by Andreo and Brahme (1984) considers catastrophic angular changes as well as catastrophic energy- losses.

Both class I and class II Monte Carlo schemes use **approximate** solutions to the time-dependent transport equation to model the angular and energy changes over a given transport step. As a result, the maximum length of a step is limited by the approximations applied in the solution of the transport equation. Since the calculation time required for a given simulation is inversely proportional to the average length of the transport steps, an upper limit for the allowable transport step length implies a lower limit for the calculation time. Thus, condensed history Monte Carlo is inherently limited in terms of its calculational efficiency.

The Macro Monte Carlo Method

The macro Monte Carlo method (Mackie and Battista, 1984; Ballinger, 1991; Neuenschwander and Born, 1992; Svatos, 1994; Neuenschwander et al., 1995) improves calculation times by eliminating many of the approximations inherent in the conventional condensed history schemes. The macro Monte Carlo method differs from conventional condensed history schemes in one respect: the Green's functions, $G_{step}(\mathbf{r}, \Omega, E; \mathbf{r}', \Omega', E')$, governing the changes in position, direction and energy over a transport step are pre-calculated using either analog Monte Carlo or conventional condensed history Monte Carlo simulations. As a result, the macro Monte Carlo method is not limited to a maximum step size and it can achieve much shorter calculation times than conventional condensed history schemes.

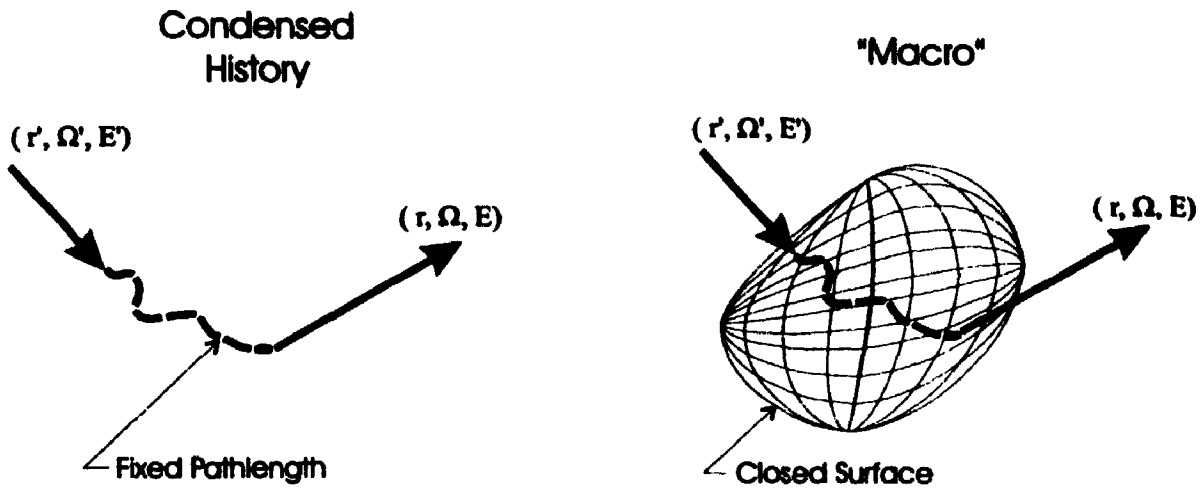

Figure 1-7: The Kugel Method of Transport Steps

The condensed history Monte Carlo schemes generally define a transport step using a fixed path length (though the length of the path may vary from step to step). In the "kugel" method, the transport step begins at the point where an electron enters a pre-defined closed volume and ends at the point where the electron first exits the volume. No information regarding the transit time or path length through the volume is retained.

The macro Monte Carlo methods presented thus far in the literature use a "kugel" method of defining the transport step. At the start of the transport step, an electron enters a closed volume (termed a "kugel" for "kernel generating element") and the transport step ends when the electron either first reaches a boundary of the closed volume or is absorbed. Neuenschwander and Born (1992) use a sphere in their approach; Ballinger (1991) uses a hemi-sphere; Mackie and Battista (1984) proposed a cube. Note that the path length traversed, or time spent, does not enter the definition of the transport step. Therefore, the macro Monte Carlo methods capitalize on the time-independent nature of the radiation therapy transport problem.

1.4.2 The Evolution Transport Method

The evolution transport method, rather than following one electron at a time,

propagates a *population* of electrons through the scattering medium (McLellan et al., 1992; Janssen et al., 1994; Papiez et al., 1994). For the purposes of numerical calculations, discrete bins of position, direction and energy serve to represent the distribution of electrons. This discrete distribution is updated (or "evolved") at each transport step according to the Green's function, $G_{step}(\boldsymbol{r}, \Omega, E; \boldsymbol{r}', \Omega', E')$. Thus, the probability density for the (i+1)th transport step is given by the recursion relation,

$$f_{i+1}(\boldsymbol{r}, \Omega, E) = \int_D f_i(\boldsymbol{r}', \Omega', E')\, G_{step}(\boldsymbol{r}, \Omega, E; \boldsymbol{r}', \Omega', E')\, d\boldsymbol{r}' d\Omega' dE' \qquad (1.9)$$

where D represents the domain of all possible positions, directions, and energies.

This expression may be approximated with the discrete summation:

$$f_{i+1}(\boldsymbol{r}, \Omega, E) = \sum_{l=1}^{N_r} \sum_{m=1}^{N_\Omega} \sum_{n=1}^{N_E} f_i(\boldsymbol{r}_l, \Omega_m, E_n)\, \Delta G_{lmn}(\boldsymbol{r}, \Omega, E) \qquad (1.10)$$

where the full six dimensional space has been divided into N_r spatial regions, N_Ω intervals of solid angle, and N_E energy intervals. The quantity, $\Delta G_{lmn}(\boldsymbol{r}, \Omega, E)$, represents the total probability of scattering from the lth volume element, $\Delta \boldsymbol{r}_l$, the mth element of solid angle, $\Delta\Omega_m$, and the nth energy interval, ΔE_n, into the state, $(\boldsymbol{r}, \Omega, E)$. It is given by,

$$\Delta G_{lmn}(\boldsymbol{r}, \Omega, E) = \int_{\Delta \boldsymbol{r}_l} \int_{\Delta\Omega_m} \int_{\Delta E_n} G_{step}(\boldsymbol{r}, \Omega, E; \boldsymbol{r}', \Omega', E')\, d\boldsymbol{r}' d\Omega' dE \qquad (1.11)$$

The quantity, $\Delta G_{lmn}(\boldsymbol{r}, \Omega, E)$, depends only on the initial state, final state and the manner in which the transport step is defined. Thus, $\Delta G_{lmn}(\boldsymbol{r}, \Omega, E)$ may be precalculated and stored for use in a variety of different calculations.

The expression (1.10) provides a prescription to calculate the distribution,

$f_{i+1}(\boldsymbol{r}, \Omega, E)$, provided the density, $f_i(\boldsymbol{r}, \Omega, E)$, is known. Recursive application of the equation allows a complete ensemble of electrons to be transported in discrete steps from a known initial state representing the incident electron beam to any desired step number. The recursive application of (1.10) may be represented symbolically as,

$$f_{N_{step}}(\boldsymbol{r}, \Omega, E) = \prod_{i=0}^{N_{step}-1} \boldsymbol{T}_i \cdot f_i(\boldsymbol{r}, \Omega, E) \qquad (1.12)$$

where N_{step} is the number of transport steps required and $\boldsymbol{T}_i$ represents the operator that "transports" the density, $f_i(\boldsymbol{r}, \Omega, E)$, a single transport step as defined by equation (1.10). Equation (1.10) together with the definition (1.11) provide all the elements necessary to calculate the transport of electrons in a scattering medium and thereby deduce the dose distribution.

1.5 Thesis Structure

The basic premise of the work presented here is that, to achieve accurate dose calculations in all situations of clinical interest, one must include all the physical processes which contribute significantly to the shaping of the dose distribution (*eg* angular scattering and energy-loss). The goal of this thesis is: (i) to elucidate the assumptions underlying the commonly-used models of energy-loss and angular scattering by formulating the various approaches with a single mathematical framework, and (ii) to explore, from a theoretical point-of-view, the relative merits of the Monte Carlo and evolution methods of transport calculations for use in radiation therapy dose calculations.

Chapter 2 (McLellan et al., 1994) summarizes various theoretical models of electron energy-loss in dense media and "unifies" these models in a single mathematical framework known as the compound Poisson process. It is demonstrated that the theory provides accurate predictions of electron energy-loss for the conditions relevant to clinical dose calculations. Chapter 3 provides an analogous discussion of the angular scattering process. Here also, it is demonstrated that the compound Poisson process provides a unifying mathematical framework for various models of electron multiple scattering.

Chapter 4 reveals the mathematical relationship between the Monte Carlo and evolution methods of electron transport calculations. By analyzing the convergence of these two methods, the chapter demonstrates that the Monte Carlo method has an advantage in "high-dimension" problems. As a result, a "dimensionally reduced" evolution method (McLellan et al., 1992; Papiez et al., 1994) is introduced which treats the transport of electrons in a medium as an evolution in depth (rather than time or path length).

Finally, Chapter 5 summarizes the work of the previous chapters. Possible extensions of the work are introduced and the elements necessary to realize a clinically usable dose calculation algorithm are discussed.

Chapter 2. Physics of Electron Energy-Loss[6]

2.1 A Method for the Calculation of Energy-Straggling Spectra

2.1.1 Introduction

As fast electrons penetrate a scattering medium, they suffer discrete energy-losses along their paths through two types of Coulomb interactions: collisions with atomic electrons (ionizational energy-losses) and collisions with atomic nuclei (radiative energy-losses). Due to the randomness in the number and size of these energy-losses, initially monoenergetic electrons form a spectrum of energies after travelling some finite path length, s. In the remainder of this paper, we will refer to this variation in energy-loss as "energy straggling" and we will refer to the resulting distribution of electron energies as the energy-loss spectrum.

Observed discrepancies (Rogers and Bielajew, 1986; Andreo, 1990) between the original ETRAN Monte Carlo code (Berger, 1969) and other Monte Carlo codes have highlighted the importance of energy straggling in electron beam dosimetry. Rogers and Bielajew (1986) showed that depth dose curves calculated using the *original* ETRAN code differ from curves calculated using other codes by 9% (surface dose) for a 20 MeV beam incident on water. They also noted differences in calculated practical ranges of up to 6% for 50 MeV electrons. Andreo (1990) also demonstrates these differences in calculated depth dose curves and notes slight differences in calculated stopping power ratios (up to 1% for 50 MeV incident electrons). However, the differences in stopping power ratios are quite small and Malamut et al. (1991) report differences of only 0.3% at 50 MeV (at depths greater than 10 cm). The discrepancies in calculated depth dose curves have been attributed (Rogers and Bielajew, 1986; Andreo, 1990) to the implementation of the Landau straggling theory (Landau, 1944) in the ETRAN Monte Carlo code. A correction

[6]This chapter has been published as: McLellan J, Sawchuk S, Battista JJ, Sandison GA and Papiez LS (1994) "A method for the calculation of electron energy-straggling spectra." Medical Physics **21**: 367-378

(Seltzer, 1988) of the original ETRAN code to account for weaknesses in the implementation of Landau's theory has resulted in excellent agreement with measurement and with other Monte Carlo codes (Seltzer, 1988; Andreo, 1990).

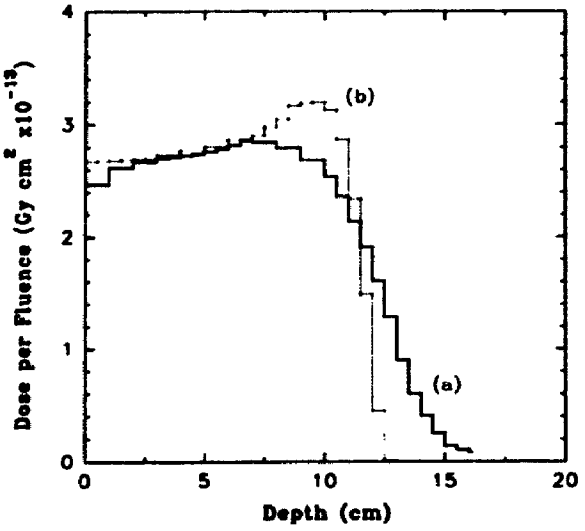

Figure 2-1: The Importance of Energy Straggling

Depth dose curves are shown for a broad, monoenergetic, monodirectional 30 MeV electron beam incident on a semi-infinite water phantom. The calculations were done using the EGS4/PRESTA Monte Carlo code (a) including all catastrophic events (AE=0.521 MeV and AP=0.01 MeV) and (b) using the continuous slowing down approximation.

Our particular interest lies in the application of energy straggling to numerical methods of electron beam dose calculation. To demonstrate the importance of energy straggling, we used the EGS4 Monte Carlo code (Nelson et al., 1985) to calculate the two depth dose curves shown in Figure 2-1. One calculation (a) included straggling by simulating all "catastrophic events" (*ie* energy-losses greater than 10 keV) while the other (b) neglected straggling by using the "continuous slowing down approximation" (csda) (see also Rogers and Bielajew, 1988). The average energy lost to both bremsstrahlung and ionization was included in the csda simulation. The depth dose curve calculated using the csda (b) differs markedly from the more realistic depth dose curve (a). This result indicates that methods of electron beam dose calculations intended for use in treatment planning must include energy straggling to achieve accurate dose predictions.

Numerical methods of dose computation calculate the "evolution" of the distribution of electrons (in position, direction, and energy) as they penetrate a scattering medium. Although they do not explicitly include energy straggling, the familiar pencil beam methods use measured (Hogstrom et al., 1981) or Monte Carlo (Lax et al., 1983) data to include implicitly the effects of energy straggling. Other numerical methods (Huizenga and Storchi, 1989; Morawska-Kaczynska and Huizenga, 1992; McLellan et al., 1992; Papiez et al., 1994) "propagate" the distribution of electrons in multiple increments of path length (or, equivalently, time). These methods rely on analytical models of energy straggling to calculate the evolution of the energy-loss spectrum over each increment. The accuracy of the numerical transport calculations depends on both the validity of the analytical models of energy straggling and the size of the path length increments.

This paper (1) discusses the assumptions inherent in currently available models of energy-loss straggling and (2) investigates the propagation of energy-loss spectra over multiple path length increments. We have found that existing methods for calculating energy-loss spectra for small path lengths (Sec. 2.1.2) derive from a single statistical model known as the *compound Poisson process* (Sec. 2.1.3). This "unified" description helps to clarify the assumptions and limitations inherent in the existing methods. Sec. 2.1.4 presents a convenient and direct method of calculation based on the compound Poisson process and fast Fourier transforms. Finally, Sec. 2.1.5 describes a method to propagate energy-loss spectra over multiple path length increments.

2.1.2 Review of Current Energy-loss Models:

Several authors have made theoretical investigations of the energy straggling of charged particles penetrating an absorbing medium (for short path lengths) and Bichsel (1988) has categorized these straggling calculations into five basic methods:

1) Moments Method:

This method uses a finite number of moments of the energy-loss spectrum to characterize the distribution of energy-losses. The first moment, or average energy-loss, corresponds to the continuous slowing down approximation (ICRU,

1984a). Inclusion of the second moment yields a Gaussian spread of energies and corresponds to "Gaussian straggling" (Fano, 1963). A general moments method which incorporates an arbitrarily large number of moments has also been described (Kessaris, 1966; Kessaris, 1970). The work of Kessaris describes not only the energy-loss spectrum but also the depth-penetration of electrons in a homogeneous phantom.

2) Laplace Transform Method:

Laplace transformation of the "kinetic" (or "Boltzmann") equation that describes the energy-loss process yields a first-order linear differential equation. Together with an appropriate initial condition, this equation may be solved analytically (Landau, 1944; Vavilov, 1957; Shulek et al., 1966) and the inverse Laplace transform of the solution may be obtained numerically (Borsch-Supan, 1961).

3) Convolution Method:

This method approximates the energy straggling distribution using a finite series. The n^{th} term in the series represents the n-fold convolution of the single-collision spectrum multiplied by the probability of an electron suffering n collisions (Bichsel and Saxon, 1975) (the "single-collision" spectrum is the differential energy-loss cross-section normalized to unity).

4) Monte Carlo Method:

In this method, individual energy-loss events are simulated by the use of pseudo-random numbers which are used to sample the single-collision spectrum. A random number of collisions is also generated and the individual energy-losses are summed to yield the total energy-loss. By repeating this process many times, an energy straggling distribution may be accumulated (Cobb et al., 1976; Ermilova et al., 1977). We note parenthetically that both this method (*ie* analog Monte Carlo) and the "condensed history" Monte Carlo method (eg ETRAN, EGS4) can yield accurate results although the latter does *not* simulate all individual interactions. Instead, to model the "soft" portion of the energy loss, the condensed history codes rely in part on analytical approaches to energy straggling as described in methods (1), (2) and (3) above. Only catastrophic collisions (*ie* those

above a preset threshold of energy transfer) are explicitly simulated.

5) Mixed methods:

The energy-loss spectrum is obtained from a convolution of multiple contributions to the energy spread. The distributions for the contributing processes are calculated using the methods listed above or using approximate methods. For example, Williams (1929) separates the energy-loss process into "soft" and "hard" collisions and approximates the soft collision energy-loss as a Gaussian straggling (this is also the approach that we adopt below). In other examples, a Gaussian function is convolved with Landau's distribution (Landau, 1944) to include the effect of the binding of the atomic electrons (Blunck and Leisegang, 1950; Hall, 1984). Matthews et al. (1981) include radiative interactions by convolving the distribution given by Blunck and Leisegang (Blunck and Leisegang, 1950) with a spectrum for radiative energy-losses.

We demonstrate in Appendix 2C that methods 1, 2 and 3 may be derived directly from an underlying **compound Poisson process**[7] (CPP, defined below) (Karlin and Taylor, 1981). Also, we show that the Monte Carlo method (method 4) is equivalent to a compound Poisson process under specific conditions. Thus, the CPP serves as a unifying theoretical framework relating these methods and, as discussed in the next section, it relies on three basic assumptions. As a result, all the methods summarized above must rely on these same three assumptions.

2.1.3 The Compound Poisson Process (CPP) Formulation

The basic equation describing the energy-loss, Δ, for a given path length, s, is:

$$\Delta(s) = \sum_{i=1}^{N(s)} e_i \qquad (2.1)$$

Both the number of events, $N(s)$, and the magnitude of the energy-losses, e_i, are

[7]Kellerer (1969) recognized the connection between the CPP and the Laplace transform methods but did not pursue the notion further.

random variables. We assume that:

(i) The individual energy-losses are all identically distributed according to a single-collision spectrum, $\omega^{E_0}(\epsilon)$, that does not change along the electron's path as the electron progressively loses energy ($\omega^{E_0}(\epsilon)\,d\epsilon$ represents the probability that, in one collision, the energy-loss will lie in the interval $[\epsilon, \epsilon+d\epsilon]$).

(ii) The energy-loss events are mutually independent (implying that the order in which events occur is not important).

(iii) The number of events in a given path length is Poisson-distributed.

Since the interaction cross section depends only on the energy of the penetrating electron and the properties of the target, the first assumption is satisfied provided that the energy loss of the electron is small. We might expect some discrepancies to arise in the tail of the energy-loss spectrum where large energy transfers have occured, but these will not affect the small energy-loss portion of the spectrum. Provided the first assumption holds then the second assumption follows from physical arguments; there is no causal connection between the energy loss in one event and the energy loss in any subsequent event. Finally, the third assumption follows from the observations that: (1) the probability of a collision in an *infinitesimally small* path length increment is vanishingly small and (2) the number of target atoms available for interaction in any *macroscopic* path length increment is very large. Thus, the distribution describing the number of collisions in a given path length increment may be interpreted as a limiting case of a binomial distribution; the number of "trials" (*ie* the number of infinitesimal path length increments) is large and the probability of "success" (*ie* the probability of a collision) in each trial is very small.

The assumptions stated above are precisely the three assumptions which define a CPP (Karlin and Taylor, 1981). The probability density describing the overall energy-loss given in equation (2.1) is well known from statistical theory (Karlin and Taylor, 1981):

$$f^{E_0}(s,\Delta) = \int_{-\infty}^{\infty} \exp[-\lambda s(1-\psi^{E_0}(p))] e^{i2\pi p\Delta} dp \qquad (2.2)$$

We note that (2.2) represents an inverse Fourier transform of the function $\exp[-\lambda s(1-\psi^{E_0}(p))]$. $f^{E_0}(s,\Delta)\,d\Delta$ is the probability that, for an electron travelling a fixed path length s, the energy-loss will lie in the interval $[\Delta, \Delta+d\Delta]$. λ is the *average* number of collisions per unit path length and $\psi^{E_0}(p)$ is the Fourier transform of the single-collision spectrum $\omega^{E_0}(\epsilon)$. The superscript E_0 indicates that the electron started with total energy E_0.

Electrons travelling long path lengths in a scattering medium violate assumptions (i), (ii) and (iii) since the energy lost along the path causes changes in the single-collision spectrum. Thus, energy-loss straggling calculations based on the compound Poisson process (*ie* the methods summarized in Sec 2.1.2) are valid only when the mean energy-loss is small compared with the incident electron energy.

2.1.4 Development of a Numerical Method for Short Path Lengths

In this section, we develop a method for the calculation of energy-loss spectra based directly on equation (2.2). The method is convenient for numerical calculations because it uses the familiar fast Fourier transform and it allows the input of various single-collision spectra. Also, the method includes both radiative and ionizational energy-losses.

Exploiting the independence of energy-loss events, we ignore the *order* in which the events occur and group energy-losses into three separate terms:

$$\Delta(s) = \Delta_{soft}(s) + \Delta_{hard}(s) + \Delta_{rad}(s) \qquad (2.3)$$

where

$$\Delta_{soft}(s) = \sum_{i=1}^{N_{soft}(s)} \epsilon_i^{soft} \qquad (2.4)$$

$$\Delta_{hard}(s) = \sum_{i=1}^{N_{hard}(s)} \epsilon_i^{hard} \qquad (2.5)$$

and

$$\Delta_{rad}(s) = \sum_{i=1}^{N_{rad}(s)} \epsilon_i^{rad} \qquad (2.6)$$

These three terms represent the soft ionizations (and excitations), hard ionizations and radiative energy-losses over a path length, s. The individual radiative energy-losses, ϵ_i^{rad}, are all assumed to be identically distributed according to a single-collision spectrum, $\omega_{rad}^{E_0}(\epsilon)$ (appendix 2B). Likewise, the individual soft and hard ionizational energy-losses, ϵ_i^{soft} and ϵ_i^{hard}, are assumed to be distributed according to the single-collision spectra, $\omega_{soft}^{E_0}(\epsilon)$ and $\omega_{hard}^{E_0}(\epsilon)$, respectively (appendix 2A). A cut-off energy, ϵ_{sep}, separates soft ionizations from hard ionizations. Specifically, soft ionizations lie in the range $[\epsilon_{min}, \epsilon_{sep}]$, while hard ionizations lie in the range $[\epsilon_{sep}, \epsilon_{max}]$ and we choose ϵ_{sep} to be larger than the mean atomic binding energy so that hard collisions may be treated as collisions between unbound electrons. The reason for the division between soft and hard ionizations will be made clear below. The quantities $N_{rad}(s)$, $N_{soft}(s)$, and $N_{hard}(s)$ represent the number of radiative, soft ionizational, and hard ionizational energy-losses, respectively, for a given path length, s. We assume that these are Poisson random variables.

With these assumptions, the three components of energy-loss given by equations (2.4), (2.5), and (2.6) are independent CPP's. The corresponding energy-loss spectra, $f_{soft}^{E_0}(s, \Delta)$, $f_{hard}^{E_0}(s, \Delta)$ and $f_{rad}^{E_0}(s, \Delta)$ are given by equations analogous to (2.2).

To apply Equation (2.2), it is necessary to calculate the average number of collisions per unit path length, λ, and the Fourier representation, $\psi^{E_0}(p)$, of the single-collision spectrum for each type of interaction (*ie* radiative, soft ionizational and hard ionizational). Specifically, the average number of radiative energy-losses per unit path length is given by

$$\lambda_{rad} = n_N \cdot \Sigma_{rad} \qquad (2.7)$$

where n_N is the number of nuclei per unit volume of scattering material and Σ_{rad} is the total radiative cross-section per nucleus (appendix 2B). Similarly, the average number of soft and hard ionizations per unit path length are given by

$$\lambda_{soft} = n_e \cdot \Sigma_{soft} \qquad (2.8)$$

and

$$\lambda_{hard} = n_e \cdot \Sigma_{hard} \qquad (2.9)$$

respectively. n_e is the number of target electrons per unit volume of scattering material and Σ_{soft} and Σ_{hard} are the total cross-sections per target electron for soft and hard ionizations, respectively (appendix 2A).

Because the radiative single-collision spectrum, $\omega_{rad}^{E_0}(\epsilon)$, is relatively "well behaved"[8], we can calculate its Fourier representation, $\psi_{rad}^{E_0}(p)$, directly using a fast Fourier transform (FFT). Ionizational energy-losses do not lend themselves to the same direct approach since the single-collision spectrum for ionizational energy-loss events increases rapidly as ϵ becomes small and the number of sampling points required to obtain an FFT over the full range of ϵ is impractically large. This is our reason for splitting ionizational energy-losses into soft and hard components. With a judicious

[8]The radiative single-collision spectrum increases with decreasing energy-loss but not as rapidly as the ionizational single-collision spectrum. Also, the radiative spectrum used in the present work incorporates a factor which brings the single-collision spectrum to zero for zero energy transfers (see Appendix 2B).

choice of ϵ_{sep}, a reasonable number of sampling points may be used to calculate $\psi^{E_0}_{hard}(p)$.

In the soft ionizational region (where the single-collision spectrum rises rapidly with decreasing energy transfer), we will use the "moments method" to approximate the energy-loss spectrum, $f^{E_0}_{soft}(s,\Delta)$, for soft ionizations using the first two moments of the spectrum. The first moment is simply the average energy-loss $\overline{\Delta}_{soft}(s)$ given by,

$$\overline{\Delta}_{soft}(s) = s\cdot\lambda_{soft}\cdot\int_{\epsilon_{min}}^{\epsilon_{sep}}\epsilon\cdot\omega^{E_0}_{soft}(\epsilon)\,d\epsilon \qquad (2.10)$$

The second moment is the variance of the energy-loss $\sigma^2_{soft}(s)$ given by,

$$\sigma^2_{soft}(s) = s\cdot\lambda_{soft}\cdot\int_{\epsilon_{min}}^{\epsilon_{sep}}\epsilon^2\cdot\omega^{E_0}_{soft}(\epsilon)\,d\epsilon \qquad (2.11)$$

Therefore, we approximate the energy-loss spectrum $f^{E_0}_{soft}(s,\Delta)$ with a Gaussian probability density:

$$f^{E_0}_{soft}(s,\Delta) \approx \frac{1}{\sqrt{2\pi\sigma^2_{soft}(s)}}\cdot\exp\left[-\frac{(\Delta-\overline{\Delta}_{soft}(s))^2}{2\sigma^2_{soft}(s)}\right] \qquad (2.12)$$

When ϵ_{sep} is small and the average number of soft collisions, $\lambda_{soft}\,s$, is large, equation (2.12) will be a good approximation since $\Delta_{soft}(s)$ is accumulated through many small independent energy-losses (Gikhman et al., 1979; Karlin and Taylor, 1981) (*ie* $\Delta_{soft}(s)$ approaches the "diffusional limit").

The three components of energy-loss are three **independent** CPP's. It follows that the total energy-loss spectrum, $f^{E_0}(s,\Delta)$, is given by,

$$f^{E_0}(s,\Delta) = f^{E_0}_{soft}(s,\Delta) * f^{E_0}_{hard}(s,\Delta) * f^{E_0}_{rad}(s,\Delta) \qquad (2.13)$$

where the symbol, $*$, indicates a convolution. Transforming (2.13) to the Fourier domain yields,

$$\phi^{E_0}(s,p) = \phi^{E_0}_{soft}(s,p) \cdot \phi^{E_0}_{hard}(s,p) \cdot \phi^{E_0}_{rad}(s,p) \qquad (2.14)$$

where

$$\phi^{E_0}_{soft}(s,p) = \exp\left[-2\pi\left(i\bar{\Delta}_{soft}(s)\, p + \pi\sigma^2_{soft}(s)\, p^2\right)\right] \qquad (2.15)$$

$$\phi^{E_0}_{hard}(s,p) = \exp\left[-\lambda_{hard}\, s\left(1 - \psi^{E_0}_{hard}(p)\right)\right] \qquad (2.16)$$

and

$$\phi^{E_0}_{rad}(s,p) = \exp\left[-\lambda_{rad}\, s\left(1 - \psi^{E_0}_{rad}(p)\right)\right] \qquad (2.17)$$

The functions $\phi^{E_0}_{soft}(s,p)$, $\phi^{E_0}_{hard}(s,p)$ and $\phi^{E_0}_{rad}(s,p)$ are the Fourier transforms of the spectra $f^{E_0}_{soft}(s,\Delta)$, $f^{E_0}_{hard}(s,\Delta)$ and $f^{E_0}_{rad}(s,\Delta)$, respectively. The method of calculation, therefore, consists of evaluating the functions (2.15), (2.16) and (2.17) and calculating the final energy-loss spectrum $f^{E_0}(s,\Delta)$ from an inverse FFT of (2.14).

2.1.5 Propagation of the Energy-Loss Spectrum

As we have mentioned, numerical methods for electron transport calculations propagate the distribution of electrons (in position, direction and energy) in small increments of path length. In this section, we isolate the propagation of the energy-loss spectrum so that it may be studied separately from the directional and positional re-distribution of electrons. The separation of energy loss and angular scattering is reasonable since the two processes arise from different types of interactions. Specifically, energy loss results from electron-electron collisions and bremsstrahlung interactions while

angular scattering results *primarily* from elastic nuclear scattering.

Consider an ensemble of electrons with an initial energy, E_0, which have all travelled a fixed path length s and which have acquired a spectrum of energy-losses $f^{E_0}(s,\Delta)$. We can use the Markov (Karlin and Taylor, 1981) property of the energy-loss process to calculate the energy-loss spectrum $f^{E_0}(s+t,\Delta)$ for an additional **small** increment of path length, t. In particular, we make the approximation,

$$f^{E_0}(s+t,\Delta) \approx \int_0^{\Delta} f^{E_0}(s,\Delta') \cdot f^{E'}(t,\Delta-\Delta')\, d\Delta' \qquad \textbf{(2.18)}$$

where

$$E' = E_0 - \Delta' \qquad \textbf{(2.19)}$$

The energy-loss spectra $f^{E'}(t,\Delta)$ may be calculated for all "initial" energies E' using the method described in the previous section.

The relation (2.18) is only an approximation because we neglect changes in the single-collision spectra, $\omega^{E'}(e)$, over the small path length interval, $[s,s+t]$. However, it can be shown that the error associated with this approximation is of order higher than t (*ie* the error is of order $o(t)$ and $\frac{o(t)}{t}$ vanishes as t is made infinitesimally small).

The relation (2.18) constitutes a transformation of the energy-loss spectrum, $f^{E_0}(s,\Delta)$, and we adopt the following shorthand notation:

$$f^{E_0}(s+t,\Delta) = \mathbf{T}_t \cdot f^{E_0}(s,\Delta) \qquad \textbf{(2.20)}$$

The transformation (2.20) provides a method to propagate the energy-loss spectrum over a small increment of path length, t. Now let us consider propagating an energy-loss spectrum over n small path length increments of size t_i $(i = 1,2,\ldots,n)$. If we are given a spectrum, $f^{E_0}(s_0,\Delta)$, at a path length, s_0, then at a path length,

$s_n = s_0 + t_1 + t_2 + \ldots + t_n$, we have,

$$f^{E_0}(s_n, \Delta) = \mathbf{T}_{t_n} \cdot \mathbf{T}_{t_{n-1}} \cdot \ldots \cdot \mathbf{T}_{t_1} \cdot f^{E_0}(s_0, \Delta) = \prod_{i=1}^{n} \mathbf{T}_{t_i} \cdot f^{E_0}(s_0, \Delta) \qquad \textbf{(2.21)}$$

Provided that all the increments t_i $(i = 1, 2, \ldots, n)$ are sufficiently small (*ie* $\frac{o(t_i)}{t_i} \to 0$, $i = 1, 2, \ldots, n$), the relation (2.21) gives an accurate representation of the energy-loss spectrum even for a long path length, s_n.

Table I: The table summarizes the method of calculation for small pathlengths, s.

Step	Explanation
1	Calculate the Fourier transform, $\psi^{E_0}_{hard}(p)$, of the single-collision spectrum for hard ionizational energy loss, $\omega^{E_0}_{hard}(\epsilon)$.
2	Calculate the Fourier transform, $\psi^{E_0}_{rad}(p)$, of the single-collision spectrum for radiative energy loss, $\omega^{E_0}_{rad}(\epsilon)$.
3	Evaluate the functions $\phi^{E_0}_{soft}(s, p)$, $\phi^{E_0}_{hard}(s, p)$ and $\phi^{E_0}_{rad}(s, p)$ as given by equations (2.15), (2.16) and (2.17) respectively.
4	Multiply the functions $\phi^{E_0}_{soft}(s, p)$, $\phi^{E_0}_{hard}(s, p)$ and $\phi^{E_0}_{rad}(s, p)$.
5	Take the inverse transform of the result of the multiplication in step 4 to yield the energy-loss spectrum, $f^{E_0}(s, \Delta)$.

2.1.6 Method and Results

Table I summarizes the method of calculation for small path lengths described in Sec. 2.1.4. To perform the fast Fourier transforms, we used the Cooley-Tukey algorithm (Brigham, 1974) with 2^{17} to 2^{19} sample points for both the forward and backward transforms. We checked each calculation to ensure that increasing the number of sample points did not significantly alter the calculated spectrum, thus confirming that any aliasing artefacts were negligible. Since the electron energy spectrum must be zero for energy-losses greater than the incident electron kinetic energy, T_0, the Nyquist criterion (Brigham, 1974) requires that the Fourier space representation of the spectrum be sampled at intervals of $\frac{1}{2T_0}$. Therefore, we sampled the single-collision spectra out to twice the incident kinetic energy (i.e. $2T_0$) to insure that the sampling in Fourier space was adequate for the backward transform. Appendices 2A and 2B describe the cross-sections which we used for ionizational and radiative interactions.

Preliminary calculations, done without radiative energy-losses, show the effect of varying the energy, e_{sep}, that separates hard and soft collisions. To determine a reasonable value for the parameter, e_{sep}, we calculated spectra for successively smaller values of e_{sep}. We found, as predicted by the theory of stochastic processes (Karlin and Taylor, 1981), that the calculated spectra converge to the correct spectrum as e_{sep} is reduced (Figure 2-2). For the absorber, the energy and the path length shown in Figure 2-2, an appropriate choice of e_{sep} is less than 0.05 MeV and for all calculations presented below, e_{sep} was set to 0.01 MeV.

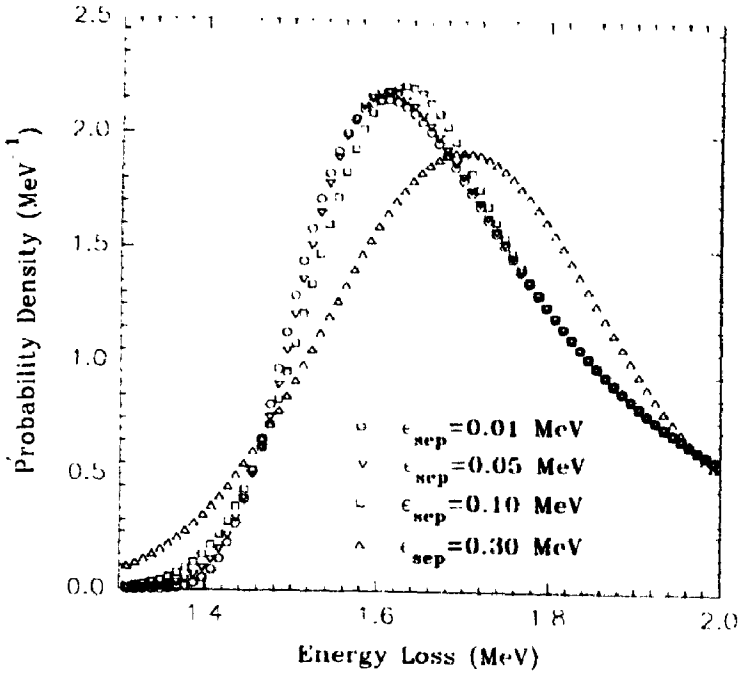

Figure 2-2: The Effect of the Cut-off Energy

The effect of changing the cutoff energy, ε_{sep}, is shown. Spectra were calculated for incident 10 MeV electrons after travelling a path length of 1.0 cm in water. The cutoff energies used were 0.01, 0.05, 0.1, and 0.3 MeV. Radiative energy losses have been *excluded* from the calculations (in this example only).

Figure 2-3 shows the calculated spectra for 10, 20 and 30 MeV electrons travelling 1 cm in graphite (ρ=1.7 g/cm^3) and 0.5 cm in aluminum (ρ=2.699 g/cm^3) absorbers. Spectra are shown both with and without radiative energy-losses and are compared with the results of condensed-history Monte Carlo simulations. The Monte Carlo results were generated using the EGS4 Monte Carlo code (Nelson et al., 1985) supplemented with the PRESTA routines (Bielajew and Rogers, 1986). The user code was written to sample the energy of a primary electron after it had travelled a given path length (Sawchuk et al., 1992). The transport cut-off energies for photons (AP) and electrons (AE) were 0.010 and 0.521 MeV (total energy), respectively. We found that lower values for AE and AP did not yield significantly different results (the insensitivity of the results to the choice of AE is explained in Sec. 2.1.7). Any photons and secondary electrons which were set in motion were immediately terminated. Primary electrons were followed until their total

energy fell below 0.521 MeV (i.e. ECUT=0.521 MeV).

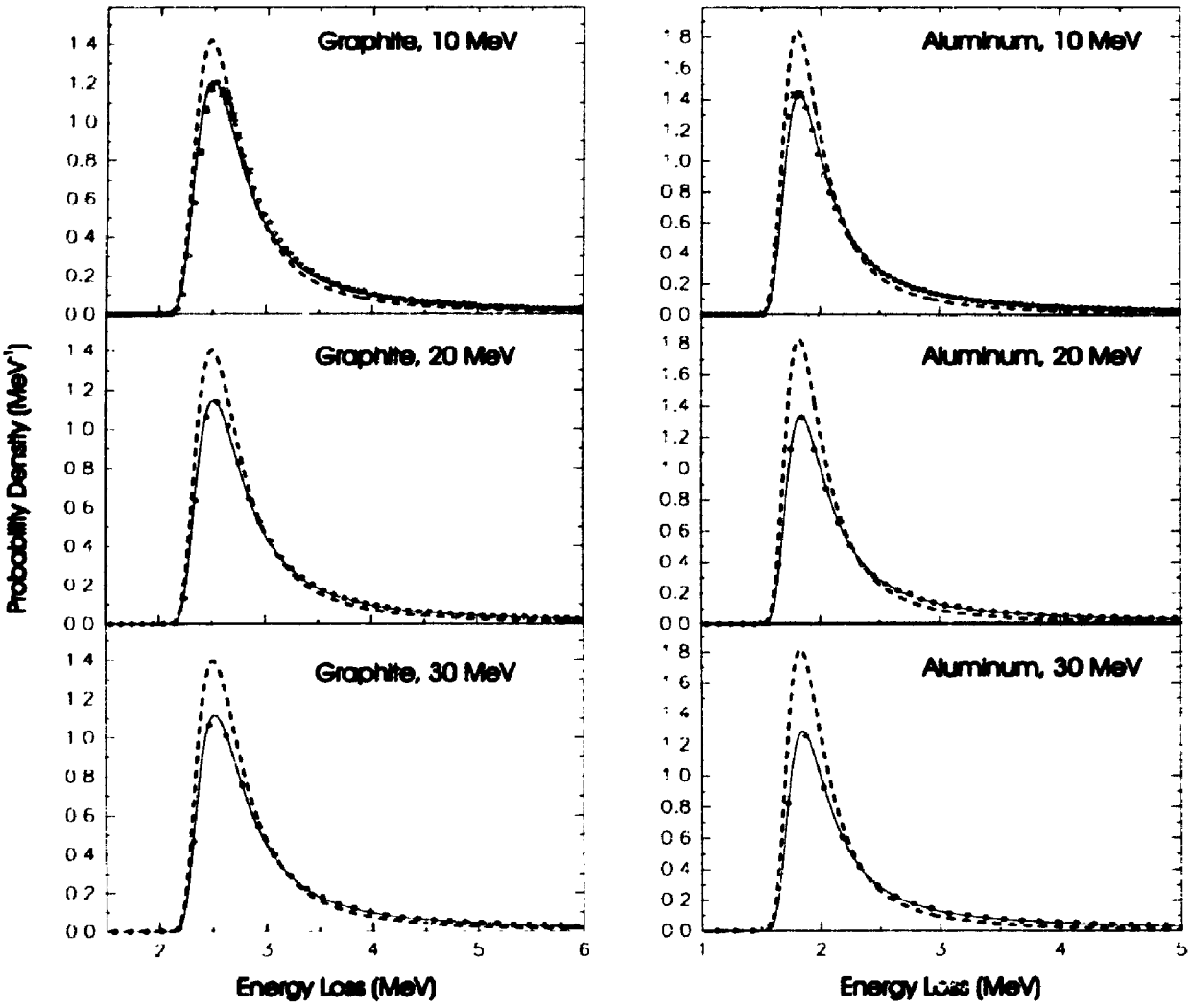

Figure 2-3: Calculated Energy Loss Spectra

Calculated spectra are compared with spectra obtained from EGS4 Monte Carlo simulations. Data for 10, 20 and 30 MeV electrons travelling 1 cm in graphite (density of 1.7 g/cm^3) and 0.5 cm in aluminum (density of 2.699 g/cm^3) are shown. Circles indicate the Monte Carlo simulations, the solid lines indicate the calculated spectra including both ionizational and radiative energy losses, and the dashed lines indicate the calculated spectra with radiative energy losses ignored (calculations were performed using a single path length increment). The error bars for the Monte Carlo data are shown only where the size of the error bar exceeds the size of the circle.

In order to propagate energy-loss spectra over multiple path length increments, the

transformation T_t defined by (2.20) and (2.18) was discretized in a straightforward way:

$$F(s+t,\Delta_m) \approx \sum_{i=1}^{m} F(s,\Delta_i)\cdot f^{E_i}(t,\Delta_{m-i})\cdot[\Delta_i-\Delta_{i-1}] \qquad (2.22)$$

where $E_i = E_0 - \Delta_i$ and $\Delta_i - \Delta_{i-1}$ is constant for all increments, i. The path length increment size, t, was held constant for all increments and the discretized spectra, $f^{E_i}(t,\Delta_m)$, were generated using the method of Table I for "incident" energies E_i ($i=1,2,\ldots,M$) where M is the number of discrete energy-loss "bins". For energies, E_i, where the electron range (assuming continuous slowing down) was less than the path length increment t, the function $f^{E_i}(t,\Delta)$ was set to zero for all Δ.

Figure 2-4 shows calculated spectra compared with results from Monte Carlo simulations for 30 MeV electrons travelling various path lengths in graphite. The Monte Carlo simulations were done in the same manner as described above. In Figure 2-4(a), the calculations were done using the method of Table I directly (i.e. without using the method of multiple path length increments). Figure 2-4(b) indicates the improved agreement with the Monte Carlo results when the method of multiple path length increments is used. Figure 2-5 shows calculations for various path length increment sizes and demonstrates the convergence of the calculated spectrum as the increment size is reduced.

2.1.7 Discussion

As outlined in Sec. 2.1.2, several methods exist for the calculation of electron energy-loss spectra and each of these methods has advantages and disadvantages. However, since each of these methods derives from a CPP, they are all subject to the three assumptions which define a CPP (Sec. 2.1.3). It follows that these methods are valid only for small path lengths where the average energy-loss is much less than the incident electron energy.

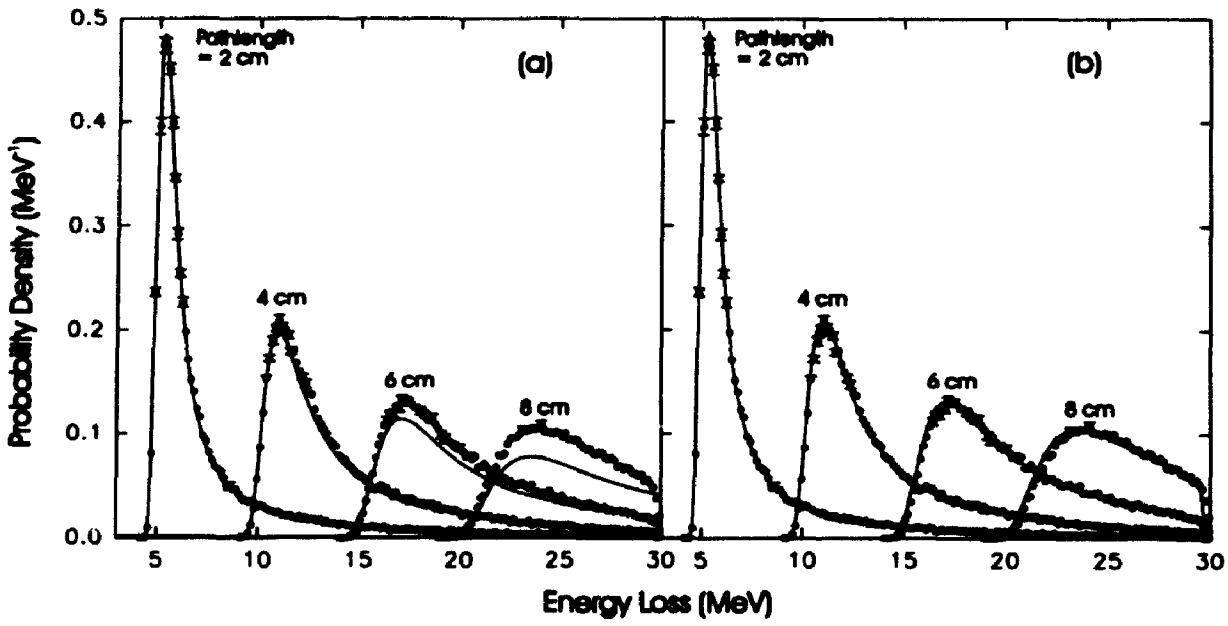

Figure 2-4: Calculated Energy-Loss Spectra for Long Path Lengths

Spectra are shown for incident 30 MeV electrons (R_{CSDA}=8.812 cm) travelling various path lengths in graphite (density of 1.7 g/cm^3). The circles indicate the results of an EGS4 Monte Carlo simulation, while the solid lines indicate the numerical calculations described in the current work. In (a) a single path length increment was used in the calculation of each spectrum. In (b) multiple path length increments of 0.25 cm each were used.

The method of moments is useful when the average energy-loss is the quantity of interest or when only a rough Gaussian approximation of the straggling is required. However, as can be seen from Figure 2-1, the csda approximation (first moment) is inadequate for the calculation of depth dose. Furthermore, an accurate calculation of an energy-loss spectrum using the method of moments necessitates a large number of terms.

The Monte Carlo and convolution methods, on the other hand, can provide accurate calculations of the energy-loss spectrum. However, in electron beam dosimetry, we are often interested in situations where a large number of electron interactions occur. The number of collisions suffered by a 10 MeV electron travelling 1 cm in water is of the order 10^5 collisions. To simulate each *individual* collision using the Monte Carlo

approach requires long calculation times. Also, the convolution approach would require approximately 10^5 terms in the expansion with a numerical convolution required for each term. Bichsel and Saxon (1975) report a method which greatly reduces the number of required convolutions but, for the path lengths of interest in this paper, their method would still require many numerical convolutions.

The Laplace transform method is more appropriate when the number of collisions is large. Landau's method (Landau, 1944), which is a Laplace transform method, is particularly convenient. Landau expressed the energy-loss spectrum in terms of a "universal function" ($\phi(\lambda)$ in his notation) which can be scaled for any given incident electron energy or any given scattering medium. Therefore, the universal function, which is given as a contour integral in the complex plane, needs to be calculated only once and tabulated (Borsch-Supan, 1961) or fitted using known functions (Tabata and Ito, 1979; Findlay and Dusautoy, 1980; Weinhous and Nath, 1984).

However, Landau's universal function can be obtained only when the maximum energy-loss for a single collision is extended to infinity (*ie* no upper limit of energy-loss is imposed). This approximation makes little difference in the region of the spectral peak, but it has serious implications for the tail of the distribution. In particular, as Δ becomes large, Landau's distribution asymptotically approaches ξ/Δ^2 where ξ is a constant. This implies that the energy-loss averaged over Landau's distribution is infinite and, therefore, non-physical:

$$\int_0^\infty \Delta \cdot f_L(s,\Delta)\, d\Delta \rightarrow \infty \qquad (2.23)$$

where $f_L(s,\Delta)$ is Landau's distribution for a given energy and scattering material. Any arbitrary average energy-loss can be generated simply by imposing various upper limits to the integration in (2.23). An *a priori* knowledge of the correct average energy-loss is required to set the appropriate upper limit of the integration (Seltzer, 1988). Furthermore, Landau's theory is not applicable to calculations of restricted energy-loss straggling (*ie* straggling due to soft collisions only).

To remove the ambiguity in the average energy-loss, it is necessary to impose an upper limit to the energy lost in a *single* collision. In this case, Landau's universal function is no longer valid and the inverse Laplace transform must be obtained numerically for every incident electron energy, path length, and scattering material of interest. These types of numerical calculations have been done successfully (Vavilov, 1957; Borsch-Supan, 1961; Shulek et al., 1966) and very fast methods of sampling the calculated energy-loss spectra have been developed (Rotondi and Montagna, 1990). However, we have chosen a different approach in this work for several reasons. The method of calculation given here does **not** depend on the interaction cross section used and allows various cross sections to be investigated. Also, the FFT used in the present work is a well known numerical technique and allows efficient numerical calculations.

The calculation time for the method described in this paper depends only on the number of Fourier sampling points used and is proportional to $N \cdot \log_2(N)$ where N is the number of sampling points. For calculations on a Sun SPARCstation II with 2^{18} sample points (as typically used in Figure 2-3), the CPU time was 220 seconds. However, we have been quite strict in our choice of the number of sampling points and the cut-off energy ϵ_{sep}. The results of Figure 2-3(a) (2^{18} sampling points, ϵ_{sep} = 0.01 MeV) change by no more than 0.5% in the spectral peak when only 2^{14} sample points and an ϵ_{sep} of 0.05 MeV are used. In this case, the cpu time is only 10.5 seconds. FFT algorithms which are faster than the one used here are available (Brigham, 1974). Also, we have not taken advantage of the fact that two real functions can be transformed simultaneously as fast as a single function (Press et al., 1988). These refinements could decrease the calculation time by a factor of two, but they remain for future work.

Figure 2-3 shows spectra calculated using our method compared with the results of Monte Carlo simulations. The comparisons are shown for two tissue substitutes: graphite, which is a soft tissue analog, and aluminum, which is a cortical bone analog. The range of energies investigated (10 to 30 MeV) is relevant for electron beam radiotherapy. The agreement between the calculated spectra and the Monte Carlo simulations is very good. In fact, the discrepancies are within the statistical uncertainties

of the Monte Carlo simulation (≈ 1% in the region of the spectral peak). In agreement with other investigations (Matthews et al., 1981), the results of Figure 2-3 indicate that the most probable energy-loss (the position of the spectral peak) does not shift appreciably when radiative energy-losses are neglected. Instead, the height of the spectral peak increases while the tail of the distribution decreases since fewer large energy transfers occur.

Table II: Stopping powers derived from the spectra of Figure 2-3 ("Calc") are compared with values tabulated by the ICRU ("ICRU 37"). The stopping powers are given in MeV cm^2/g.

Medium and Energy	$\left(\frac{S}{\rho}\right)_{ion}$		$\left(\frac{S}{\rho}\right)_{rad}$		$\left(\frac{S}{\rho}\right)_{tot}$	
	Calc	ICRU 37	Calc	ICRU 37	Calc	ICRU 37
Aluminum 10 MeV	1.6087	1.636	0.2903	0.2858	1.8990	1.921
Aluminum 20 MeV	1.6748	1.704	0.6420	0.6357	2.3168	2.340
Aluminum 30 MeV	1.7123	1.743	1.0123	1.003	2.7246	2.743
Graphite 10 MeV	1.7191	1.745	0.1547	0.1513	1.8738	1.896
Graphite 20 MeV	1.7872	1.816	0.3442	0.3417	2.1314	2.157
Graphite 30 MeV	1.8229	1.852	0.5444	0.5435	2.3673	2.396

By calculating the average energy-losses over the spectra shown in Figure 2-3 and dividing by the path length, we can calculate the associated electron stopping powers. In Table II, these stopping powers have been compared with values tabulated by the International Commission on Radiation Units and Measurements (ICRU) in the ICRU report 37 (ICRU, 1984b). This comparison serves as a check on the first moment of our calculated spectra. The calculated and tabulated values of total stopping power agree within 1.2%. We have separated the stopping powers in table II into ionizational and radiative components. It may be seen that most of the discrepancy in stopping powers is due to differences in the ionizational stopping power. Since the single-collision spectrum used in the present work for ionizational energy-losses is of a particularly

simple form (appendix 2A), the slight discrepancy in stopping powers is expected. The ICRU report 37 (ICRU, 1984) uses the Moller cross-section which accounts for relativistic and quantum mechanical effects (Evans, 1982). Since the focus of this paper is to demonstrate the calculational technique, a simplified single-collision spectrum seemed warranted. Indeed, the simple (Rutherford) cross section used in the present work is surprisingly close to the Moller cross section except for large energy transfers where the differential cross section is very small. A more complex cross-section can be used if greater accuracy is required.

As Figure 2-4(a) indicates, the spectra calculated using the method of Table I are accurate only for small path lengths (the single-step spectra are accurate only for a path length less than approximately 2 cm). The error for long path lengths results from energy-loss along the electrons' paths and from the concomitant changes in the single-collision spectra. The energy dependence of the single-collision spectra leads directly to the break-down of assumptions (i), (ii) and (iii) in Sec. 2.1.3. This difficulty is avoided by "propagating" energy-loss spectra in small increments of path length, adjusting the single-collision spectra at the start of each increment. Figure 2-4(b) shows the improved agreement with Monte Carlo simulations when calculations are made in small incremental s s of path length. The spectra calculated using path length increments of 0.25 cm agree well with the Monte Carlo predictions even for path lengths close to the end of the electron range.

Figure 2-5 shows the effect of varying the path length increment size for 30 MeV electrons travelling 8 cm in graphite. Clearly, as the increment size is reduced, the spectra converge to a stable result. The spectrum corresponding to 0.5 cm increments is only slightly different than that for 0.25 cm increments and choosing path length increments smaller than 0.25 cm does not significantly alter the calculated spectrum. Thus, an increment size of 0.25 cm (or roughly 0.5 g/cm^2) is sufficiently small to guarantee accurate calculations over the full electron range for 30 MeV electrons in graphite. Since energy-loss scales with density, 0.5 g/cm^2 is a suitable path length increment size for any low atomic number absorber.

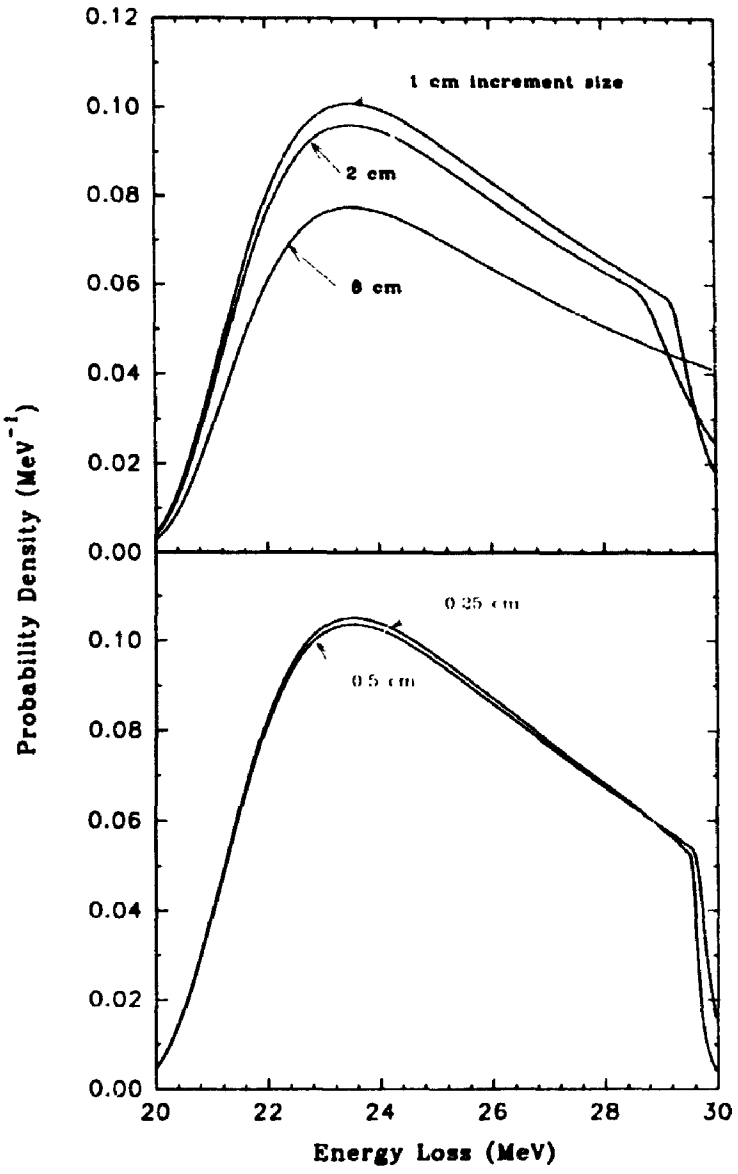

Figure 2-5: The Effect of Varying the Path Length Increment Size

Spectra are shown for incident 30 MeV electrons (R_{CSDA}=8.812 cm) travelling 8 cm in graphite (density of 1.7 g/cm^3). The spectra were calculated using the method of multiple path length increments for increment sizes of 0.25, 0.5, 1.0, 2.0 and 8.0 cm.

To separate ionizational energy-loss into soft and hard components, we used the fact that a CPP can be decomposed into two independent CPP's (Karlin and Taylor, 1981). We then approximated the soft component of energy straggling with a Gaussian diffusion process. The energy-loss ϵ_{sep} marks the separation between soft and hard

collisions and Figure 2-2 demonstrates a means of determining ϵ_{sep}. Provided ϵ_{sep} is sufficiently small, the calculated spectrum does not depend much on the choice of ϵ_{sep} (In Figure 2-2, the peak value of the energy-loss spectrum changes by only 1% and the position of the spectral peak does not shift measurably when ϵ_{sep} is reduced from 0.05 MeV to 0.01 MeV).

Let us consider in more detail the dependence of the calculated spectrum on ϵ_{sep}. Using the ionizational single-collision spectrum given in appendix 2A, the variances may be written

$$\sigma^2_{soft} = A \cdot (\epsilon_{sep} - \epsilon_{min}) \qquad (2.24)$$

and

$$\sigma^2_{hard} = A \cdot (\epsilon_{max} - \epsilon_{sep}) \approx A \cdot \epsilon_{max} \qquad (2.25)$$

where A is a constant dependent only on the path length, the incident electron energy and the type of scattering medium. In all practical cases, the condition, $\epsilon_{max} \gg \epsilon_{sep} > \epsilon_{min}$, will be satisfied and it follows that $\sigma^2_{hard} \gg \sigma^2_{soft}$. The total ionizational energy-loss spectrum is given by a convolution of the soft and hard energy-loss spectra. Since the energy-loss spectrum for soft ionizations, $f^{E_0}_{soft}(s, \Delta)$, is much narrower than that for hard ionizations, $f^{E_0}_{hard}(s, \Delta)$, the convolution results in a shift of $f^{E_0}_{hard}(s, \Delta)$ with little change in its shape. Indeed, $f^{E_0}_{soft}(s, \Delta)$ approaches a Dirac delta function as ϵ_{sep} and ϵ_{min} approach zero. Furthermore, the shift (which is equal to the mean soft ionizational energy-loss, $\overline{\Delta}_{soft}$) depends only *logarithmically* on ϵ_{sep}.

The separation of ionizational energy-losses into soft and hard collisions is a familiar concept in condensed history Monte Carlo codes (Andreo and Brahme, 1984; Nelson et al., 1985). In the EGS4 code (Nelson et al., 1985), the transport parameter, AE, is analogous to ϵ_{sep} and we noted in Sec. 2.1.6 that the EGS4 results were not strongly dependent on the choice of AE (provided AE is sufficiently small). We might expect this

since equation (2.24) predicts small values for σ^2_{soft} and implies that the fluctuations in soft ionizational energy-losses do not contribute appreciably to the overall energy straggling. Thus, EGS4 achieves accurate results despite using the continuous slowing down approximation for soft collisions.

2.1.8 Summary and Conclusions

Many numerical methods of electron transport calculations use analytical theories of energy straggling and several such theories appear in the literature. We demonstrate in the present work that all these theories derive from an underlying compound Poisson process (CPP) and, therefore, depend on the assumptions which define a CPP. Using the properties of a CPP and the fast Fourier transform (FFT), we have developed a calculational method which is convenient for use in situations where the number of collisions is large. Spectra calculated using this method agree with EGS4 Monte Carlo simulations within the statistical error of the simulations ($\approx 1\%$ in the region of the spectral peak). Also, stopping powers derived from the calculated spectra agree within 1.2% with values tabulated by the ICRU (1984). Using our method of calculation for small path lengths, we have investigated the propagation of energy spectra over multiple path length increments. For low atomic number absorbers, 0.5 g/cm^2 path length increments are necessary to guarantee accurate calculations of energy-loss spectra over the full electron range.

Appendix 2A: The Single-Collision Spectrum for Electron-Electron Collisions

The binding of the target electron to the atom complicates the form of the differential energy-loss cross-section for electron-electron collisions (*eg* see Hall, 1984). We divide electron-electron collisions into hard ($\epsilon > \epsilon_{sep}$) and soft ($\epsilon < \epsilon_{sep}$) collision regions and consider the hard collision region first.

If $\epsilon_{sep} \gg I$ where I is the mean ionization potential for the medium, then the target electrons behave as though they were unbound. This condition is satisfied in our calculations since ϵ_{sep} is 10 keV, whereas I is a fraction of 1 keV for most media (0.078 keV for graphite). Evans (1982) cites Bohr as the source of the following differential energy-loss cross-section for an incident electron colliding with a free stationary electron:

$$\frac{d\sigma_{ion}(\epsilon)}{d\epsilon} = 2\pi mc^2 r_e^2 \cdot \frac{(T+1)^2}{T(T+2)} \cdot \frac{1}{\epsilon^2} \qquad \text{(A.1)}$$

where T is the ratio of the incident electron's kinetic energy to its rest energy, mc^2, and r_e is the classical electron radius (2.818×10^{-15} m). To account for the indistinguishability of the incident and target electrons, the upper limit of energy-loss is set to half the kinetic energy of the incident electron (*ie* $\epsilon_{max} = mc^2 T/2$).

The single-collision spectrum, $\omega_{hard}^{E_0}(\epsilon)$, is related to the differential energy-loss cross-section, $d\sigma_{ion}/d\epsilon$, by

$$\omega_{hard}^{E_0}(\epsilon) = \begin{cases} \dfrac{1}{\Sigma_{hard}} \cdot \dfrac{d\sigma_{ion}(\epsilon)}{d\epsilon}, & \epsilon_{sep} < \epsilon \le \epsilon_{max} \\ 0, & \textit{otherwise} \end{cases} \qquad \text{(A.2)}$$

where the cross-section is calculated for the incident total energy, $E_0 = mc^2(T+1)$, and Σ_{hard} is the total cross-section for hard collisions obtained by integrating $d\sigma_{ion}/d\epsilon$ from ϵ_{sep}

to ϵ_{max}.

Consider now the soft collision region, $\epsilon < \epsilon_{sep}$. For the moment, we ignore the difficulties introduced by the binding of the target electrons and we apply the differential cross-section (A.1) to the soft collision region. Therefore, the single-collision spectrum, $\omega_{soft}^{E_0}(\epsilon)$, for soft collisions is given by,

$$\omega_{soft}^{E_0}(\epsilon) = \begin{cases} \dfrac{1}{\Sigma_{soft}} \cdot \dfrac{d\sigma_{ion}(\epsilon)}{d\epsilon}, & \epsilon_{min} \le \epsilon \le \epsilon_{sep} \\ 0, & otherwise \end{cases} \qquad (A.3)$$

where the cross-section is calculated for the incident total energy, $E_0 = mc^2(T+1)$, and Σ_{soft} is the total cross-section for soft collisions given by integrating $d\sigma_{ion}/d\epsilon$ from ϵ_{min} to ϵ_{sep}.

The neglect of binding and screening effects is, obviously, an approximation and the form of the single-collision spectrum is more complicated than equation (A.3) would indicate (see Hall, 1984). We can at least obtain the correct average soft ionizational energy-loss by choosing ϵ_{min} as,

$$\epsilon_{min} = \frac{I^2}{2mc^2T(T+2)} \cdot \exp\left[1 - \left(\frac{1}{T+1}\right)^2\right] \cdot \exp(\delta) \qquad (A.4)$$

where δ is the density effect correction as tabulated in ICRU report 37 (ICRU, 1984). Except for the inclusion of the density effect correction, this value of ϵ_{min} is the same as that used implicitly by Landau (1944). The use of a more exact cross section would negate the need to choose ϵ_{min}. However, for the path lengths and media investigated in this paper, the soft ionizations do not contribute appreciably to the over-all energy straggling and the use of a more complicated cross section is unwarranted.

We note at this point that (A.3) does not account correctly for the variance of soft energy-losses and the binding of the target electrons tends to broaden the energy-loss

spectrum (Blunck and Leisegang, 1950; Shulek et al., 1966; Hall, 1984). If $\omega^{E_0}_{true}(\epsilon)$ is the "true" single-collision spectrum which allows for the binding of the target electrons, the correct variance of soft energy-losses is given by,

$$\sigma^2_{true} = s \cdot \lambda_{true} \int_0^{\epsilon_{cap}} \epsilon^2 \omega^{E_0}_{true}(\epsilon) d\epsilon \qquad \text{(A.5)}$$

where λ_{true} is the true number of soft collisions per unit path length. It can readily be shown that σ^2_{true} can be written as the sum of two terms, σ^2_{soft} and $\sigma^2_{binding}$. σ^2_{soft} is the soft collision variance as given by (2.11) and $\sigma^2_{binding}$ is given by

$$\sigma^2_{binding} = \frac{s \cdot \lambda_{soft}}{\Sigma_{soft}} \int_0^{\epsilon_{cap}} \epsilon^2 \left(\Sigma_{true} \omega^{E_0}_{true}(\epsilon) - \Sigma_{soft} \omega^{E_0}_{soft}(\epsilon) \right) d\epsilon \qquad \text{(A.6)}$$

This last quantity represents the increase in energy-loss variance due to the binding of the target electrons. It has been calculated by direct numerical integration (Hall, 1984) and by approximate methods (Blunck and Leisegang, 1950; Shulek et al., 1966) and found to have an impact on the final energy-loss spectrum only when the path length is small or the atomic number of the absorber is high. Inclusion of $\sigma^2_{binding}$ represents only a very small correction for the path lengths and atomic numbers investigated in the present work and $\sigma^2_{binding}$ has been set to zero. It should be noted, however, that the effects of binding can be incorporated into our calculational method by replacing σ^2_{soft} with σ^2_{true} in equation (2.12).

Appendix 2B. The Single Collision Spectrum for Radiative Interactions

The differential radiative energy-loss cross-section which we use for the calculations in the present work is a modification of the cross-section given by Schiff (1951):

$$\frac{d\sigma_{rad}(\epsilon)}{d\epsilon} = F_p \cdot \frac{2Z^2\alpha r_e^2}{\epsilon}\left\{\left(\frac{E_0^2+E^2}{E_0^2} - \frac{2E}{3E_0}\right)\cdot\left(\ln(M) + 1 - \frac{2\arctan b}{b}\right)\right. \tag{A.7}$$
$$\left. + \frac{E}{E_0}\left[\frac{2\ln(1+b^2)}{b^2} + \frac{4(2-b^2)\arctan b}{3b^3} - \frac{8}{3b^2} + \frac{2}{9}\right]\right\}$$

where

$$b = \frac{2E_0E\cdot Z^{\frac{1}{3}}}{C\cdot mc^2\cdot\epsilon} \tag{A.8}$$

$$M = \left[\left(\frac{mc^2\cdot\epsilon}{2E_0E}\right)^2 + \left(\frac{Z^{\frac{1}{3}}}{C}\right)^2\right]^{-1} \tag{A.9}$$

C is a dimensionless constant with the value 111, the energy of the scattered electron is $E = E_0 - \epsilon$, Z is the atomic number of the target nucleus, and α is the fine structure constant. As suggested by Nelson et al. (1985), we have multiplied the cross-section by the factor F_p which was derived by Migdal (1956). This factor is given by,

$$F_p = \left[1 + \frac{n_e r_e \lambda_0^2 E_0^2}{\pi\epsilon^2}\right]^{-1} \tag{A.10}$$

where λ_0 is the Compton wavelength for an electron. The factor (A.10) prevents the cross-section from diverging at small energy transfers, ϵ.

The single-collision spectrum is related to the differential cross-section by

$$\omega_{rad}^{E_0}(\epsilon) = \begin{cases} \dfrac{1}{\Sigma_{rad}} \cdot \dfrac{d\sigma_{rad}(\epsilon)}{d\epsilon}, & 0 \le \epsilon \le \epsilon_{max} \\ 0, & otherwise \end{cases} \qquad \text{(A.11)}$$

In this case, the maximum allowable energy transfer, ϵ_{max}, is the kinetic energy of the incident electron. The total radiative cross section, Σ_{rad}, may be calculated by numerically integrating $d\sigma_{rad}/d\epsilon$ from 0 to ϵ_{max}.

Appendix 2C. Relationship of Other Methods to the CPP

In this appendix, we show that the methods of moments, Laplace transforms, and convolution can be derived directly from equations (2.1) and (2.2) which define a CPP. Also, we discuss the conditions under which the Monte Carlo method is equivalent to a CPP. We will deal with a "generic" single-collision spectrum, $\omega(\epsilon)$, since the discussion can be applied to both radiative and ionizational energy-losses. For convenience, we drop the superscript, E_0, and we assume that all mathematical operations and series expansions used are well-defined and convergent.

Moments Method:

Expanding the Fourier transform, $\psi(p)$, of the single-collision spectrum, $\omega(\epsilon)$, in a Taylor series about $p=0$ yields,

$$\psi(p) = \sum_{n=0}^{\infty} \frac{\psi^{(n)}(0)}{n!} p^n \qquad \text{(A.12)}$$

where $\psi^{(n)}(0)$ is the nth derivative of $\psi(p)$ evaluated at $p=0$. These derivatives are related to the moments of $\omega(\epsilon)$ by,

$$\psi^{(n)}(0) = (-i2\pi)^n \cdot m_n \qquad \text{(A.13)}$$

where m_n is the nth moment of $\omega(\epsilon)$. Substituting equations (A.13) and (A.12) in equation (2.2) gives

$$f(s,\Delta) = \int_{-\infty}^{\infty} \exp\left[\lambda s \sum_{n=1}^{\infty} \frac{(-i2\pi)^n}{n!} m_n \cdot p^n\right] e^{i2\pi p\Delta}\, dp \qquad \text{(A.14)}$$

It may readily be shown that neglecting terms of order p^2 and higher in the exponent gives a Dirac delta function centred on the average energy-loss, $\overline{\Delta} = \lambda s m_1$ (the first moment of $f(s,\Delta)$). This represents the continuous slowing down approximation (ICRU, 1984a). Alternatively, neglecting terms of order p^3 and higher gives a Gaussian

spectrum with mean $\overline{\Delta}$ and variance, $\sigma^2 = \lambda s m_2$ (the second central moment of $f(s,\Delta)$).

Laplace Transform Method:

Taking the Fourier transform of (2.2) yields,

$$\phi(s,p) = \exp[-\lambda s(1-\psi(p))] \tag{A.15}$$

Differentiating both sides with respect to s and taking the inverse Fourier transform yields,

$$\frac{df}{ds} = \lambda \int_{-\infty}^{\infty} \omega(e)[f(s,\Delta-e) - f(s,\Delta)]de \tag{A.16}$$

(we have used the normalization condition $\int \omega(e)\,de = 1$ and the convolution theorem). Equation (A.16) is the Boltzmann (or kinetic) equation describing the electron energy-loss and is the starting point for the Laplace transform methods (Landau, 1944; Vavilov, 1957; Shulek et al., 1966). In the literature, the factor λ is often "absorbed" into the single-collision spectrum, $\omega(e)$.

Convolution Method:

By factoring out $e^{-\lambda s}$ on the right hand side of equation (A.15) and expanding the remaining exponential in powers of $\lambda s \psi(p)$, it may be shown that,

$$\phi(s,p) = \sum_{n=0}^{\infty} \frac{(\lambda s)^n e^{-\lambda s}}{n!} (\psi(p))^n \tag{A.17}$$

Taking the inverse Fourier transform of (A.17) yields,

$$f(s,\Delta) = \sum_{n=0}^{\infty} \frac{(\lambda s)^n e^{-\lambda s}}{n!} \omega(\Delta)^{*n} \tag{A.18}$$

where

$$\omega(\epsilon)^{*n} \equiv \int_{-\infty}^{\infty} \omega(\epsilon-\epsilon') \cdot \omega(\epsilon')^{*(n-1)} d\epsilon' \qquad \text{(A.19)}$$

$$\omega(\epsilon)^{*0} \equiv \delta(\epsilon)$$

$$\omega(\epsilon)^{*1} \equiv \omega(\epsilon)$$

Equations (A.18) and (A.19) are the basis of the convolution method (Bichsel and Saxon, 1975; Bichsel, 1988). The factor $(\lambda s)^n e^{-\lambda s}/n!$ is equal to the probability of an electron suffering n collisions (assuming Poisson statistics). Therefore, the n^{th} term in the series (A.18) represents the n-fold convolution of $\omega(\epsilon)$ with itself multiplied by the probability of having n collisions.

Monte Carlo Method:

In the Monte Carlo method, individual energy-losses are simulated and summed to give the total energy-loss of an electron travelling a certain path length. This procedure is expressed mathematically in equation (2.1). Provided the energy-losses are "sampled" from the same single-collision spectrum for each energy-loss and the number of energy-losses is "sampled" from a Poisson distribution, the Monte Carlo procedure is (by definition) a CPP. Under these conditions, the energy-loss spectrum calculated using the Monte Carlo method will converge (for a large number of simulated electrons) to the same energy-loss spectrum calculated using any one of the above methods. Monte Carlo codes normally sample the length of the free path between successive collisions rather than sample the number of collisions directly. However, if the same exponential distribution is used to generate all free paths, then this procedure is equivalent to sampling the number of collisions from a Poisson distribution.

Chapter 3. Physics of Electron Angular Scattering

3.1 Introduction

As electrons penetrate a dense medium, they change their direction of travel frequently through collisions with atomic nuclei and, to a lesser extent, through collisions with orbital electrons. Because angular scattering is a random process, electrons which all start with the same direction of travel will acquire a spread of directions after travelling some fixed path length. Since the angular history of an electron determines its spatial trajectory[9], an accurate calculation of the spatial distribution of dose necessitates an accurate theory which describes the multiple scattering of electrons in solids.

Chapter 2 introduced the compound Poisson process (CPP) formulation of electron energy-loss. In close analogy with Chapter 2, this chapter introduces the CPP description of angular scattering (see also Ning, 1994) and investigates its accuracy for situations of relevance to the calculation of therapeutic electron beam dose distributions. Also, we highlight the close mathematical relationship between the energy loss process and the angular scattering process.

Given the scattering cross section for a single collision, multiple scattering theories aim to describe the angular distribution of electrons which suffer numerous interactions over a fixed path length. Goudsmit and Saunderson (1940) and Lewis (1950) present a general theory of electron multiple scattering. The theory makes only one assumption, namely that the energy-loss of the electrons is negligible over the path length considered. The theory does not restrict the form of the angular scattering cross section or the range of allowable angles. However, Goudsmit and Saunderson's expression for the multiple scattering distribution takes the form of a series of Legendre polynomials and, in its original formulation, the series converges very slowly for small path lengths. By

---

[9]The spatial and angular trajectories of an electron are related by,

$$\boldsymbol{r}(s) = \int_0^s \Omega(s')\, ds'$$

where s represents the path length travelled, $\boldsymbol{r}(s)$ is the position, and $\Omega(s)$ is the direction of travel.

separating out terms representing the un-scattered and once-scattered electrons, the convergence of the Goudsmit-Saunderson series improves for small path lengths (Berger and Wang, 1988).

Molière presents a less general multiple scattering theory (Molière, 1947; Molière, 1948; Bethe, 1953) which is valid only for small *cumulative* scattering angles and a sufficiently large number of collisions (greater than 20). The multiple scattering distribution at small angles depends only on a characteristic screening angle (χ_a in Molière's notation) and not on the particular form of the scattering cross section. At large angles, the distribution approaches the well-known Rutherford scattering cross section. Molière's theory does not apply to the case of very short path lengths (*ie* to single or plural scattering). However, Bielajew (1994) has recently reformulated Molière's theory to remove this restriction.

Bethe (1953) has confirmed that, for small angles and a sufficiently large number of collisions, the Goudsmit-Saunderson series reduces to the expression given by Molière. If we further assume that the number of collisions approaches infinity while the size of individual angular changes approaches zero, the angular scattering process becomes a diffusion process and the angular distribution approaches a Gaussian function. The Fermi-Eyges transport theory (Eyges, 1948; Rossi, 1952), which is central to many pencil-beam dose-calculation methods, relies intrinsically on this Gaussian scattering model.

Section 3.2 of this chapter summarizes the CPP formulation of electron multiple scattering and demonstrates the mathematical equivalence to the Goudsmit-Saunderson theory. Section 3.3 goes on to compare angular scattering distributions calculated using the CPP formulation with measured data and EGS4 Monte Carlo simulations. Emphasis is placed on situations of relevance to the calculation of electron beam dose distributions. Using the CPP formulation, Section 3.7 helps to clarify the concept of the "angular scattering power" and its application to the Gaussian scattering approximation.

3.2 The CPP Formulation of Multiple Scattering

3.2.1 Distribution for a Fixed Number of Scattering Events

In Figure 3-1, an electron travelling initially with direction Ω_0 scatters by an angle α_1 and azimuth ϕ_1 relative to Ω_0. After the scattering event, the electron has a new direction of travel, Ω_1. The change in direction is $\Delta\Omega_1 = \Omega_1 - \Omega_0$. If the electron were to scatter a second time with a change of direction $\Delta\Omega_2$, then the new direction would be given by $\Omega_2 = \Omega_1 + \Delta\Omega_2$. In general, the direction of travel after the n^{th} collision is given by the vectorial sum,

$$\Omega_n = \Omega_0 + \sum_{i=1}^{n} \Delta\Omega_i \qquad (3.1)$$

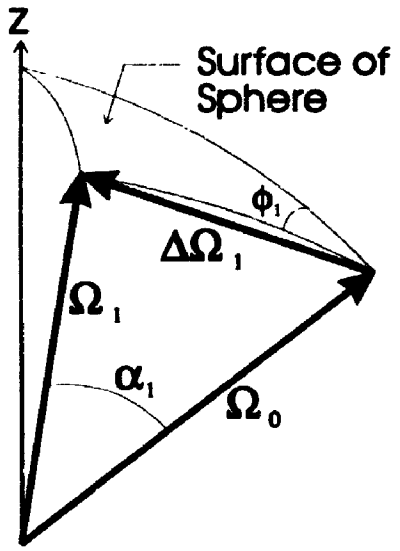

Figure 3-1: Spherical Geometry for Angular Scattering

An electron scatters from a direction, Ω_0, to another direction, Ω_1. Both directions may be represented by points on a sphere of unit radius. The scattering angle, α_1, is the angle between the two directions, Ω_0 and Ω_1. The scattering azimuth, ϕ_1, is the angle formed between two arcs on the surface of the sphere: one arc connecting the points Ω_0 and Ω_1 and the other arc connecting Ω_0 with the z-axis.

This last equation describes the angle of travel after *exactly* n collisions. Since the

outcome of any single scattering event is random, the direction, Ω_n, is a random variable.

The random variable, Ω_n, is described by an appropriate conditional probability density which specifies the probability per unit solid angle that an electron will acquire a direction, Ω_n, **given** that it started with a direction, Ω_0, and suffered exactly n collisions. Since the angular scattering cross section is symmetric about the initial direction of travel, these probability densities will be rotationally symmetric about the direction, Ω_0.

The probability density which describes the case of no collisions (*ie* $n=0$) is given by the "angular" Dirac delta function[10], $\delta_\Omega(\Omega\cdot\Omega_0)$, where the quantity, $\Omega\cdot\Omega_0$, represents the scalar (or "dot") product of the two vectors. In other words, electrons which have not scattered remain in the direction, Ω_0. The probability density describing the case of *one* collision (*ie* n=1), $\omega^{\Omega_0}(\Omega\cdot\Omega_0)$, is the differential angular scattering cross section normalized such that its integral over all directions is unity. The superscript, Ω_0, denotes the axis of symmetry (*ie* the initial direction).

The probability densities corresponding to more than one scattering event (*ie* n>1) will be denoted by $\omega^{\Omega_0}(\Omega\cdot\Omega_0)^{*n}$. The use of the superscript, "$*n$", is explained below. These probability densities may be generated using the recursion relation,

$$\omega^{\Omega_0}(\Omega\cdot\Omega_0)^{*n} = \int_{4\pi} \omega^{\Omega'}(\Omega\cdot\Omega')\,\omega^{\Omega_0}(\Omega'\cdot\Omega_0)^{*(n-1)}\,d\Omega' \qquad (3.2)$$

with

$$\omega^{\Omega_0}(\Omega\cdot\Omega_0)^{*0} = \delta_\Omega(\Omega\cdot\Omega_0) \qquad (3.3)$$

The relation (3.2) results from the following intuitive argument. The quantity,

---

[10]By definition, the angular Dirac delta function satisfies the relation,

$$\int_\omega \delta_\Omega(\Omega\cdot\Omega_0)\,g(\Omega)\,d\Omega = g(\Omega_0)$$

for any choice of neighbourhood, ω, of the point, Ω_0, and continuous function, $g(\Omega)$.

$\omega^{\Omega_0}(\Omega'\cdot\Omega_0)^{*(n-1)}$, represents the probability per unit solid angle that, in $n-1$ collisions, an electron will scatter from a direction, Ω_0, into an intermediate direction, Ω'. The quantity, $\omega^{\Omega'}(\Omega\cdot\Omega')$, represents the probability per unit solid angle that an electron will scatter from the intermediate direction, Ω', to the final direction, Ω, in one additional scattering event. Multiplying the two together gives the probability per unit solid angle that an electron will scatter from Ω_0 to Ω via the intermediate direction, Ω'. Finally, summing (*ie* integrating) over all possible intermediate directions yields the desired probability density, $\omega^{\Omega_0}(\Omega\cdot\Omega_0)^{*n}$.

The relation (3.2) has a form analogous to a convolution. Thus, $\omega^{\Omega_0}(\Omega\cdot\Omega_0)^{*n}$ is the n-fold "spherical convolution" of $\omega^{\Omega_0}(\Omega\cdot\Omega_0)$ with itself (hence the use of the superscript, "$*n$"). This approach assumes implicitly that all the scattering events, $\Delta\Omega_i$, $i=1,\ldots,n$ are identically distributed (*ie* the scattering cross section is the same in each collision).

3.2.2 Distribution for a Fixed Path Length

The relation (3.2) gives the angular distribution of electrons which have scattered **exactly** n times. However, in any fixed path length, s, the number of angular scattering events is a random variable. Assuming that the number of scattering events is Poisson distributed, then the fraction of electrons which scatter exactly n times is $(\lambda s)^n e^{-\lambda s}/n!$ where λ represents the average number of scattering events per unit path length. If the scattering events are independent, then we may sum the probability densities, $\omega^{\Omega_0}(\Omega\cdot\Omega_0)^{*n}$, with the appropriate weights for all possible values of n to obtain the probability density, $f^{\Omega_0}(s,\Omega\cdot\Omega_0)$, describing the angular distribution of electrons for a fixed path length, s. *ie*

$$f^{\Omega_0}(s, \Omega \cdot \Omega_0) = \sum_{n=0}^{\infty} \frac{(\lambda s)^n e^{-\lambda s}}{n!} \cdot \omega^{\Omega_0}(\Omega \cdot \Omega_0)^{*n} \qquad (3.4)$$

This last expression gives the probability per unit solid angle that an electron will change its direction of travel from Ω_0 to Ω in the course of travelling a path length, s.

The following summarize the assumptions made in the derivation of Equation (3.4):

(i) the scattering events are independent,

(ii) all scattering events are identically distributed, and

(iii) the number of events in a given path length is a Poisson random variable.

These are precisely the assumptions which define a compound Poisson process (see Chapter 2). In fact, equation (3.4) is completely analogous to the convolution method for the calculation of the energy-loss distribution described in Chapter 2 (see Appendix 2C, Equation A.18).

The CPP expression (3.4) for the angular scattering distribution provides a convenient means to calculate the angular distribution for short path lengths since only the first few terms of the series make a significant contribution. However, in the case of long path lengths, the number of terms required is excessive; the number of terms required is of the order of λs (*ie* the average number of angular scattering events). Ning (1994) has shown that accurate and practical calculations may be performed by splitting the angular scattering process into small and large angle regimes in a manner analogous to the division between "soft" and "hard" energy-loss events presented in Chapter 2. Small angle scattering is treated as a diffusion process (which is Gaussian for small **cumulative** angles of travel) and the CPP series is used to calculate the contribution from the few large-angle collisions.

Instead, this chapter uses the expression,

$$f^{\Omega_0}(s, \Omega\cdot\Omega_0) = \sum_{i=0}^{\infty} \frac{2i+1}{4\pi} \exp[-\lambda s(1-a_i^{(1)})] P_i(\Omega\cdot\Omega_0) \qquad (3.5)$$

where

$$a_i^{(1)} = \int_{4\pi} \omega^{\Omega_0}(\Omega\cdot\Omega_0)\, P_i(\Omega\cdot\Omega_0)\, d\Omega \qquad (3.6)$$

is the ith Legendre polynomial, $P_i(\Omega\cdot\Omega_0)$, averaged over the normalized cross section, $\omega^{\Omega_0}(\Omega\cdot\Omega_0)$ (*ie* $a_i^{(1)} = \langle P_i(\Omega\cdot\Omega_0)\rangle_1$). Appendix 3C demonstrates that Equation (3.5) is completely equivalent to the expression (3.4). However, (3.5) has the advantage of faster convergence for large path lengths.

In the special case where the electrons travel initially along the z-axis (*ie* $\Omega_0 = \boldsymbol{k}$ where $\boldsymbol{k}$ is a unit vector lying along the z-axis), Equation (3.5) reduces to the familiar expression given by Goudsmit and Saunderson (1940):

$$f_{GS}(s,\theta) = f^{\boldsymbol{k}}(s, \Omega\cdot\boldsymbol{k}) = \sum_{i=0}^{\infty} \frac{2i+1}{4\pi} e^{-\lambda s(1-\langle P_i(\cos\theta)\rangle_1)} P_i(\cos\theta) \qquad (3.7)$$

where θ denotes the scattering angle with respect to the z-axis and $P_i(\cos\theta)$ are the Legendre polynomials.

3.2.3 Analogy with Electron Energy-Loss

Table 3.1: The mathematical formulation of electron energy loss straggling is compared with that of angular scattering. Both processes are described using a CPP formalism.

Quantity	Energy-Loss Straggling	Angular Scattering
Random Variable	E	Ω
Relative Variable	$\Delta = E_0 - E$	$\Omega \cdot \Omega_0$
Probability density for fixed number of interactions	$\omega^{E_0}(\Delta)^{*n}$	$\omega^{\Omega_0}(\Omega \cdot \Omega_0)^{*n}$
Probability density for fixed path length	$f^{E_0}(s, \Delta)$	$f^{\Omega_0}(s, \Omega \cdot \Omega_0)$
CPP formulation (convolution form)	$\sum_{n=0}^{\infty} \frac{(\lambda s)^n e^{-\lambda s}}{n!} \omega^{E_0}(\Delta)^{*n}$	$\sum_{n=0}^{\infty} \frac{(\lambda s)^n e^{-\lambda s}}{n!} \omega^{\Omega_0}(\Omega \cdot \Omega_0)^{*n}$
CPP formulation (alternate form)	$\int_{-\infty}^{\infty} e^{-\lambda s(1-\phi^{E_0}(p))} e^{i2\pi p\Delta} dp$	$\sum_{i=0}^{\infty} \frac{2i+1}{4\pi} e^{-\lambda s(1-a_i^{(1)})} P_i(\Omega \cdot \Omega_0)$

The CPP formulation of multiple angular scattering is completely analogous to the description of electron energy-loss given in the previous chapter. Table 3.1 lists the corresponding variables and expressions in each of the two formalisms. In the last row of Table 3.1, the energy-loss distribution is written as a superpostion of the basis functions, $e^{i2\pi p\Delta}$, (*ie* as a Fourier transform) while the angular distribution is written as a superpostion of the basis functions, $\frac{2i+1}{4\pi} P_i(\Omega \cdot \Omega_0)$. In the case of electron energy-loss, the superposition takes the form of a continuous integral since only the boundary condition at E=0 needs to be specified. In the case of angular scattering, the superposition takes the form of a discrete sum since directions are defined only on the surface of the sphere and the distribution of directions must satisfy periodic boundary conditions.

From a mathematical standpoint, only two differences exist between angular scattering and electron energy-loss: (i) the direction of travel is described by a two-dimensional vector while the energy loss is described by a one dimensional scalar, and (ii) the direction of travel is defined only for a finite space which corresponds to the surface of the unit sphere while electron energy is defined for the infinite interval $[0,\infty)$.

3.3 Method of Calculation

This section provides details of the CPP formulation of the multiple angular scattering process for situations relevant to the calculation of therapeutic electron beam dose distributions. Angular distributions are presented for monoenergetic, monodirectional electrons which have passed through a uniform slab of scattering material. To validate the calculated angular distributions, comparisons are made both with measured angular distributions (Hanson et al., 1951) and with EGS4 Monte Carlo simulations.

3.3.1 Evaluation of the Series (3.5):

The angular scattering distribution is given by the series (3.5). In the calculations presented below, the initial direction of travel will coincide with the z-axis so that the expansion coefficients, $a_l^{(1)}$, are given by Equation (C.2). The coefficients were calculated numerically using a trapezoidal numerical integration technique (Press et al., 1988) and the Legendre polynomials were generated using the procedure described by Press et al. (1988). The discrete bins used in the numerical integration were concentrated at small angles where the single-collision cross section changes rapidly. The calculations used the Mott angular scattering cross section with a screening correction to account for the effects of orbital electrons (Appendix 3B).

Even for the shortest path length considered here, the series converged at small angles (less than one radian) with at most 1000 terms. However, the convergence of the series is slow at very large angles. Fortunately, the number of electrons scattered into large angles is negligible (at least for our purposes) when the path length is small. In the

case of 15.7 MeV electrons passing through a 0.001 cm thick gold foil, 1000 terms in the series provides complete convergence at all angles up to 1 radian. The number of electrons at this angle is already 6 orders of magnitude less than the number of forward-directed electrons.

3.3.2 Absorbers Containing More than One Atomic Species:

In cases where the scattering medium contains more than one atomic species, the angular scattering process is assumed to be a superposition of independent processes which represent the scattering contributions from each of the atomic species (Karlin and Taylor, 1981). For n_A different atomic species, the series (3.5) becomes (assuming the initial direction of travel is along the z-axis),

$$f^k(s,\cos\theta) = \sum_{i=0}^{\infty} \frac{2i+1}{4\pi} e^{\left(-s\sum_{m=1}^{n_A}\lambda_m(1-a_{i,m}^{(1)})\right)} P_i(\cos\theta) \qquad (3.8)$$

where λ_m is the average number of collisions with the m^{th} atomic species per unit path length and $a_{i,m}^{(1)}$ is the i^{th} expansion coefficient for the m^{th} atomic species given by,

$$a_{i,m}^{(1)} = 2\pi\int_0^{\pi}\omega_m^k(\cos\theta)\,P_i(\cos\theta)\sin\theta d\theta \qquad (3.9)$$

$\omega_m^k(\cos\theta)$ is the normalized single collision cross section for the m^{th} atomic species.

3.3.3 Energy-Loss Correction

The CPP formulation of electron multiple scattering assumes that all angular scattering events are identically distributed. However, electrons passing through a relatively thick slab may lose a significant portion of their initial energy. Since the angular scattering cross section is energy dependent, the single-collision probability density, $\omega^{\Omega_0}(\Omega\cdot\Omega_0)$, will change slightly along the electron's path. In the calculations presented below, the average energy-loss was estimated to be $S_{tot}(E_0)\Delta z$ where

$S_{tot}(E_0)$ is the total stopping power calculated at the *incident* electron energy, E_0, and Δz is the thickness of the slab of scattering material. The scattering cross section was then calculated for the average electron energy in the slab which is given approximately by $E_0 - S_{tot}(E_0)\,\Delta z/2$. This approximation is valid since the stopping power remains nearly constant along the electron's path except near the end-of-range.

3.3.4 Path Length Correction

On average, the true path length traversed by the electrons is greater than the thickness of the scattering slab. If the average angle cosine for electrons penetrating the scattering slab is $\langle\cos\theta\rangle_{\Delta z}$, then the thickness of the slab, Δz, and the electrons' average path length are related approximately by,

$$\Delta z \approx s\langle\cos\theta\rangle_{\Delta z} \qquad (3.10)$$

To calculate the path length, s, for a given slab thickness, Δz, we require an expression for the average angle cosine, $\langle\cos\theta\rangle_{\Delta z}$. Note that $\cos\theta$ is just the first Legendre polynomial, $P_1(\cos\theta)$. Note also that the averages of the Legendre polynomials, $\langle P_i(\cos\theta)\rangle_s$, for a given path length, s, are given by,

$$\langle P_i(\cos\theta)\rangle_s = 2\pi\int_0^{\pi} P_i(\cos\theta)\, f^k(s,\cos\theta)\sin\theta d\theta \qquad (3.11)$$

(assuming that the electrons travel initially along the z-axis). Inserting the series (3.5) in this last expression and using the orthogonality of the Legendre polynomials, we find,

$$\langle P_i(\cos\theta)\rangle_s = \exp(-\lambda s(1-a_i^{(1)})) \qquad (3.12)$$

If we approximate the average angle cosine, $\langle\cos\theta\rangle_{\Delta z}$, by the average of $P_1(\cos\theta)$ at a point mid-way through the scattering slab (*ie* at $\Delta z/2$), then the electrons' average path length through the scattering slab is,

$$s \approx \exp\left(\lambda \frac{\Delta z}{2}\left(1-a_1^{(1)}\right)\right) \Delta z \qquad (3.13)$$

This "path length correction" was applied to the calculated angular distributions given below.

3.3.5 Characteristic Screening Angle

The angular scattering cross section incorporates a "characteristic screening angle" to account for the screening effects of the orbital electrons. The calculated multiple angular scattering distribution can vary significantly depending on the choice of this screening angle. Rossi (1952), Jackson (1962), and ICRU (1984a) give a screening angle which under-estimates the screening effect and therefore gives angular distributions which are too broad compared with experiment. The present work uses the more accurate screening angle given by Molière (see Bethe, 1953). Nigam et al. (1959) give an even more accurate expression for the screening angle, but Molière's expression was found to be sufficient for all the cases investigated here.

3.3.6 EGS4 Monte Carlo Simulations

To assess the accuracy of the calculational technique described above, we wrote a user code (called "FOIL") for the Electron Gamma Shower (EGS4) Monte Carlo system. The user code simulates the scattering of electrons in a uniform slab of material. The angular distributions of primary and secondary electrons (or delta rays) were scored separately and, in all cases, the secondary electrons gave a negligible contribution to the angular scattering distribution at small angles (even for a delta ray production threshold as low as AE=0.512 MeV which corresponds to a kinetic energy of 0.001 MeV). Therefore, the Monte Carlo data presented below includes only primary electrons.

For the simulation of low energy electron transport, EGS4 allows the user to fix (in subroutine FIXTMX) the maximum fraction of an electron's kinetic energy which may be lost in one transport step (ESTEPE). Preliminary calculations were done with various values of ESTEPE. For high atomic number materials (*eg* gold), an ESTEPE of 0.3%

was required while, for low atomic numbers (*eg* water), an ESTEPE of 1.0% was adequate.

The other EGS4 parameter of interest (AE) determines the division between "soft" collisions (energy transfer less than AE) and catastrophic collisions (energy transfer greater than AE). EGS4 "double counts" the angular scattering due to electron-electron collisions (Werner et al., 1994) and, for small values of AE, EGS4 over-estimates the angular scattering of electrons. This effect is especially important in low atomic number materials. The calculations presented below used an AE of 0.911 MeV (total energy) and showed no strong dependence on AE when the value was reduced to 0.711 MeV.

3.4 Results

3.4.1 Comparison with Measured Data

Since Monte Carlo simulations will serve as a comparison for the calculated angular distributions, some validation of the Monte Carlo calculations was necessary. To this end, this section compares published measurements (Hanson et al., 1951) both with data from the Monte Carlo simulations and with our calculated angular distributions.

Figure 3-2 shows the comparison of the measured, calculated, and Monte-Carlo-generated data for a gold foil approximately 0.001 cm thick. Figure 3-3 makes the same comparison but for a foil of twice the thickness.

The agreement between the measured data, calculated distributions and Monte Carlo simulations is excellent in the case of the thin gold foil. In the case of the thick gold foil, both the CPP calculation and the EGS4 simulation under-estimate the forward-scattered intensity by about 2%. However, the agreement at larger angles is excellent.

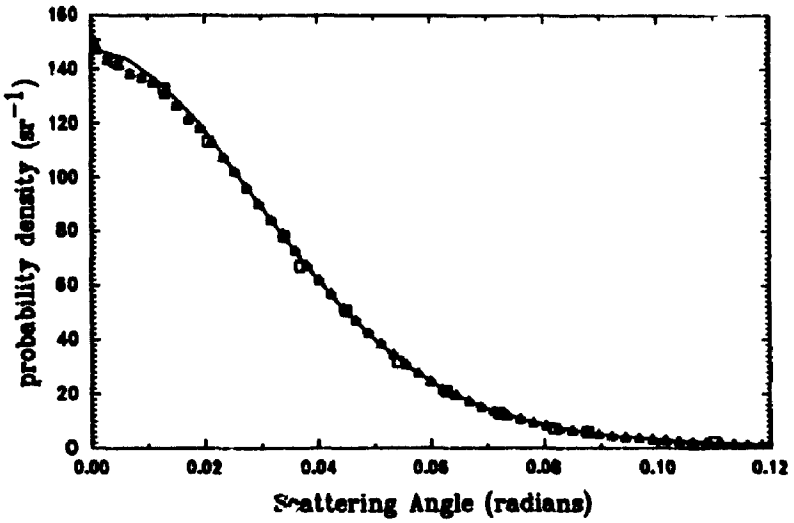

Figure 3-2: Angular Scattering in a Thin Gold Foil

The figure shows the angular distribution of 15.7 MeV electrons passing through a gold foil of thickness 18.66 mg/cm^2. The CPP calculation (solid line) used 1000 terms in the series (3.5). The squares represent the data measured by Hanson et al. (1951) and the triangles (with error bars) represent the EGS4 Monte Carlo data (ESTEPE is 0.3%, AE is 0.911 MeV).

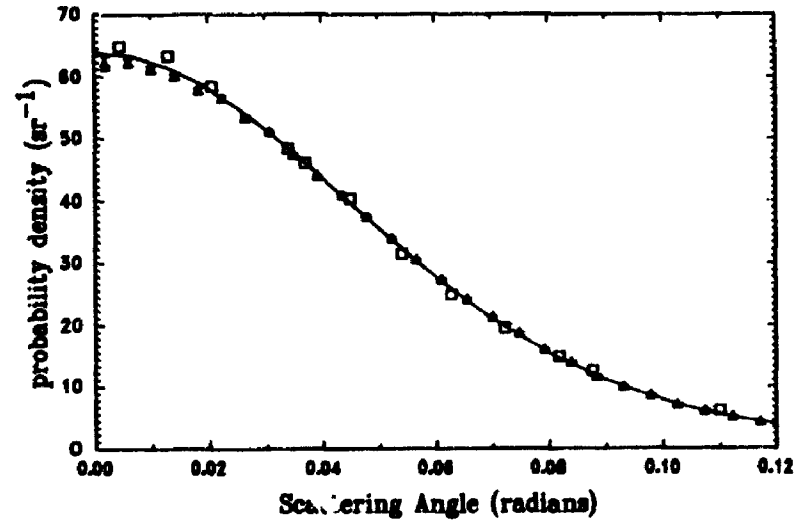

Figure 3-3: Angular Scattering in a Thicker Gold Foil

The figure makes the same comparison as in Figure 3-2 except that the thickness of the foil is 37.28 mg/cm^2.

3.4.2 Calculations in Tissue-Equivalent Media

Although the comparisons made above serve to validate the EGS4 Monte Carlo simulations, the case of a thin high atomic number foil is of little relevance to the situations encountered in the calculation of electron dose distributions in tissue. We are more interested in relatively thick slabs (*eg* 1 cm) of low-atomic-number materials. Therefore, this section compares the CPP calculations with EGS4 Monte Carlo simulations of the angular scattering of electrons in slabs of water of various thicknesses.

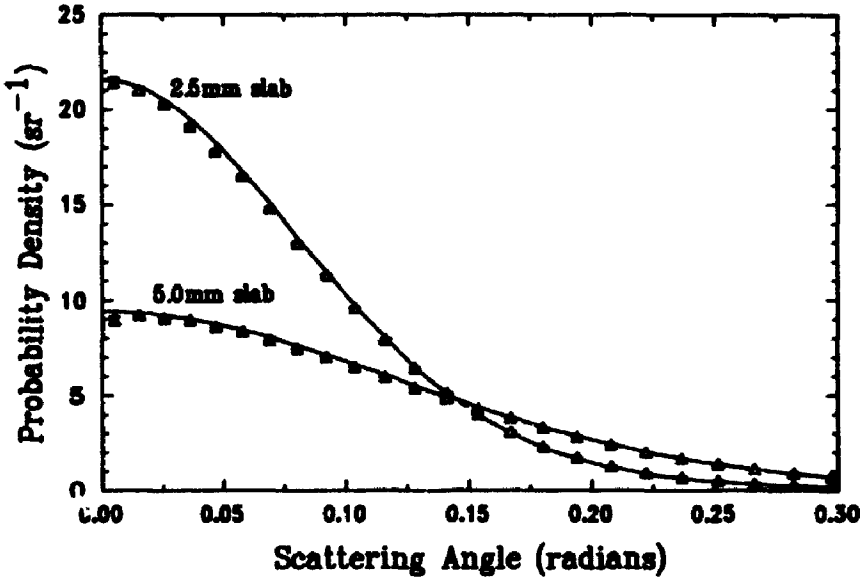

Figure 3-4: Angular Scattering of 10 MeV Electrons in Water Slabs

The figure shows the angular distribution of 10 MeV electrons passing through a 2.5 mm water slab and a 5.0 mm water slab. The solid lines represent the summation of 500 terms in the series (3.5). The triangles represent EGS4 simulations using the user-code, "FOiL" (ESTEPE is 1.0%, AE is 0.911 MeV).

Figure 3-4 demonstrates that the agreement between the CPP calculations and the EGS4 Monte Carlo simulation is very good for 10 MeV electrons passing through water slabs of 2.5 mm and 5.0 mm thickness. The agreement is similarly good for the case of 5 MeV electrons (Figure 3-5).

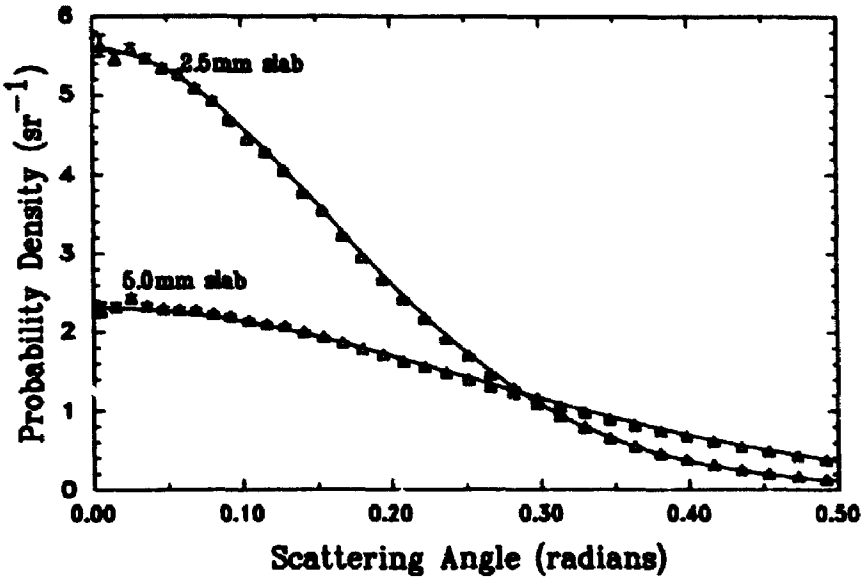

Figure 3-5: Angular Scattering of 5 MeV Electrons in Water Slabs

The figure shows the angular distribution of 5 MeV electrons passing through a 2.5 mm water slab and a 5.0 mm water slab. The solid lines represent the summation of 500 terms in the series (3.5). The triangles represent EGS4 simulations using the user-code, 'FOIL" (ESTEPE is 1.0%, AE is 0.911 MeV).

These comparisons indicate that the CPP formulation gives an accurate description of the angular scattering process for the slab thicknesses and electron energies investigated thus far. However, the theory does break-down for sufficiently large slab thicknesses and low incident electron energies. Figure 3-6 shows the case of 5 MeV electrons incident on a 1.0 cm thick water slab. In this case, the CPP calculation significantly over-estimates the amount of angular scattering. Three factors lead to the deviation of the theoretical result from the Monte Carlo simulation:

(i) Although the energy-loss correction on page 65 accounts for the **average** energy-loss, energy-loss **straggling** increases with slab thickness

(ii) The path length correction ((3.13)) is accurate only for relatively small path lengths and it becomes more inaccurate as the scattering angles increase.

(iii) The number of electrons transmitted through the foil decreases with increasing slab thickness (in Figure 3-6, only 94% of the electrons are transmitted in the

Monte Carlo simulation). The application of the CPP model to scattering in a slab of material does not account for back-scattering of electrons since it assumes 100% forward transmission. Renormalization of the distribution to compensate for the loss of back-scattered electrons is possible but an *a priori* knowledge of the fraction of back-scattered electrons is required. The possibility of renormalization has not been pursued here.

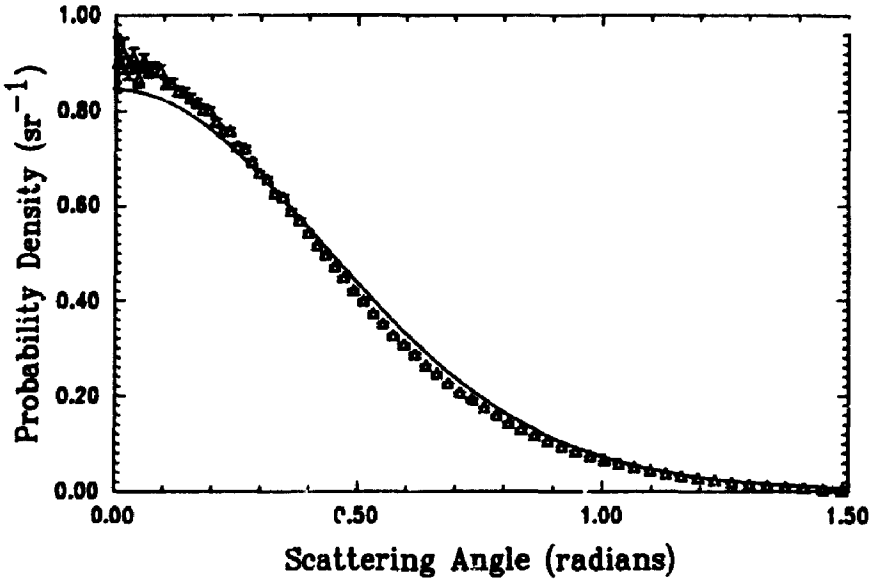

Figure 3-6: Angular Scattering in a Thick Water Slab

The figure shows the angular distribution of 5 MeV electrons scattered in a 1.0 cm thick water slab. The solid line represents the summation of 500 terms in the series (3.5) while the triangles represent the EGS4 Monte Carlo simulation (ESTEPE is 1%, AE is 0.911 MeV).

3.5 Summary and Discussion

The energy-loss (Chapter 2) and angular scattering (Chapter 3) of electrons in tissue are the two most important factors influencing the shape of the dose distribution in electron beam radiation therapy. The previous chapter dealt with the energy-loss process while this chapter deals with the angular scattering process. As discussed in Section 3.2.3, the compound Poisson process unifies both processes in a single

mathematical formalism.

The CPP formulation of the angular scattering process relies on the three assumptions listed in Section 3.2.2. *ie*

(i) the scattering events are independent,

(ii) all scattering events are identically distributed, and

(iii) the number of events in a given path length is a Poisson random variable.

These assumptions are satisfied provided that the electron energy-loss is negligible over the path length considered. This fact may be understood as follows. Assumption (i) is satisfied in an unpolarized medium on the basis of physical arguments; there is no causal connection between the angular change in one scattering event and the angular change in any other scattering event. If the electron energy is the same in each scattering event, then the **differential** angular scattering cross section will be the same in each event and assumption (ii) will be satisfied. The same is also true of the **total** cross section. Thus, the *average* length of the free path between two successive collisions does not depend on which two collisions we choose. In this case, the number of collisions on any path length interval, $[s_0, s]$, must be a Poisson random variable (see page 365 of Papoulis, 1984) and assumption (iii) is satisfied.

Molière's theory and the Gaussian approximation are limiting cases of the CPP formulation. Thus, these descriptions of the angular scattering process make assumptions *beyond* the three assumptions listed above. Specifically, Molière's theory assumes that the cumulative angle of travel is small and his mathematical approach requires that the number of collisions be large (greater than 20). In addition to the assumption of small cumulative angles of travel, the Gaussian approximation assumes that the number of collisions approaches infinity as the size of individual scattering events becomes vanishingly small.

The independent variable (or variable of evolution) in the CPP formulation of angular scattering is path length. However, the straight-line distance of travel is a more relevant parameter for numerical dose calculations. The path length correction (3.13) provides an estimate of the path length travelled for a given straight-line distance.

However, this correction is only approximate and will fail for large distances.

The path length correction together with the neglect of energy-loss limit the CPP angular scattering formalism to small straight-line distances (or "transport steps"). The calculations presented above indicate that the CPP formalism is accurate for transport steps of up to 0.5 g/cm^2 in water equivalent media for an incident electron energy of 5 MeV. This upper limit on the transport step size will decrease as the electron energy decreases or as the atomic number of the scattering medium increases. As a rough estimate, the maximum step size will be proportional to the square of the incident electron kinetic energy and inversely proportional to the square of the atomic number of the scattering medium. For the situations encountered in the calculation of therapeutic dose distributions, an accurate description of the angular scattering process may be achieved with a reasonable (*ie* not too small) step size.

3.6 Conclusions

This chapter demonstrates that the compound Poisson formulation of angular scattering and the Goudsmit-Saunderson theory are equivalent mathematical descriptions of the angular scattering process. Given the single scattering cross section for a medium, the CPP formulation is exact aside from the neglect of electron energy-loss. Comparisons of the theory with measured data and Monte Carlo simulations shows excellent agreement for thin gold foils. The theory also provides an accurate description of angular scattering in water slabs for slab thicknesses up to 0.5 cm for an incident electron energy of 5 MeV.

3.7 An Aside: Interpretation of Scattering Power

The scattering power of a medium characterizes the rate at which electrons of a given kinetic energy increase their angular spread as they increase their path length. In analogy with the mass stopping power, the ICRU (1984a) defines the mass angular scattering power as,

$$\frac{T}{\rho} = \frac{1}{\rho}\frac{d\langle\theta^2\rangle_s}{ds} \qquad (3.14)$$

where ρ is the mass density of the scattering medium and $\langle\theta^2\rangle_s$ is the average of the square of the scattering angle with respect to the initial direction of travel for electrons which have travelled a path length, s. The CPP formulation of the angular scattering process provides interesting insights into the concept of mass angular scattering power.

3.7.1 Derivation of Scattering power

To begin, let us derive an expression for the mass angular scattering power from the definition (3.14) and the CPP formulation given by Equation (3.4). Since we are free to chose the orientation of our co-ordinate system, we will make the initial direction of travel coincident with the z-axis (*ie* $\Omega_0 = \boldsymbol{k}$). The average of θ^2 is then given by,

$$\begin{aligned}\langle\theta^2\rangle_s &= \int_{4\pi}\theta^2 f^k(s,\Omega\cdot\boldsymbol{k})\,d\Omega \\ &= 2\pi\int_0^{\pi}\theta^2 f^k(s,\cos\theta)\sin\theta\,d\theta\end{aligned} \qquad (3.15)$$

Using the definition of a derivative, the expression for the mass angular scattering power (3.14) becomes:

$$\frac{T}{\rho} = \frac{1}{\rho}\lim_{s\to 0}\left[\frac{\langle\theta^2\rangle_s - \langle\theta^2\rangle_0}{s}\right] \qquad (3.16)$$

The quantity $\langle\theta^2\rangle_0$ vanishes since the electrons have no angular spread at s=0.

Substituting the equation (3.15) in to this last expression yields,

$$\frac{T}{\rho} = \frac{1}{\rho} \lim_{s \to 0} \left[\frac{2\pi}{s} \int_0^{\pi} \theta^2 f^k(s, \cos\theta) \sin\theta d\theta \right] \qquad (3.17)$$

Using the CPP equation (3.4) and interchanging the order of summation and integration gives,

$$\frac{T}{\rho} = \frac{2\pi}{\rho} \lim_{s \to 0} \left[\frac{1}{s} \sum_{n=0}^{\infty} \frac{e^{-\lambda s}(\lambda s)^n}{n!} \int_0^{\pi} \theta^2 \omega^k(\cos\theta)^{*n} \sin\theta d\theta \right] \qquad (3.18)$$

Noting that the term with n=0 vanishes and calculating the limit, only the term with n=1 survives. The scattering power becomes, then, an average over the single-collision cross section:

$$\frac{T}{\rho} = \frac{2\pi N_{av}}{A} \int_0^{\pi} \theta^2 \frac{d\sigma(\theta)}{d\Omega} \sin\theta d\theta \qquad (3.19)$$

where $d\sigma/d\Omega$ is the differential angular scattering cross section, N_{av} is Avogadro's number and A is the atomic mass of the scattering medium. This last expression incorporates the fact that $\omega^k(\cos\theta)$ is just the normalized single scattering cross section (*ie* $\frac{1}{\sigma_{tot}} \cdot \frac{d\sigma}{d\Omega}$) and the average number of collisions per unit path length, λ, is just the total cross section for angular scattering, σ_{tot}, multiplied by the volume density of scattering targets (*ie* the number of nuclei per unit volume).

McParland (1989) used an expression identical to Equation (3.19) in his calculation of scattering power. Other reports (Rossi, 1952; ICRU 1972; ICRU 1984a) also use equation (3.19) but they apply the small angle approximation, $\sin\theta \approx \theta$, and restrict the upper limit of the integral to 1 radian. However, since the magnitude of the

differential angular scattering cross section is appreciable only for small scattering angles, the small angle approximation does not have much impact on the numerical value of the scattering power. It is important to note that the concept of scattering power does **not** rely on the small angle approximation since the expression for scattering power arises directly from the definition (3.14) and the CPP equation (3.4) without any further approximations.

3.7.2 Scattering Power and Gaussian Scattering

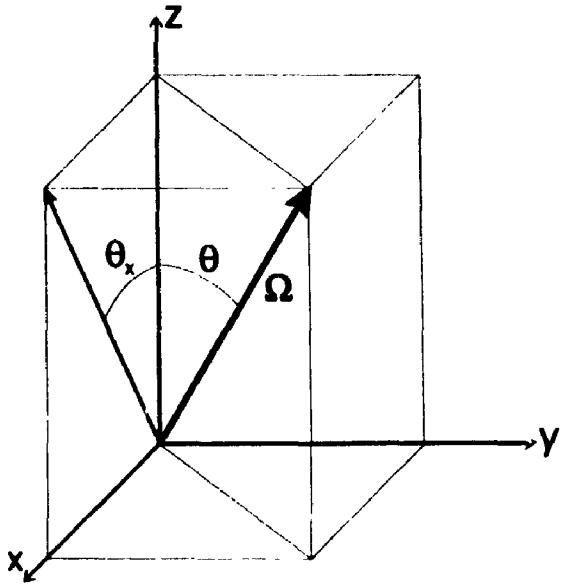

Figure 3-7: The Projected Angle of Travel

The diagram shows the direction vector, Ω, which forms an angle, θ, with the z-axis. The projection of Ω on the xz-plane makes an angle, θ_x, with the z-axis. An analogous angle, θ_y, may be defined for the projection of Ω on the yz-plane.

The mass angular scattering power is often associated with the Gaussian angular scattering approximation which assumes (i) that the angular distribution is a result of many small angle scattering events and (ii) that the cumulative angle of travel remains small. The association is so common that the ICRU (1984a) cautions that "the mass scattering power must be used with care for thin absorbers where single large-angle scattering events can be important." However, as noted in the previous section, the derivation of the scattering power expression (3.19) makes no assumption of small angles.

Moreover, the scattering power is defined in the limit of small path length (*ie* for an **infinitely thin** absorber). The ICRU's statement appears to be inconsistent with this fact and some clarification of the connection between scattering power and the Gaussian approximation seems warranted.

In the Gaussian approximation, the angular probability density is given by,

$$f_{Gauss}(z,\theta_x,\theta_y) = \frac{1}{2\pi\sigma_p^2}\exp\left[-\frac{\theta_x^2+\theta_y^2}{2\sigma_p^2}\right] \qquad (3.20)$$

where θ_x and θ_y are the projected angles defined in Figure 3-7 and σ_p^2 is the variance of the one dimensional projected distribution of electrons given by,

$$\sigma_p^2 = \langle\theta_x^2\rangle_z = \langle\theta_y^2\rangle_z = \int_{4\pi}\theta_x^2 f^k(z,\Omega\cdot k)\,d\Omega \qquad (3.21)$$

The path length, s, has been replaced by the depth in the scattering medium, z, since the two are interchangeable in the limit of small angles. The projected angle, θ_x, is related to the scattering angle, θ, by $\tan\theta_x = \tan\theta\cos\phi$ which becomes $\theta_x = \theta c \cdot \phi$ in the small angle approximation. Inserting this into the last expression, we find that $\langle\theta^2\rangle_z = 2\langle\theta_x^2\rangle_z$ and the Gaussian angular distribution becomes,

$$f_{Gauss}(z,\theta_x,\theta_y) = \frac{1}{\pi\langle\theta^2\rangle_z}\exp\left[-\frac{\theta_x^2+\theta_y^2}{\langle\theta^2\rangle_z}\right] \qquad (3.22)$$

where, to first order in z, the mean square angle of scatter is given by,

$$\langle\theta^2\rangle_z \approx \langle\theta^2\rangle_0 + \int_0^z \frac{T(u)}{\rho}\rho\,du \qquad (3.23)$$

This last expression assumes that the mass angular scattering power is a function of depth only (Eyges, 1948).

The Gaussian description of angular scattering given by equations (3.22) and

(3.23) will fail in two instances: (i) when the number of collisions is too small and (ii) when the cumulative angle of travel becomes too large. Although the Gaussian approximation breaks-down in these cases, it is important to note that the concept of scattering power is not limited by the Gaussian approximation. Therefore, ICRU's assertion that "the mass scattering power must be used with care for thin absorbers where single large-angle scattering events can be important" can be more precisely stated as, "the mass scattering power should not be applied to the Gaussian description of angular scattering when the number of scattering events is small."

Appendix 3A: Expansion of a Function on the Unit Sphere

Each point on the surface of a unit-radius sphere centred on the origin may be specified using a unit-length vector, Ω. Therefore, a function, $g(\Omega)$, is said to be a function on the unit sphere. Any continuous and finite function on the unit sphere may be expanded in terms of the spherical harmonics, $Y_{nm}(\Omega)$, as follows (Arfken, 1985):

$$g(\Omega) = \sum_{n=0}^{\infty} \sum_{m=-n}^{n} a_{nm} Y_{nm}(\Omega) \qquad \text{(A.1)}$$

where the expansion coefficients, a_{nm}, are given by,

$$a_{nm} = \int_{4\pi} g(\Omega)\, Y^{*}_{nm}(\Omega) d\Omega \qquad \text{(A.2)}$$

The superscript, "*", denotes the complex conjugate. This last expression follows from the orthogonality relation of the spherical harmonics,

$$\int_{4\pi} Y^{*}_{ij}(\Omega)\, Y_{nm}(\Omega) d\Omega = \begin{cases} 1 & \text{if } i=n,\ j=m \\ 0 & \text{otherwise} \end{cases} \qquad \text{(A.3)}$$

In the case of a function which is rotationally symmetric about the z-axis (*ie* $g(\Omega) = g(\theta)$ where θ is the angle with respect to the z-axis) all the terms except those with m=0 will be zero. The expansion may then be written,

$$g(\theta) = \sum_{n=0}^{\infty} \frac{2n+1}{4\pi} a_n P_n(\cos\theta) \qquad \text{(A.4)}$$

where $P_n(\cos\theta)$ are the Legendre polynomials (Arfken, 1985) and the expansion coefficients, a_n, are now given by,

$$a_n = 2\pi \int_0^{\pi} g(\theta) P_n(\cos\theta) \sin\theta d\theta \qquad \text{(A.5)}$$

The addition theorem for spherical harmonics (Arfken, 1985) allows the rotation of spherically symmetric functions. If two vectors, Ω_0 and Ω, form an angle α then the addition theorem states,

$$P_n(\cos\alpha) = \frac{4\pi}{2n+1} \sum_{m=-n}^{n} Y_{nm}(\Omega)\, Y^*_{nm}(\Omega_0) \qquad \text{(A.6)}$$

For instance, if we wish to rotate the function given by the expansion (A.4) such that the new axis of symmetry is the direction, Ω_0, we may apply the addition theorem to write the expansion as

$$g(\Omega \cdot \Omega_0) = \sum_{n=0}^{\infty} a_n \sum_{m=-n}^{n} Y_{nm}(\Omega)\, Y^*_{nm}(\Omega_0) \qquad \text{(A.7)}$$

Appendix 3B: The Screened Mott Cross Section

Using the first Born approximation, Mott (1929) derived a relativistically correct angular scattering cross section for the scattering of electrons from a point charge. The cross section takes the form of an infinite series but may be well approximated by (Evans, 1982),

$$\frac{d\sigma}{d\Omega} = \left[\frac{d\sigma}{d\Omega}\right]_R \left(1 - \beta^2 \sin^2\frac{\theta}{2} + \pi\beta\frac{Z}{137}(1 - \sin\frac{\theta}{2})\sin\frac{\theta}{2}\right) \qquad \text{(B.1)}$$

where $[d\sigma/d\Omega]_R$ is the Rutherford scattering cross section, β is the velocity of the electron as a fraction of the speed of light and Z is the atomic number of the scattering nucleus. The factor in the brackets, (...), on the right hand side acts as a relativistic correction to the Rutherford cross section and it is important only at large scattering angles.

The screening of the nucleus by the orbital electrons becomes an important effect at small scattering angles (*ie* large impact parameters). Therefore, the present work uses the screened Rutherford cross section in (B.1):

$$\left[\frac{d\sigma}{d\Omega}\right]_R = \frac{Z(Z+1)r_e^2}{4}\left(\frac{mc}{\beta p}\right)^2 \left(\sin^2\frac{\theta}{2} + \frac{\theta_s^2}{4}\right)^{-2} \qquad \text{(B.2)}$$

where p is the momentum of the incident electron, r_e is the classical electron radius, m is the electron mass and c is the speed of light in a vacuum. The factor $Z(Z+1)$ is used in place of Z^2 to account in an approximate way for the contribution of electron-electron collisions. The characteristic screening angle, θ_s, as calculated by Molière (see Bethe, 1953) is,

$$\theta_s^2 = \left(\frac{Z^{1/3}mc\,\alpha}{0.885p}\right)^2 (1.13 + 3.76(\frac{Z\alpha}{\beta})^2) \qquad \text{(B.3)}$$

where α is the fine structure constant.

Appendix 3C: Derivation of Equation (3.5)

This appendix demonstrates that the CPP Equation (3.4) leads directly to the equivalent expression (3.5). The derivation relies on the expansion of a function on the unit sphere as described in Appendix 3A. To begin, we require a relation between the expansion coefficients for the multiple scattering distribution and the expansion coefficients for the single-scattering distribution.

If the electrons travel initially along the z-axis (*ie* $\Omega_0 = \boldsymbol{k}$ where $\boldsymbol{k}$ is a unit vector lying along the z-axis) and θ denotes the scattering angle with respect to the z-axis, then the probability density for electrons scattered n times may be expressed in terms of an expansion in Legendre polynomials as follows (see Appendix 3A):

$$\omega^k(\Omega \cdot \boldsymbol{k})^{*n} = \omega^k(\cos\theta)^{*n} = \sum_{i=0}^{\infty} \frac{2i+1}{4\pi} a_i^{(n)} P_i(\cos\theta) \qquad \text{(C.1)}$$

where $P_i(\cos\theta)$ represents the Legendre polynomials (Arfken, 1985) and the expansion coefficients, $a_i^{(n)}$, are given by,

$$\begin{aligned} a_i^{(n)} &= \int_{4\pi} \omega^k(\Omega \cdot \boldsymbol{k})^{*n} P_i(\Omega \cdot \boldsymbol{k}) d\Omega \\ &= 2\pi \int_0^{\pi} \omega^k(\cos\theta)^{*n} P_i(\cos\theta) \sin\theta d\theta \end{aligned} \qquad \text{(C.2)}$$

Since $\omega^k(\cos\theta)^{*n}$ are normalized probability densities, the coefficients, $a_i^{(n)}$, represent averages of the Legendre polynomials, $\langle P_i(\cos\theta) \rangle_n$. The notation, $\langle \quad \rangle_n$, denotes a quantity averaged over the probability density for electrons scattered n times. The superscript "(n)" indicates that the expansion coefficients apply to the probability density for electrons scattered n times.

We may use the addition theorem for spherical harmonics (Appendix 3A) to write the expansion (C.1) for any arbitrary initial direction, Ω_0. *ie*

$$\omega^{\Omega_0}(\Omega\cdot\Omega_0)^{*n} = \sum_{i=0}^{\infty} a_i^{(n)} \sum_{j=-i}^{i} Y_{ij}(\Omega) Y_{ij}^{*}(\Omega_0) \tag{C.3}$$

where $Y_{ij}(\Omega)$ represent the spherical harmonics (Arfken, 1985) and the superscript "*" denotes the complex conjugate. Substituting (C.3) in the recursion relation (3.2) and using the orthogonality property of the spherical harmonics yields,

$$a_i^{(n)} = a_i^{(1)} a_i^{(n-1)} \tag{C.4}$$

This recursion relation for the expansion coefficients may be rewritten as,

$$a_i^{(n)} = \left(a_i^{(1)}\right)^n \tag{C.5}$$

In other words, the expansion coefficients of the n-scattered probability density are given simply by raising the coefficients for the single-scatter probability density to nth power[11]. This result will prove useful in deriving the series (3.5) from equation (3.4).

To derive Equation (3.5), we begin by substituting the expansion (C.3) in Equation (3.4):

$$f^{\Omega_0}(s,\Omega\cdot\Omega_0) = \sum_{n=0}^{\infty} \frac{(\lambda s)^n e^{-\lambda s}}{n!} \sum_{i=0}^{\infty} a_i^{(n)} \sum_{j=-i}^{i} Y_{ij}(\Omega) Y_{ij}^{*}(\Omega_0) \tag{C.6}$$

Interchanging the order of summation and applying the result (C.5) gives,

[11]This result is analogous to the familiar convolution theorem whereby Fourier transforming a convolution of two functions is equivalent to multiplying the Fourier transforms of the two functions.

$$f^{\Omega_0}(s,\Omega\cdot\Omega_0) =$$

$$\sum_{i=0}^{\infty}\sum_{j=-i}^{i} Y_{ij}(\Omega)Y_{ij}^{*}(\Omega_0)e^{-\lambda s}\sum_{n=0}^{\infty}\frac{(\lambda s a_i^{(1)})^n}{n!} \tag{C.7}$$

The last summation on the right hand side is the Taylor series expansion of $\exp(\lambda s a_i^{(1)})$. Therefore, the previous expression may be written,

$$f^{\Omega_0}(s,\Omega\cdot\Omega_0) =$$

$$\sum_{i=0}^{\infty}\exp(-\lambda s(1-a_i^{(1)}))\sum_{j=-i}^{i} Y_{ij}(\Omega)Y_{ij}^{*}(\Omega_0) \tag{C.8}$$

Applying the addition theorem for spherical harmonics, we obtain

$$f^{\Omega_0}(s,\Omega\cdot\Omega_0) =$$

$$\sum_{i=0}^{\infty}\frac{2i+1}{4\pi}\exp[-\lambda s(1-a_i^{(1)})]P_i(\Omega\cdot\Omega_0) \tag{C.9}$$

which is identical to Equation (3.5).

Chapter 4. Transport-Based Dose Calculations: The Monte Carlo and Evolution Methods[12]

4.1 Introduction

The previous two chapters presented models of electron energy-loss and of angular scattering. These were both based on a general statistical theory known as the compound Poisson process. However, we now require a means of applying these models to the calculation of electron beam dose distributions. As discussed in Chapter 1, two methods of transport calculations lend themselves to this task: the Monte Carlo method (Berger, 1963) and the evolution method (McLellan et al. 1992; Papiez et al., 1994; Janssen et al., 1994). The term "transport-based" is used to describe these two methods since they arrive at a dose distribution by providing a complete numerical solution of the transport problem (*ie* they provide the joint angle-position-energy distribution of electrons from which the dose distribution is derived rather than just the dose distribution directly).

The Monte Carlo method has long been applied to various problems in radiation dosimetry (Andreo, 1991). Recently, the increasing computational power available in typical radiation therapy departments has sparked interest in the use of the Monte Carlo method for routine treatment planning (DeMarco et al., 1994; Neuenschwander et al.,1995). Similarly, the evolution method benefits from computer advances and may also provide a computationally efficient basis for routine treatment planning. However, neither method is yet fast enough for routine clinical use on the computers typically available for clinical treatment planning. Therefore, the question arises: which method is the most computationally efficient?

The Monte Carlo method simulates many individual electron trajectories one at a time and uses the information gained to estimate the quantity of interest (in this case, the dose deposited in the patient). On the other hand, the evolution method simulates the

[12]Sections 4.1 and 4.2 of this chapter will be submitted to Medical Physics as "A comparison of the Monte Carlo and evolution methods of dose calculation: Theoretical considerations." The remainder of the chapter has already been published (see Papiez et al., 1994).

transport of an entire population of electrons; the angular scattering and energy-loss models are used to "evolve" the complete distribution of electrons from an initial state to a final state in which all the electrons have been stopped. Since the evolution method propagates all the electrons at once rather than one electron at a time, one would expect intuitively that the evolution method would be more efficient than the Monte Carlo method. However, this chapter demonstrates that, for problems involving several dimensions, this not necessarily the case.

This chapter analyzes the convergence of the Monte Carlo and evolution methods of dose calculation and comments on the relative merits of the two methods. A "dimensionally reduced" evolution method which uses the convergence properties of the evolution method to advantage is then introduced. The feasibility of the dimensionally reduced algorithm is demonstrated through calculations of two dimensional dose distributions in a water absorber exposed to 10 and 20 MeV beams of electrons.

4.2 Comparison of the Methods

4.2.1 Mathematical Connection

As discussed in Chapter 1, the basic equation underlying the evolution method is,

$$f_{i+1}(\boldsymbol{r}, \boldsymbol{\Omega}, E) = \int_D f_i(\boldsymbol{r}', \boldsymbol{\Omega}', E')\, G_{step}(\boldsymbol{r}, \boldsymbol{\Omega}, E; \boldsymbol{r}', \boldsymbol{\Omega}', E')\, d\boldsymbol{r}' d\boldsymbol{\Omega}' dE' \qquad (4.1)$$

where D represents the domain of all possible positions, directions, and energies. This equation "evolves" the joint density of electrons, $f_i(\boldsymbol{r}, \boldsymbol{\Omega}, E)$, a single transport step (from the i^{th} step to the $(i+1)^{th}$ step). A straightforward discretization of the six-dimensional space, $(\boldsymbol{r}, \boldsymbol{\Omega}, E)$, allows the integral to be performed numerically. In this approach, the probability density, $f_i(\boldsymbol{r}, \boldsymbol{\Omega}, E)$, is approximated using a **regularly spaced grid** of points. Iterative application of the numerical integration allows the transport of electrons in successive transport steps. The result of the calculation is a sequence of probability densities, $f_i(\boldsymbol{r}, \boldsymbol{\Omega}, E)$ for $i = 0, 1, 2, \ldots, N_{step}$, representing

the evolution of the ensemble of electrons with increasing transport step number. This procedure is represented schematically in Figure Figure 4-1.

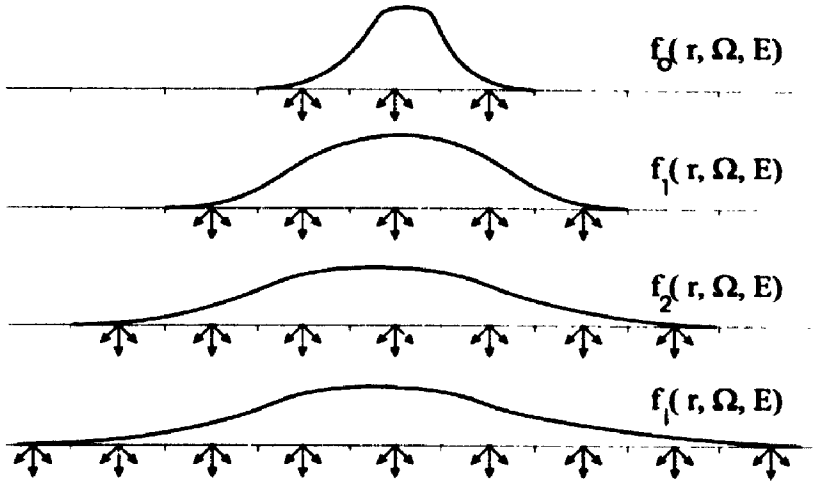

Figure 4-1: The Evolution Transport Calculation Method

The figure shows the evolution method schematically. An incident electron beam is transported in successive transport steps. At each transport step, the beam is spread-out according to an appropriate Green's function (or "kernel"). The full six-dimensional distribution of electrons is represented here as a one-dimensional curve for the purposes of illustration.

At first glance, the Monte Carlo method seems unrelated to the evolution method. However, consider the manner in which a condensed history or macro Monte Carlo scheme transports an electron:

1. The starting coordinates, $(\boldsymbol{r}_0, \Omega_0, E_0)$, are sampled from the probability density, $f_0(\boldsymbol{r}, \Omega, E)$.
2. The electron is transported one step by sampling the new coordinates, $(\boldsymbol{r}, \Omega, E)$, from the Green's function, $G_{step}(\boldsymbol{r}, \Omega, E; \boldsymbol{r}_0, \Omega_0, E_0)$.
3. Step 2 is repeated until the electron stops or leaves the calculation volume.

The result of the calculation is a sequence of points, $(\boldsymbol{r}_i, \Omega_i, E_i)$ for

$i = 0, 1, 2, \ldots, N_{step}$. The simulation of many histories generates a set of points for each transport step (for the ith transport step, the set of points may be denoted $\{(\boldsymbol{r}_i, \boldsymbol{\Omega}_i, E_i)_j, \; j = 1, 2, \ldots, N_{hist}\}$). This set serves to approximate the probability density, $f_i(\boldsymbol{r}, \boldsymbol{\Omega}, E)$ (this is discussed further in the next section). The result of a complete Monte Carlo simulation is a sequence of probability densities, $f_i(\boldsymbol{r}, \boldsymbol{\Omega}, E)$ for $i = 0, 1, 2, \ldots, N_{step}$, with each probability density represented by a set of **randomly sampled points** (*ie* an irregular grid). This procedure is shown schematically in Figure 4-2.

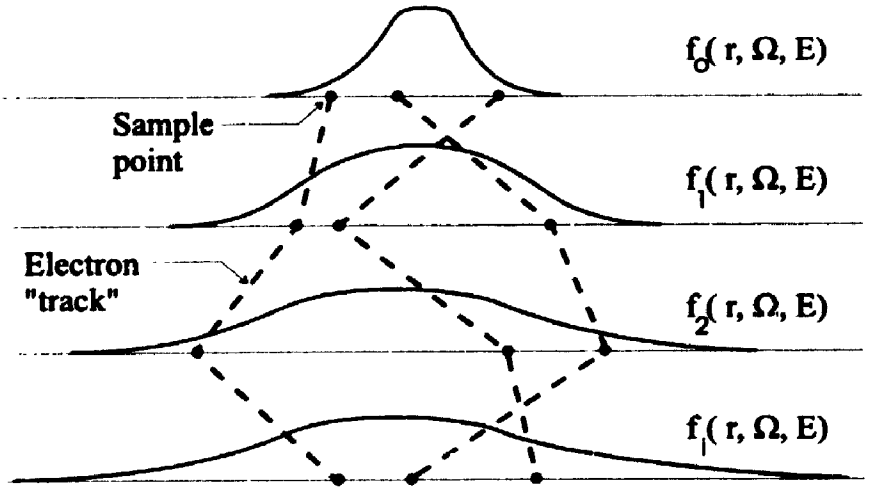

Figure 4-2: The "Evolutionary" Nature of the Monte Carlo Method

Each history in a Monte Carlo simulation generates a random sample of a probability density for every transport step in the history. Therefore, the simulation of many histories will generate a set of points associated with each transport step. The sequence of sets thus formed represents an "evolution" of the ensemble of incident electrons with increasing step number. The figure depicts three representative histories and, therefore, three sample points per transport step. Obviously, many more histories are required to achieve an accurate representation of the evolution of probability densities.

Both the Monte Carlo method and the evolution method solve the integral (1.9), (4.1) numerically for a sequence of probability densities, $f_i(\boldsymbol{r}, \boldsymbol{\Omega}, E)$ for $i = 0, 1, \ldots, N_{step}$. From a mathematical standpoint, the only difference between the

evolution and Monte Carlo methods is the manner in which they represent the probability densities, $f_i(\boldsymbol{r}, \boldsymbol{\Omega}, E)$. In the case of the evolution method, the probability density is approximated by a set of samples on a regularly spaced grid (one sample per grid-point). In the case of the Monte Carlo method, a set of randomly sampled points (one sample per history) may be used to reconstruct an approximation of the probability density. Thus, the total number of grid points in the evolution method is analogous to the total number of histories in the Monte Carlo method. The number of grid-points or histories required to achieve a given accuracy requires a knowledge of the convergence of the evolution and Monte Carlo methods.

4.2.2 Convergence in Monte Carlo

The previous section notes that the set of randomly sampled points, $\{(\boldsymbol{r}_i, \boldsymbol{\Omega}_i, E_i)_j \;,\quad j = 1, 2, \ldots, N_{hist}\}$, serves to approximate the probability density, $f_i(\boldsymbol{r}, \boldsymbol{\Omega}, E)$. Since this probability density represents the probability per unit volume, per unit solid angle, per unit energy of finding an electron at the point, $(\boldsymbol{r}, \boldsymbol{\Omega}, E)$, after the i^{th} transport step, an estimate of the probability density at any given point, $(\boldsymbol{r}, \boldsymbol{\Omega}, E)$, may be obtained from the expression,

$$f_i(\boldsymbol{r}, \boldsymbol{\Omega}, E) \approx \frac{1}{V_R} \cdot \frac{N_R}{N_{hist}} \qquad (4.2)$$

where V_R is the volume (in six dimensional phase space) of a small region, R, containing the point, $(\boldsymbol{r}, \boldsymbol{\Omega}, E)$, and N_R is the number of points in the set which lie in the region, R (termed a "scoring region"). This estimate of $f_i(\boldsymbol{r}, \boldsymbol{\Omega}, E)$ becomes exact in the limit that the number of histories, N_{hist}, becomes infinite while the volume of the region, V_R, shrinks to zero.

A practical Monte Carlo simulation cannot achieve an infinite number of histories or infinitely small scoring volumes, V_R. Thus, a Monte Carlo simulation provides only an estimate of the probability density, $f_i(\boldsymbol{r}, \boldsymbol{\Omega}, E)$, with some associated uncertainty. A consideration of this uncertainty will aid in an analysis of the computational efficiency

of the Monte Carlo method.

The number of electrons, N_R, arriving in the small region, R, after the i[th] transport step is a binomial random variable with the density,

$$Pr\{N_R = n\} = \frac{N_{hist}!}{n!\,(N_{hist}-n)!} P_R^n (1-P_R)^{N_{hist}-n} \qquad (4.3)$$

where P_R is the probability that an electron will arrive in the region, R, after the i[th] transport step ($P_R \approx N_R / N_{hist}$). Since N_R is a binomial random variable, its variance is given by $\sigma_{N_R}^2 = N_{hist} P_R (1-P_R)$ and this serves as a convenient estimate of the error in N_R. The error, $\Delta f_i(\boldsymbol{r}, \Omega, E)$, in the estimate of the probability density, $f_i(\boldsymbol{r}, \Omega, E)$, is then given by,

$$\Delta f_i(\boldsymbol{r}, \Omega, E) = \frac{1}{V_R} \cdot \frac{\sigma_{N_R}}{N_{hist}} = \frac{1}{V_R} \cdot \sqrt{\frac{P_R(1-P_R)}{N_{hist}}} \qquad (4.4)$$

This gives a relative error of,

$$\frac{\Delta f(\boldsymbol{r}, \Omega, E)}{f(\boldsymbol{r}, \Omega, E)} = \sqrt{\frac{1-P_R}{N_{hist} \cdot P_R}} \qquad (4.5)$$

where we have made the substitution, $P_R \approx N_R / N_{hist}$. This last expression shows that the error in the Monte Carlo simulation is inversely proportional to $\sqrt{N_{hist}}$ as is well known in practice. For example Neuenschwander et al. (1995) found empirically that the calculation time of their macro-Monte Carlo method was inversely proportional to the square of the uncertainty. Since the calculation time is also proportional to the number of simulated particles, their finding is consistent with the expression (4.5).

Note that the error (4.5) depends on the probability, P_R. This implies that the error in a Monte Carlo simulation depends on the fraction of the total number of histories reaching a given scoring region (as one would expect intuitively). In fact, the expression (4.5) implies that the error increases rapidly as P_R becomes small. Thus, a Monte Carlo

simulation provides fast convergence in a "high-probability region" (eg points within the beam's path) but provides poor convergence in "low-probability regions" (eg points well outside the primary beam).

4.2.3 Convergence in the Evolution Method

The evolution method of transport calculations described in Chapter 1 is essentially a six-dimensional numerical integration. The theory of numerical integration has been well studied and methods for its implementation on computers have been developed (Press et al., 1988). We require an expression relating the error in the discrete representation of a continuous integral and the number of bins used in the numerical integration.

Consider first the general problem of integrating a one-dimensional function, $F(u)$, from a lower limit, u_{min}, to an upper limit, u_{max}. The exact integral, I_{exact}, is given by,

$$I_{exact} = \int_{u_{min}}^{u_{max}} F(u)\,du \qquad (4.6)$$

Dividing the range of integration into N_{bins} discrete bins each of size Δu, the integral may be written,

$$I_{exact} = \sum_{i=1}^{N_{bins}} \int_{u_i-\Delta u/2}^{u_i+\Delta u/2} F(u)\,du \qquad (4.7)$$

where the points, u_i, represent the centres of the discrete bins. Expanding $F(u)$ in a Taylor series about the bin centres yields,

$$I_{exact} = \sum_{i=1}^{N_{bins}} \left[F(u_i)\,\Delta u + F''(u_i)\,\frac{\Delta u^3}{24} + \ldots \right] \qquad (4.8)$$

where $F''(u_i)$ represents the second derivative of $F(u)$ with respect to u evaluated at

the point, u_i. Compare this with the approximate numerical integral,

$$I_{approx} = \sum_{i=1}^{N_{bins}} F(u_i)\,\Delta u \qquad (4.9)$$

The relative error in the numerical integration may be defined by $\Delta I/I = (I_{exact}-I_{approx})/I_{exact}$. Considering terms up to second order in Δu and noting that $\Delta u = (u_{max}-u_{min})/N_{bins}$, the error in the numerical integration is given approximately by,

$$\frac{\Delta I}{I} = \frac{1}{N_{bins}^2}\cdot\frac{(u_{max}-u_{min})^2}{24}\sum_{i=1}^{N_{bins}}\frac{F''(u_i)}{F(u_i)} \qquad (4.10)$$

Therefore, in the case of a one-dimensional integration, the relative error is proportional to $1/N_{bins}^2$ where N_{bins} is the total number of bins used. For an integral of D dimensions, the discrete bins must be shared among the various dimensions and the error becomes $1/N_{bins}^{2/D}$. Therefore, the six-dimensional integral of the evolution method has a relative error proportional to $1/N_{bins}^{1/3}$.

4.2.4 Comparisons

A comparison of the convergence of the evolution and Monte Carlo methods indicates that the Monte Carlo method has a computational advantage over the evolution method. Consider a total number of samples, $N = N_{hist} = N_{bins}$, from the function, $f_i(\mathbf{r}, \Omega, E)$. The error in the evolution method is proportional to $1/N^{1/3}$. Compare this with an error proportional to $1/N^{1/2}$ in the Monte Carlo method. Assuming that the constant of proportionality is the same in each case, the error is a factor of $N^{1/6}$ smaller in the case of the Monte Carlo method (Figure 4-3). Of course, the constant of proportionality will not, in general, be the same and the relative convergence will depend

on: (i) the electron fluence in the region of interest (via the quantity P_R in equation (4.5)) and (ii) the "smoothness" of the function (via the quantity $F''(u_i)$ in equation (4.10)). The convergence of the evolution method relative to the Monte Carlo method improves in regions where the electron fluence is smooth (in all six dimensions) and the electron fluence is low. However, the shape of the curve in Figure 4-3 will remain the same.

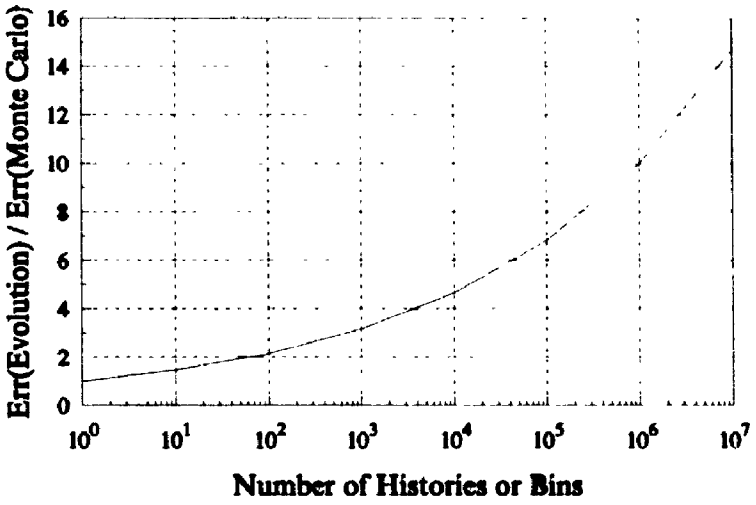

Figure 4-3: The Convergence of the Evolution and Monte Carlo Methods

The graph shows the relative rate of convergence for the evolution method and the Monte Carlo method. Since the evolution method is a six dimensional integral, the relative convergence is *proportional* to $N^{1/6}$. Although various factors (see text) will shift the curve up or down, the shape of the curve remains unaffected.

A comparison of the calculational speed of the Monte Carlo and evolution methods is more problematical than a consideration of their relative convergence since the calculational speed depends almost entirely on the details of the computer implementation. However, it is possible to draw some general conclusions. Note that the calculational speed of a particular method is distinct from the convergence; the convergence indicates the number of histories or bins required to achieve a given accuracy while the calculational speed indicates the time required to make a calculation with a given number of histories or bins.

In the case of the Monte Carlo method, the calculation time will simply be proportional to the number of histories simulated (N_{hist}). In the case of the evolution method, the relationship between the total number of bins, N_{bins}, and the calculation time is somewhat more complicated. The integral (1.9), (4.1) must be evaluated numerically to obtain a single point in the discrete representation of $f_{i+1}(\boldsymbol{r}, \boldsymbol{\Omega}, E)$. The time for one of these integrations is proportional to N_{bins}. In the worst case, a single source point, $(\boldsymbol{r}', \boldsymbol{\Omega}', E')$, can contribute to all destination points in phase space, $(\boldsymbol{r}, \boldsymbol{\Omega}, E)$, so that the integral must be evaluated a total of N_{bins} times. This leads to a total calculation time proportional to N_{bins}^2. In the best case, a source point, $(\boldsymbol{r}', \boldsymbol{\Omega}', E')$, can contribute only to a single destination point, $(\boldsymbol{r}, \boldsymbol{\Omega}, E)$. This would lead to a total calculation time proportional to N_{bins}. In reality, the true calculation time will lie between these two extremes so that the calculation time will be proportional to N_{bins}^{α} where α is a number in the range $(1,2)$.

Computational "over-head" is also important in a consideration of the speed of a particular numerical method. The evolution method can take advantage of the fact that calculations are performed on a regular grid to streamline the computer algorithm. For instance, coordinate transformations can be precalculated and stored in look-up tables (see for example Morawska-Kaczynska and Huizenga, 1992). Also, the spatial grid may be chosen such that interfaces in the scattering medium correspond to points on the discrete grid. The so-called "boundary-crossing" problem (as well as coordinate transformations) represent a very significant computational burden in the Monte Carlo method. Such considerations complicate the comparison of the calculational speed of the evolution and Monte Carlo methods.

Despite their close mathematical relationship, the computer implementations of the evolution method and Monte Carlo method differ significantly. The evolution method requires that the complete density, $f_i(\boldsymbol{r}, \boldsymbol{\Omega}, E)$, for the i^{th} transport step be known before the density, $f_{i+1}(\boldsymbol{r}, \boldsymbol{\Omega}, E)$, for the $(i+1)^{th}$ transport step can be calculated. Thus, the computer must store in memory (or on disk) the full discrete representation of

$f_i(\boldsymbol{r}, \boldsymbol{\Omega}, E)$. Assuming a modest 20 discrete bins per dimension, the total computer memory required is 244 MBytes (allowing for 4 bytes per floating point number). This is in addition to other data which must be stored for the calculation (*eg* CT data, pre-calculated Green's functions). By contrast, the Monte Carlo method tracks only one electron at a time and the computer must store only the current position, direction and energy of the electron (a total of only 24 bytes[13]) to calculate the coordinates for the next transport step. It should be noted, however, that the Green's functions, $G_{step}(\boldsymbol{r}, \boldsymbol{\Omega}, E; \boldsymbol{r}_0, \boldsymbol{\Omega}_0, E_0)$, can occupy a sizable amount of computer memory. To reduce the memory requirements, current implementations of the macro Monte Carlo method ignore the correlations between position, direction and energy for electrons emerging from the kugel (Ballinger, 1991; Neuenschwander, 1992).

4.3 A Dimensionally-Reduced Evolution Method[14]

4.3.1 Introduction

The above discussion indicates that, due to the large number of dimensions involved, the Monte Carlo method has a potential advantage over the evolution method for situations relevant to electron beam treatment planning. This section presents an approximate evolution method which reduces the number of dimensions involved in the numerical integration and reduces the computer memory requirements by using depth, rather than path length, as the variable of evolution. The reduced number of dimensions provides a significant gain in calculational speed. The improvement in memory requirements and gain in calculational efficiency is made at the expense of two assumptions: (i) electrons travel in straight lines within a single transport step, and (ii) electrons do not back-scatter (since depth is the variable of evolution). The purpose of this section is to establish the feasibility of such a method. At this point in the

[13]Even if the Monte Carlo simulation tracks secondary particles and must store the coordinates of, say, 10 particles, the total memory required is only 240 bytes.

[14]See Papiez et al. (1994)

implementation of the method, the computer code has not been optimized for calculational efficiency and only simplified models of electron energy loss and angular scattering have been used. Thus, quantitative timing comparisons with the Monte Carlo method have not been made.

4.3.2 Modification of the Green's Function

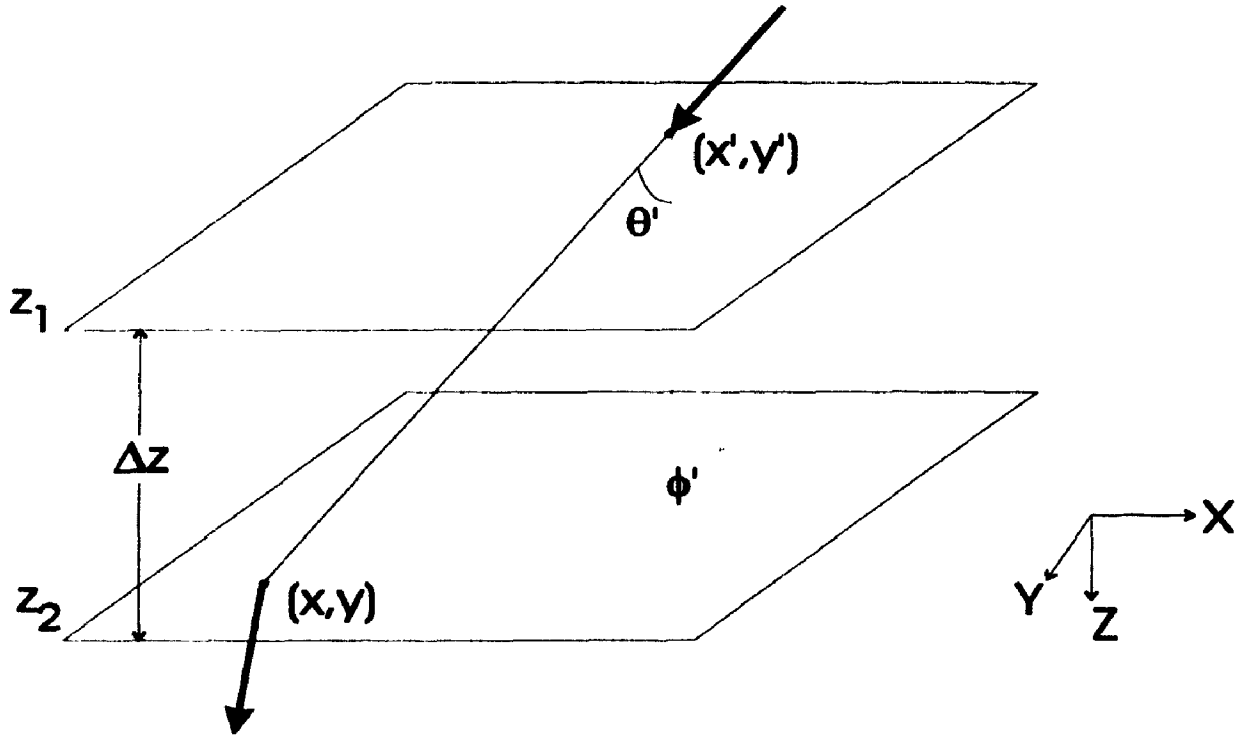

Figure 4-4: Geometry for Depth Evolution

The modified transport cheme assumes that electrons travel in straight lines over a small increment of depth. Therefore, an electron is projected along its initial direction of travel from one plane at depth, z_1, to the plane below at depth, z_2. Once the electron is projected to the lower plane, its direction of travel and energy is altered according to an appropriate Green's function. In this fashion, the complete distribution of electrons at depth, z_1, is transported to a depth, z_2. Using multiple depth increments, the distribution of electrons "evolves" from an incident surface distribution to any desired depth.

The first step in the development of the modified transport scheme is the construction of an appropriate Green's function. Figure 4-4 shows the modified transport scheme graphically. Two angles, θ and ϕ, specify the electron's direction of travel while

the lateral coordinates, (x, y), and the depth, z, specify the electron's position. A transport step is defined so that an electron travels in a straight line until it has increased its depth a specified amount, Δz. This scheme assumes that an electron which has a direction of travel greater than $\pi/2$ is absorbed locally in the scattering medium. In effect, this transport scheme evolves the electron distribution as a function of depth. Therefore, the depth, z, plays the role of the variable of evolution (*ie* depth is analogous to time in this model) rather than contributing to the dimensionality of the problem.

Since electrons are assumed to travel in straight lines, an electron leaving the position, (x, y), at a depth, z_1, will arrive at a new position given by, $(x + \Delta z \tan\theta' \cos\phi',\ y + \Delta z \tan\theta' \sin\phi')$, at depth $z_2 = z_1 + \Delta z$. Therefore, we approximate the Green's function governing the spatial redistribution of electrons as follows,

$$G_r(x, y; x', y', \theta', \phi') \approx \delta(x - x' - \Delta z \tan\theta' \cos\phi') \cdot \delta(y - y' - \Delta z \tan\theta' \sin\phi') \qquad (4.11)$$

where $\delta(\ldots)$ denotes Dirac's delta function. In reality, electrons do not follow straight lines and the error associated with the straight-line approximation is of the order Δz^2. This error constrains the size of the depth increments and forces the calculation to proceed only in small increments of depth.

The process of electron energy-loss was described in Chapter 2 which gives the probability density, $f^E(s, \Delta)$, for an electron of energy, E, to lose an amount of energy, Δ, in a path length, s. In the modified transport scheme presented here, the path length depends on the initial direction of travel and the size of the depth increment, Δz. *ie*

$$s = \Delta z \sqrt{1 + \tan^2\theta'}\ , \quad \theta' < \frac{\pi}{2} \qquad (4.12)$$

Thus, the Green's function describing the energy-loss process may be written, where the path length, s, is given by equation (4.12) and the energy change is given by

$$G_E(E;E',\theta') = f^{E'}(s,\Delta) \qquad (4.13)$$

$\Delta = E'-E$.

The angular scattering process has a similar dependence on path length and the Green's function describing the angular scattering process is,

$$G_\theta(\theta,\phi;\theta',\phi',E') = f^{\Omega'}(s,\Omega\cdot\Omega') \qquad (4.14)$$

The probability density, $f^{\Omega'}(s,\Omega\cdot\Omega')$, is discussed in Chapter 3. The dot product, $\Omega\cdot\Omega'$, may be expressed as follows:

$$\Omega\cdot\Omega' = \sin\theta\sin\theta'\cos(\phi-\phi') + \cos\theta\cos\theta' \qquad (4.15)$$

Assuming that the angular scattering and energy-loss processes are independent, the complete Green's function is a multiplication of the three component parts given above:

$$\begin{aligned} &G_{step}(\boldsymbol{r},\Omega,E;\boldsymbol{r}',\Omega',E') \\ &= G_{step}(x,y,\theta,\phi,E;\ x',y',\theta',\phi',E') \\ &= \delta(x-x'-\Delta z\tan\theta'\cos\phi')\cdot\delta(y-y'-\Delta z\tan\theta'\sin\phi')\cdot f^{E'}(s,\Delta)\cdot f^{\Omega'}(s,\Omega\cdot\Omega') \end{aligned} \qquad (4.16)$$

Inserting this expression into equation (1.9), (4.1) above yields,

$$\begin{aligned} &f_{i+1}(x,y,\theta,\phi,E) = \\ &\int_{\theta,\phi,E} f_i(x-\Delta z\tan\theta'\cos\phi', y-\Delta z\tan\theta'\sin\phi',\theta',\phi',E')\cdot \\ &\qquad f^{-'}(s,\Delta)\ f^{\Omega'}(s,\Omega\cdot\Omega')\,d\theta'd\phi'dE' \end{aligned} \qquad (4.17)$$

This approximate expression forms the basis for a modified evolution method. It allows electrons at a given depth, z_i, to be transported an increment of depth, Δz, to a new depth, $z_{i+1} = z_i + \Delta z$. Iterative application of the equation (4.17) allows the transport

of a beam of electrons from the surface of the scattering medium to any desired depth in increments of depth, Δz.

Due to the fashion in which the transport steps are defined, the distribution of electrons essentially evolves with depth rather than time or path length. Because depth now plays the role of the variable of evolution, the problem reduces to 5 dimensions rather than six (*ie* x, y, θ, ϕ and E) and the calculation time drops by a factor equal to the number of depth bins when compared with the full six-dimensional implementation.

4.3.3 Implementation in Two Spatial Dimensions

Mathematical Formulation

This section presents a simplified version of the modified transport scheme in which only two spatial dimensions are considered: depth, z, and lateral position, x. This two-dimensional version of the evolution method assumes that tissue inhomogeneities extend infinitely in the y-direction and it tracks only the projection of the electron motion on the xz-plane. Since this section aims only to establish the feasibility of the method, the current implementation uses simplified models of electron energy-loss and angular scattering. Specifically, the theory of Landau (1944) was chosen to describe the energy-loss of the electrons while the angular scattering was assumed to be Gaussian. The Gaussian approximation for the angular scattering of electrons was described in Chapter 3. Note that the choice of models made here was guided by the need for simplicity and the numerical method is not dependent on this particular choice.

Although the simplified geometry will aid in demonstrating the method, the two-dimensional nature of the calculations introduces one complication. Since the projection of an electron's path on a plane is always shorter than the true three dimensional path and the angular scattering and energy-loss processes are both path length dependent, a method to estimate the true length of the three dimensional path is required. Appendix 4A presents such a method.

In the two dimensional version of the evolution method, the distribution of electrons is described using the reduced set of coordinates, (x, θ_x, E), where θ_x represents the projection of the angle, θ, on the xz-plane. Equation (4.17) given in the previous section simplifies to,

$$f_{i+1}(x, \theta_x, E) =$$

$$\int_{E}^{E_{max}} \int_{-\pi/2}^{\pi/2} f_i(x-\Delta z \tan\theta'_x, \theta'_x, E')\ f^{E'}(s, E'-E)\ f^{\Omega'}(s, \theta'_x-\theta_x)\, d\theta'_x dE' \qquad (4.18)$$

In keeping with the Gaussian model of angular scattering, the angular transition density is expressed in terms of the difference, $\theta'_x-\theta_x$.

Numerical Calculations

To implement the transport scheme on a computer, the coordinate space, (x, θ_x, E), was organized into discrete bins, (x_j, θ_k, E_l), for $j = 1, \ldots, N_x$, $k = 1, \ldots, N_\theta$ and $l = 1, \ldots, N_E$. The discrete form of equation (4.18) is then,

$$f_{i+1}(x_j, \theta_k, E_l) =$$

$$\sum_{m=1}^{N_\theta} \sum_{n=1}^{N_E} f_i(x_j-\Delta z \tan\theta_m, \theta_m, E_n) \cdot \Delta G_\theta(\theta_k; \theta_m, E_n) \cdot \Delta G_E(E_l; E_n, \theta_m) \qquad (4.19)$$

where

$$\Delta G_\theta(\theta_k; \theta_m, E_n) = \int_{\theta_m-\Delta\theta/2}^{\theta_m+\Delta\theta/2} f^{\Omega'}(s, \theta'-\theta_k)\, d\theta' \qquad (4.20)$$

represents the probability for an electron to scatter from the mth angular bin to the angle, θ_k. Similarly,

$$\Delta G_E(E_l; E_n, \theta_m) = \int_{E_n-\Delta E/2}^{E_n+\Delta E/2} f^{E'}(s, E_n-E_l)\, dE' \qquad (4.21)$$

represents the probability for an electron to acquire an energy, E_l, at the end of a transport step given that it started in the n^{th} energy bin. The quantities, $\Delta\theta$ and ΔE, are, respectively, the sizes of the angular and energy bins.

Since the lateral point, $x-\Delta z \tan\theta_m$, does not necessarily lie on one of the discrete points, x_j, the function, $f_i(x-\Delta z \tan\theta_m, \theta_m, E_n)$, must be interpolated using the information from nearby discrete points. The function, $f_i(x-\Delta z \tan\theta_m, \theta_m, E_n)$, in equation (4.19) represents a linear interpolation between the two discrete points either side of $x-\Delta z \tan\theta_m$.

The discrete equation (4.19) was coded in VAX FORTRAN for the purpose of computer calculations. Calculations were performed on VAX 3200 and 4000 workstations under the VMS operating system as well as on SPARCstations II and 10 under the SunOS operating system. The "look-up tables", $\Delta G_\theta(\theta_k;\theta_m, E_n)$ and $\Delta G_E(E_l;E_n,\theta_m)$, were pre-calculated and stored on disk for use in subsequent transport calculations.

Dose Scoring

A careful accounting of the energy lost by the penetrating electrons yields the dose deposited in the scattering medium. To determine the dose deposited in absolute terms, it is necessary to determine the number of electrons incident on the scattering medium. The incident beam of electrons is represented by the discrete probability density, $f_0(x_j, \theta_k, E_l)$, which is normalized to satisfy the condition,

$$\sum_{j=1}^{N_x}\sum_{k=1}^{N_\theta}\sum_{l=1}^{N_E} f_0(x_j, \theta_k, E_l)\,\Delta x\,\Delta\theta\,\Delta E = 1 \qquad (4.22)$$

Since the two-dimensional implementation of the evolution method assumes that the beam extends infinitely and uniformly in the y-direction, the normalization condition implies that one electron per unit distance in the y-direction is incident upon the medium.

The number of electrons leaving the point, $(x_j-\Delta z\tan\theta_m, \theta_m, E_n)$, is $f_i(x_j-\Delta z \tan\theta_m, \theta_m, E_n)\,\Delta x\,\Delta\theta\,\Delta E\,\Delta y$ where Δy is an increment of distance in the

y-direction. The fraction of these electrons which arrive at their destination with energy, E_l, is $\Delta g_E(E_l; E_n, \theta_m)$ and each of these electrons deposits an amount of energy, $E_n - E_l$. Summing the contributions from all source points yields the total energy deposited:

$$E_{dep}(x_j, \frac{z_i+z_{i+1}}{2}) = \sum_{l=1}^{N_E} \sum_{m=1}^{N_\theta} \sum_{n=1}^{N_E} (E_n-E_l)\,\Delta G_E(E_l; E_n, \theta_m)\, f_i(x_j - \Delta z \tan\theta_m, \theta_m, E_n)\,\Delta x\,\Delta\theta\,\Delta E\,\Delta y \quad \textbf{(4.23)}$$

Notice that this assumes that all the energy is deposited at the point, $(x_j, \frac{z_i+z_{i+1}}{2})$.

The dose deposited is simply the energy deposited in a voxel divided by the mass of the voxel. *ie*

$$D(x_j, \frac{z_i+z_{i+1}}{2}) = \frac{E_{dep}(x_j, \frac{z_i+z_{i+1}}{2})}{\rho(x_j, \frac{z_i+z_{i+1}}{2})\,\Delta x\,\Delta y\,\Delta z} = \frac{\sum_{l=1}^{N_E} \sum_{m=1}^{N_\theta} \sum_{n=1}^{N_E} (E_n-E_l)\,\Delta G_E(E_l; E_n, \theta_m)\, f_i(x_j - \Delta z \tan\theta_m, \theta_m, E_n)\,\Delta\theta\,\Delta E}{\rho(x_j, \frac{z_i+z_{i+1}}{2})\,\Delta z} \quad \textbf{(4.24)}$$

where $\rho(...)$ is the mass density at the specified point. The calculation of dose adds very little to the computational burden since the energy deposited at each discrete point may be tallied "simultaneously" in the course of doing the transport calculation.

Monte Carlo Simulations

Monte Carlo simulations were performed using the EGS4 Monte Carlo code and its associated preprocessor, PEGS4. The user code XYZDOS was used to obtain the central axis depth dose and isodose data for comparison with the depth evolution method. As a consequence of the use of Landau's theory for electron energy-loss, the depth

evolution method neglected the energy lost to bremsstrahlung photons. Neither did the depth evolution method account for the transport of secondary electrons. Therefore, the Monte Carlo simulations took one of two forms: either a full simulation which included all electron interactions or, a modified calculation which suppressed the creation of bremsstrahlung radiation and deposited secondary electrons "on-the-spot". The modified Monte Carlo simulations necessitated two alterations. Firstly, the preprocessor, PEGS4, was altered (Sawchuk et al., 1992) to set the bremsstrahlung cross sections, the radiative branching ratio, and the radiative stopping power to zero. Secondly, the user code XYZDOS was altered to terminate secondary electrons as soon as they were created and deposit the associated energy at the point of creation. These modifications mimic the approximations inherent in the depth evolution method.

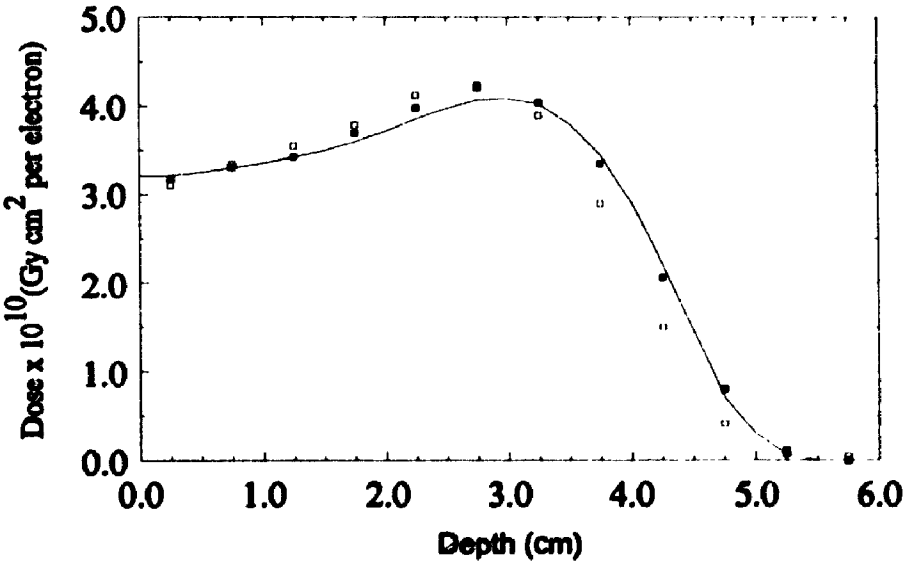

Figure 4-5: Depth Dose Curves for 10 MeV Electrons in Water

The figure compares the depth dose curve calculated using the depth evolution method (smooth curve) with the results of two Monte Carlo simulations: a full simulation (open squares) and a modified simulation (solid squares) in which bremsstrahlung is neglected and secondary electrons are deposited "on the spot".

For all Monte Carlo calculations, one million histories were simulated and the dose scored throughout a two-dimensional array of rods. The number of histories was sufficient to achieve better than 1% statistical accuracy in the peak dose region. Each

primary electron was followed until its kinetic energy fell below 10 keV (ECUT=521 keV) at which time it was considered to be locally absorbed. In the unmodified Monte Carlo calculations, secondary electrons and bremsstrahlung photons were set in motion and transported provided that their kinetic energy was above 10 keV (AE=521 keV, AP=10 keV). Photon histories were terminated if their kinetic energy fell below 100 keV (PCUT=100 keV).

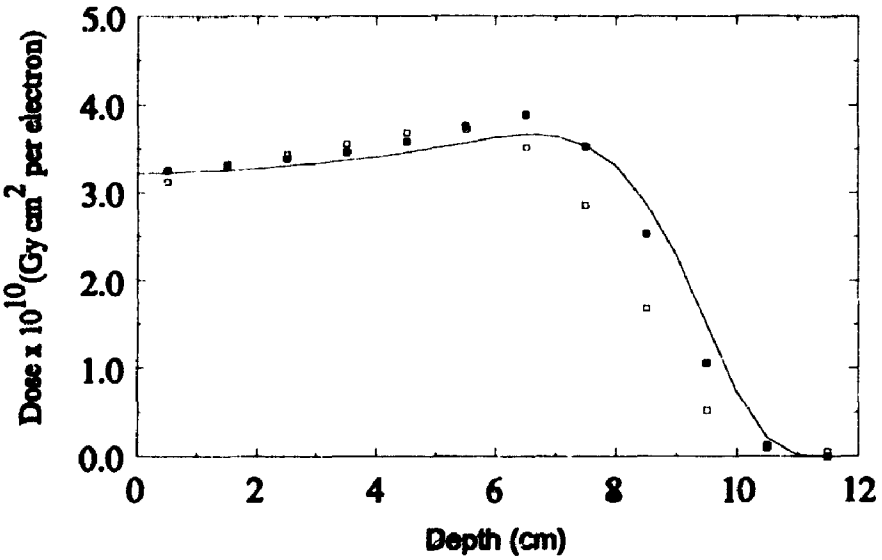

Figure 4-6: Depth Dose Curves for 20 MeV Electrons in Water
Same as Figure 4-5 but for 20 MeV electrons.

4.3.4 Results and Discussion

Figure 4-5 shows the depth dose curves for 10 MeV electrons incident on a water equivalent scattering medium. The field size was 10x10 cm^2 and the electrons were monoenergetic and incident normally on the surface of the scattering medium. The figure shows the results of the depth evolution method, the full Monte Carlo simulation, and the modified Monte Carlo simulation. Figure 4-6 shows the same comparison for 20 MeV electrons. In both cases, the number of angular bins, N_θ, was 31, the lateral increment size was 0.25 cm, and the depth increment size was 0.5 cm. The number of energy bins was 50 for the 10 MeV case and 100 for the 20 MeV case. All curves are displayed in dimensions of dose per unit incident fluence.

Due to the neglect of bremsstrahlung energy-loss, the depth evolution method over-estimates the penetration of the electrons when compared with the full Monte Carlo simulation. In addition, the depth evolution method over-estimates the depth of dose maximum. However, the agreement with the modified Monte Carlo calculations is markedly improved. Aside from a slight under-estimate of the dose at depth maximum, the depth evolution method agrees reasonably well with the modified Monte Carlo results.

Recall that the depth evolution method assumes (i) that electrons travel in straight lines within a single transport step and (ii) that electrons do not back-scatter. The agreement observed between the depth evolution method and the modified Monte Carlo simulations indicates that these assumptions do not cause serious errors in the calculation of depth dose distributions in a homogeneous absorber.

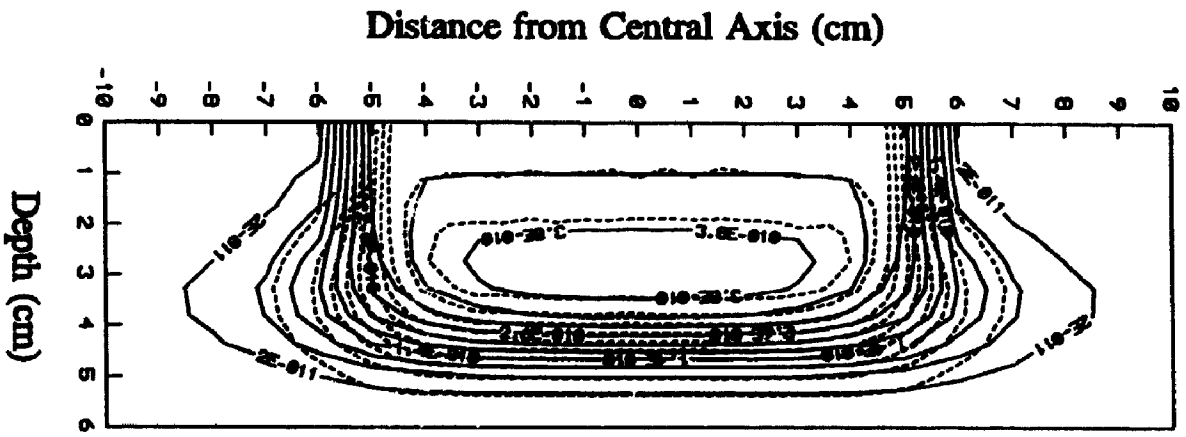

Figure 4-7: Isodose curves for 10 MeV Electrons in Water

The isodose distribution calculated using the depth evolution method (solid lines) is compared with the results of a modified Monte Carlo simulation (dashed lines) in which the energy lost to bremsstrahlung is neglected and secondary electrons are deposited "on the spot". The dose is displayed in units of Gy cm^2 / electron.

Figure 4-7 shows isodose distributions calculated using the evolution method as well as a modified Monte Carlo simulation. The incident 10x10 cm^2 beam consisted of 10 MeV monoenergetic and monodirectional electrons incident normally on the surface of the scattering medium. At all points near the central axis, the agreement between the

two data sets is very good. Discrepancies appear in the penumbra region especial beyond one half of the electron range. The depth evolution method over-estimates the width of the penumbra at the 10% isodose level by 8mm (*ie* the 4×10^{-11} Gy cm^2 isodose line). Several possible reasons for this discrepancy exist:

(1) The Gaussian approximation for the angular scattering used in the depth evolution method may over-estimate the angular spread of the electrons. This would lead to an increased penumbra width.

(2) In the depth evolution method, electrons arriving at a lateral point (which may not lie exactly on one of the discrete grid points) are placed in the two nearest discrete lateral points according to a linear weighting. This has the effect of causing a lateral spread of the electrons and this "grid diffusion" may contribute to the over-estimate of the beam penumbra width.

(3) As described above, the depth evolution method assumes that the energy lost by electrons travelling from a source point to a destination point is deposited at the destination point. In regions where lateral electron equilibrium does not exist (*eg* the penumbra), this dose deposition scheme causes a net lateral shift in the local dose deposition. This shift occurs in the predominant direction of electron travel.

The sources of error (1) and (3) listed above may be eliminated by appropriate modifications of the depth evolution method. In (1), an improved model of angular scattering, such as that described by Molière (1948), may be used in place of the Gaussian angular scattering model. In (3), the method of dose deposition may be modified to spread the energy uniformly between the source and destination points. The source of error (2), however, appears to be a fundamental limitation of the discrete representation of the electron distribution. It is worth noting, though, that "grid diffusion" also occurs in the discrete ordinates approach to transport calculations (Duderstadt and Martin, 1979) and in the transport calculations described by Janssen et al. (1994) and does not appear to cause any undue errors in dose calculation.

As yet, no rigorous timing comparisons of the evolution and Monte Carlo methods have been made. The dimensionally-reduced evolution method reduces the problem to five dimensions which still leaves the Monte Carlo method with a slight (theoretical)

advantage. Whether the high computational burden of the Monte Carlo method eliminates this advantage remains to be seen. As discussed in Chapter 5, the possibility exists to incorporate a higher order numerical integration scheme in the evolution method. Using such a method in all 5 dimensions would give the evolution method a relative convergence rate of $1/N^{4/5}$ which is somewhat better than the Monte Carlo method.

4.3.5 Conclusions

The results indicate that the dimensionally-reduced evolution method provides accurate predictions of the central axis depth dose when compared with the modified Monte Carlo calculations. Inclusion of radiative energy-losses is clearly needed to provide good agreement with the full Monte Carlo simulations. Discrepancies in the calculated dose distributions occur in the beam penumbra beyond a depth of half the electron range. These discrepancies may be due to the use of the Gaussian angular scattering approximation, grid diffusion, or assumptions in the method of dose scoring. Appropriate modifications of the calculational scheme will likely improve the calculated dose distribution.

The two assumptions of the dimensionally reduced evolution method -- namely (i) electrons travel in straight lines within a single transport step and (ii) electrons do not backscatter -- do not contribute to excessive errors in dose calculations for homogeneous, water-like media. The data suggest that this approach to electron beam dose calculations is feasible and worth pursuing.

Appendix 4A: Calculating Path Length in Three Dimensions

As mentixoned above, the projection of an electron's path on a plane is always shorter than the true three-dimensional path. This appendix presents a method of approximating the average length of the three-dimensional path given the length of the two-dimensional path and information regarding the angular spread of electrons.

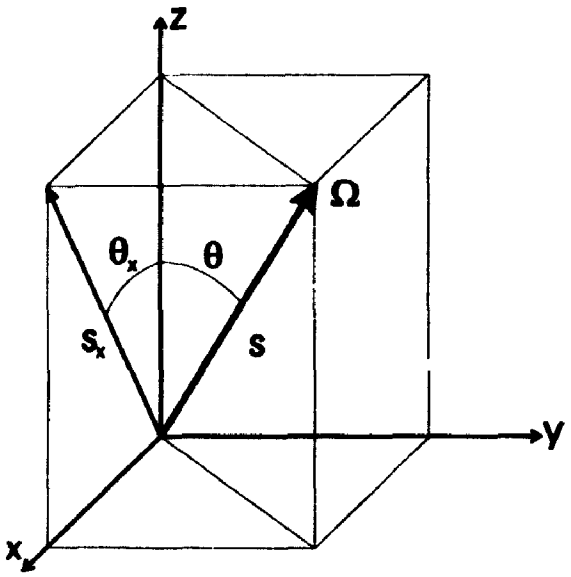

Figure 4-8: The Projected Path Length

A line segment of length, s, is projected onto the xz-plane to form a new line segment of length, s_x. Clearly, s_x is always less than or equal to s.

Based on the geometry shown in Figure 4-8, the true three-dimensional path length for an electron moving from depth z_i to depth z_{i+1} is given by,

$$s = \Delta z\sqrt{1+\tan^2\theta} = \Delta z\sqrt{1+\tan^2\theta_x+\tan^2\theta_y} \qquad \text{(A.1)}$$

The length of the projection of this path on the zx-plane is given by,

$$s_x = \Delta z \sqrt{1+\tan^2\theta_x} \qquad \text{(A.2)}$$

Applying the small angle approximation, these two expressions reduce to,

$$s = \Delta z \left(1 + \frac{\theta_x^2}{2} + \frac{\theta_y^2}{2}\right) \qquad \text{(A.3)}$$

and

$$s_x = \Delta z \left(1 + \frac{\theta_x^2}{2}\right) \qquad \text{(A.4)}$$

The difference between s and s_x is the increase in path length due to the excursion in the y-direction which is given by,

$$\begin{aligned} \Delta s_y &= s - s_x \\ &= \Delta z \frac{\theta_y^2}{2} \end{aligned} \qquad \text{(A.5)}$$

Taking averages of both sides and assuming $\langle\theta_x^2\rangle = \langle\theta_y^2\rangle$ yields,

$$\langle \Delta s_y \rangle = \frac{\Delta z}{2} \cdot \langle\theta_x^2\rangle \qquad \text{(A.6)}$$

The increase in path length due to excursions in the y-direction may be estimated using this last expression. The resulting approximate path length, $s \approx s_x + \langle \Delta s_y \rangle$, is used in all table look-ups of the angular and energy transition densities.

Chapter 5. Discussion and Conclusion

5.1 The Present Work

5.1.1 Summary

Chapter 1 discussed the shortcomings of the electron beam dose calculation methods currently in clinical use. These methods are semi-empirical in nature and can fail in some situations encountered in clinical dose calculations (*eg* in the presence of small tissue inhomogeneities). The premise of this thesis is that a more accurate dose calculation method -- one that is applicable to all situations encountered in clinical practice -- must incorporate the major physical processes which shape the dose distribution.

The two most important physical processes which drive the transport of electrons in a scattering medium are energy-loss and angular scattering. Chapters 2 and 3 address these two processes by developing a mathematical model which predicts the energy spectrum and angular spread of electrons which have travelled a given path length in a scattering medium. This mathematical model is based on the compound Poisson process and its applicability to situations relevant to clinical dose calculations is demonstrated.

Two "transport-based" dose calculation methods (*ie* methods which include the major physical processes) have been proposed for clinical use: the evolution method and the Monte Carlo method. Chapter 4 analyzes these two approaches and compares their numerical convergence. Chapter 4 also presents an approximate evolution method which incorporates two simplifying assumptions:

(i) electrons travel in straight lines over a single transport step, and
(ii) electrons do not backscatter.

The approximate method is intended to reduce the calculation time and computer memory requirements in comparison with the "exact" evolution transport method. The effects of these two assumptions on the accuracy of dose calculations are investigated using a two-

dimensional dose calculation algorithm.

5.1.2 Conclusions

The major conclusions of the previous four chapters may be summarized as follows:

(1) Commonly used models of energy-loss and angular scattering may be described using a single statistical model known as the "compound Poisson process".

The compound Poisson process (CPP) underlies many commonly used models of electron energy-loss (Landau, 1944; Vavilov, 1957; Bichsel and Saxon, 1975) and angular scattering (Goudsmit and Saunderson, 1940; Molière, 1948; Lewis, 1950). The CPP in turn relies on three basic assumptions:

(i) energy-loss or angular scattering events are independent,

(ii) all events are identically distributed (*ie* the cross sections do not change along the electron's path), and

(iii) the number of events in a given path length is a Poisson distributed random variable.

The effect of these three assumptions is to impose an upper limit of the allowable path length. The results of Chapters 2 and 3 indicate that, for water-like media, the upper limit of path length is approximately 0.5 g/cm^2.

(2) The macro Monte Carlo method and evolution method are both numerical methods of solving the same integral.

The basic equation underlying both the macro Monte Carlo method and evolution method is,

$$f_{i+1}(\boldsymbol{r}, \boldsymbol{\Omega}, E) =$$
$$\int_D f_i(\boldsymbol{r}', \boldsymbol{\Omega}', E')\, G_{step}(\boldsymbol{r}, \boldsymbol{\Omega}, E; \boldsymbol{r}', \boldsymbol{\Omega}', E')\, d\boldsymbol{r}' d\boldsymbol{\Omega}' dE' \qquad (5.1)$$

where $G_{step}(\boldsymbol{r}, \boldsymbol{\Omega}, E; \boldsymbol{r}', \boldsymbol{\Omega}', E')$ is the Green's function which gives the probability density of arriving at position, $\boldsymbol{r}$, direction, $\boldsymbol{\Omega}$, and energy, E, in one transport step given that the electron started at position, $\boldsymbol{r}'$, direction, $\boldsymbol{\Omega}'$, and energy, E'. The probability density, $f_i(\boldsymbol{r}, \boldsymbol{\Omega}, E)$, represents the ensemble of penetrating electrons after the i^{th} transport step ($f_0(\boldsymbol{r}, \boldsymbol{\Omega}, E)$ represents the incident electron beam) and D represents the domain of all possible positions, directions and energies. The Monte Carlo method and the evolution method differ only in the way they represent the probability density, $f_i(\boldsymbol{r}, \boldsymbol{\Omega}, E)$. The evolution method uses a regularly spaced grid of points while the Monte Carlo method uses a set of randomly sampled points. The total number of points, N_{bins}, in the regular grid is analogous to the total number of samples, N_{hist}, (*i.e.* the total number of histories) in the macro-Monte Carlo approach.

(3) The Monte Carlo method offers faster convergence than the evolution method for the full six-dimensional integral.

The convergence of the evolution method depends on the dimensionality of the integral while the Monte Carlo method does not. For a six-dimensional integral, the error in the evolution method is proportional to $1/N_{bins}^{1/3}$ compared to an error proportional to $1/N_{hist}^{1/2}$ for the Monte Carlo method. The convergence of the evolution method improves with decreasing dimensionality of the integral; specifically, the rate of convergence is proportional to $1/N^{2/D}$ where D is the dimensionality of the integral.

(4) The assumptions needed for a dimensionally-reduced evolution method do not cause excessive errors for the purposes of radiation therapy treatment planning.

A dimensionally-reduced evolution method may be formulated such that the

distribution of electrons evolves as a function of depth. The formulation relies on the two assumptions:

(i) electrons travel in straight lines within a transport step, and

(ii) electrons do not back-scatter.

Calculations of two-dimensional dose distributions indicate that these assumptions do not cause significant error in the calculated dose distributions. Also, the calculation time and memory requirements are reduced by a factor equal to the number of depth increments when compared with the full six-dimensional evolution method.

5.2 Future Research and Development

5.2.1 Generalization of Multiple Scattering Theory

The generalization of the models of energy-loss and angular scattering presented in Chapters 2 and 3 is unlikely to impact on the accuracy of dose calculations in a clinically significant way; the models used in the EGS4 (Nelson et al., 1985) and ETRAN (Berger, 1969) Monte Carlo codes both rely on the assumptions of the compound Poisson process yet they provide sufficiently accurate predictions for the purposes of clinical dose calculation. However, these Monte Carlo codes are known to give poor results in some problems (*eg* electron back-scattering calculations) due to the approximate nature of the multiple scattering and energy-loss formalisms. Therefore, the generalization of the multiple scattering theory merits serious attention in the solution of these types of problems.

Two approximations have been applied in Chapters 2 and 3. Firstly, the angular scattering and energy-loss processes are assumed to conform to the conditions of a compound Poisson process. Secondly, since the angular scattering and energy-loss processes have been treated separately, it is assumed implicitly that they are independent processes. Therefore, we may generalize the mathematical formalism on two levels: (i) remove the restrictions of the compound Poisson process, and (ii) include correlations between angular scattering and energy-loss.

The angle-energy correlations may be included within the framework of the

compound Poisson process. In other words, the generalization (ii) may be achieved without relaxing the conditions for a compound Poisson process. In analogy with the formalisms of Chapters 2 and 3, let $\omega_n(\Omega, E; \Omega_0, E_0)$ represent the probability density for an electron to acquire an angle, Ω, and an energy, E, after exactly n collisions, given that it started with an angle, Ω_0, and an energy, E_0. This probability density is defined by the recursive relation,

$$\omega_n(\Omega, E; \Omega_0, E_0) = \int_{all\ \Omega', E'} \omega_1(\Omega, E; \Omega', E') \cdot \omega_{n-1}(\Omega', E'; \Omega_0, E_0)\, d\Omega' dE' \tag{5.2}$$

where $\omega_1(\Omega, E; \Omega', E')$ is the probability density for a transition to the "state", (Ω, E), from an intermediate state, (Ω', E'), in a single interaction. This single-scattering probability density may be constructed from a normalized sum of the cross sections for the various possible modes of interaction:

$$\omega_1(\Omega, E; \Omega', E') = \frac{\sigma_{mol}(\Omega, E; \Omega', E') + \sigma_{nuc}(\Omega, E; \Omega', E') + \sigma_{brem}(\Omega, E; \Omega', E')}{\Sigma_{mol} + \Sigma_{nuc} + \Sigma_{brem}} \tag{5.3}$$

where Σ_{mol}, Σ_{nuc}, and Σ_{brem} are the **total** cross sections for Moller (electron-electron), nuclear (electron-nucleus), and bremsstrahlung interactions respectively. Similarly, $\sigma_{mol}(...)$, $\sigma_{nuc}(...)$, and $\sigma_{brem}(...)$ are the corresponding **differential** scattering cross sections (differential in both solid angle and energy). The probability density, $\omega_0(\Omega, E; \Omega_0, E_0)$, corresponding to no collisions (n=0) is the Dirac delta function, $\delta_\Omega(\Omega \cdot \Omega_0)\, \delta(E - E_0)$.

The conditions of the compound Poisson process imply that we can write the probability densities, $\omega_n(\Omega, E; \Omega_0, E_0)$, as a function of the difference, $\Delta = E_0 - E$, and the dot product, $\Omega \cdot \Omega_0$ (*ie* $\omega_n(\Omega, E; \Omega_0, E_0) = \omega_n(\Omega \cdot \Omega_0, \Delta)$). The joint angular-energy density for a given path length is then given by,

$$f(s,\Omega,E) = \sum_{n=0}^{\infty} \frac{(\lambda s)^n e^{-\lambda s}}{n!}\ \omega_n(\Omega\cdot\Omega_0,\Delta) \qquad (5.4)$$

where λ is the average number of collisions (of any type) per unit path length. Since the expression (5.4) uses cross sections which are differential in both energy and angle, the correlations between energy-loss and direction are retained.

The expression (5.4) is not useful when λs is large (*ie* when the path length is relatively large compared with the mean free path of the electrons) since the number of terms in the series required for accurate calculations becomes too large. Therefore, the next step in the procedure is to write the expression (5.4) in an alternate form suitable for relatively long path lengths as was done for the angular scattering and energy-loss processes (see Table 3-1 in Chapter 3).

A complete generalization of the multiple scattering process requires that we relax the conditions of the compound Poisson process. This may be achieved by replacing λs with $\int_0^s \lambda(s')\,ds'$ and by replacing $\omega_n(\Omega\cdot\Omega_0,\Delta)$ with $\omega_n(\Omega,E;\Omega_0,E_0)$ in the expression (5.4). With these substitutions, the methods used in Chapters 2 and 3 to derive the expressions for relatively long path lengths are no longer applicable. Thus, the challenge in deriving a more general scattering theory lies not in the actual formulation but in finding convenient expressions for incorporation into transport calculations. However, since a general scattering theory would not be restricted to a maximum path length increment, the challenge seems well worth the effort.

5.2.2 Timing Bench-marks

Results reported by Neuenschwander et al. (1995) and Janssen et al. (1994) afford a rough estimate of the relative calculational speed of the macro Monte Carlo method and the evolution method. Both papers report a speed gain over comparable EGS4 Monte Carlo calculations of about one order of magnitude indicating that the macro Monte Carlo method and the evolution method achieve comparable calculation times. Although this

result is not a rigorous timing bench-mark, it does suggest that, despite the advantage of faster convergence, the macro Monte Carlo method can not achieve dramatically shorter calculation times than the evolution method.

However, no quantitative comparisons of calculation times have appeared in the literature. Since any method of clinical dose calculation must be fast (*eg* <5 minutes per beam), timing "bench-marks" are essential to establish the practicality of a given method. Also, since the calculation time can vary with many factors (*eg* incident beam energy and the presence of inhomogeneities) time comparisons between two methods must be made under identical conditions. Therefore, a set of standard test cases would aid in the comparison of calculation times.

5.2.3 Cube-Based Macro Monte Carlo

Two practical considerations lead to an increased computational burden for the macro Monte Carlo method. Firstly, the kugel data-base is generated only for a single incident electron position and direction; to consider all possible incident positions and directions would generate an impractically large amount of data (Mackie and Battista, 1984). Secondly, the kugel data-base is generated only for homogeneous kugels.

The first limitation implies that the kugel data-base provides only the **change** in position, direction and energy over a given transport step. Thus, a coordinate transformation is required after each transport step to calculate the new position and direction of an electron given the position and direction immediately prior to the transport step. These coordinate transformations add to the time needed for a Monte Carlo simulation.

The second limitation implies that an electron should not cross a boundary between two dissimilar media in a single transport step. Thus, at every transport step, the calculational algorithm must check to see if a boundary has been crossed. If it has, then the algorithm must recalculate the transport step such that the step ends exactly on the boundary. The recalculation of steps near boundaries requires additional calculation time.

In contrast to the macro Monte Carlo method (as currently implemented), the evolution method requires neither coordinate transformations nor boundary crossing

algorithms. Since the distribution of electrons is represented using a regularly spaced grid, the position, direction and energy of an electron is determined by a set of six integers corresponding to the grid indices. Therefore, to change the position, direction and energy of an electron over a transport step requires only a shift of the grid indices. This shift requires far less computational effort than the coordinate transformation required in the macro Monte Carlo method. In addition, since the geometry of the scattering medium is obtained from computed tomography data (*ie* a three dimensional regularly spaced array of voxels), the calculational grid may be constructed such that medium boundaries coincide with discrete grid points. Such an arrangement precludes the possibility of crossing a boundary within a single transport step. Therefore, the discrete nature of the evolution method leads to a "stream-lined" numerical algorithm.

A dose calculation algorithm which combines the calculational simplicity of the evolution method with the faster convergence of the Monte Carlo method would provide shorter calculation times. Such an algorithm may be achieved by using cubes as kugels (as suggested by Mackie and Battista, 1984) rather than spheres or hemispheres as is done presently. To avoid coordinate transformations, the data base should be generated for all possible incident directions and positions. To avoid an excessively large data-base, the incident and exit positions of the electrons can be restricted to the corners of the cube. This is the approach taken by Janssen et al. (1994) in their evolution algorithm. The cube-based approach will also make it possible to avoid, *a priori*, the possibility of crossing a boundary within a transport step. The possibility of a cube-based macro Monte Carlo approach presents an exciting possibility for future development.

5.2.4 Generalization of the Depth Evolution Method

Chapter 4 demonstrated the feasibility of a depth evolution method of dose calculation for use in clinical treatment planning. However, several refinements of the method are required to achieve more accurate dose calculations.

Most importantly, better models of angular scattering and energy-loss (as described in Chapters 2 and 3) are needed to replace the overly simplistic models used in the

preliminary version of the algorithm. Inclusion of secondary electron and bremsstrahlung transport will further improve the accuracy.

One important assumption of the depth evolution method is that electrons do not back-scatter. This assumption may be relaxed somewhat by using a straight-line transport approximation for the backward-travelling electrons. In this approach, electrons which have acquired a polar angle of travel greater than $\pi/2$ radians are projected in a straight line for a distance equal to their residual range. The energy of these back-scattered electrons is spread uniformly along this line.

It is also important to establish the "robustness" of the depth evolution method. In other words, one must establish the limitations of the algorithm by finding situations in which the dose predictions are inaccurate or erroneous. For example, one weakness of the algorithm noted in Chapter 4 is the grid-diffusion problem. Electrons arriving at a given lateral point are placed in the discrete grid points closest to the true destination point. This has the effect of causing an artificial lateral spreading of the electrons. Further investigation is required to find the electron energy and material density for which this effect becomes unacceptably large.

Improving the calculation time will still be an important goal for the dimensionally reduced evolution method. Since the evolution method is simply a form of numerical integration, it seems reasonable to attempt to use more sophisticated numerical integration techniques to improve the rate of convergence and thereby improve the calculation time. Higher order numerical integration techniques such as Gaussian quadrature are well established (Press et al., 1988) and improve the convergence of a one-dimensional integral from $1/N_{bins}^2$ to $1/N_{bins}^4$.

Using Gaussian quadrature, the error in the five-dimensional integral of the depth evolution method would be proportional to $1/N_{bins}^{4/5}$ which is somewhat better than the convergence provided by the Monte Carlo method. Unfortunately, Gaussian quadrature requires that the discrete grid points be placed at the zeros of the Legendre polynomials and it remains to be seen if this would provide sufficiently small angular bins in the forward direction.

Whatever final form the depth evolution method may take, quantitative timing bench-marks remain an important requirement for the assessment of the practicality of the method. Although the depth evolution method will certainly improve upon the calculational speed of the full six-dimensional evolution method, its performance relative to the Monte Carlo method must also be assessed quantitatively.

5.2.5 Clinical Implementation

Chapter 4 presented depth-evolution results which tested the two basic approximations of the method: (i) electrons travel in straight lines within a given transport step, and (ii) electrons do not back-scatter. In this case, EGS4 Monte Carlo served as a suitable "gold standard" to isolate and test the approximations under idealized situations (*ie* "clean", monoenergetic, monodirectional beams incident on a homogeneous flat phantom). These types of comparisons were ideal for uncovering the weaknesses in the depth evolution method which were identified in Section 5.2.4. However, even once these weaknesses have been addressed, the depth evolution method must be compared with measured data obtained for clinically realistic situations.

Valid comparisons of the depth evolution method with data measured in clinically realistic situations first requires that the beam emerging from the medical linear accelerator be adequately modeled. Fortunately, considerable work has been done to calculate the distribution of electrons (in position, direction and energy) emerging from the electron applicator of a medical accelerator. Perhaps the most promising work has involved the use of the EGS4 Monte Carlo code to simulate all the components of the beam-shaping apparatus (Rogers et al., 1995). This provides a means to completely specify the properties of a clinical electron beam and use this information as input to a dose calculation. The depth evolution method can accept this input through appropriate specification of the initial conditions.

Once the questions of the numerical convergence of the evolution method and the modelling of the incident beam have been addressed, the validation of the depth evolution method in clinically realistic situations may proceed. The validation entails a careful

check of calculations against measurements for the many different situations of clinical interest. Complications encountered in the clinic can be broadly divided into two categories: (i) variations in the surface contour, and (ii) variations in the composition and geometry of inhomogeneities.

The variation of surface contour will present a particular challenge for the depth evolution method since, as noted above, the grid-diffusion problem will be exaggerated in low density media (*eg* the air space between the applicator and the patient surface). However, it seems reasonable to expect that pencil beam methods will be adequate to simulate the scattering of electrons in-air. One can envision, then, a hybrid method where a pencil beam calculation is used to bring the electrons from the level of the applicator to the patient's surface and the depth evolution method is used to calculate the electron transport thereafter.

The variation of the composition and geometry of inhomogeneities may be tested using standard test geometries which have been presented in the literature (Shui et al., 1992). However, it is also important to find test cases specific to a given method which probe its limitations. In the case of the depth evolution method, low density inhomogeneities will be of particular importance since the grid-diffusion problem will be most severe in these cases. The importance of grid diffusion will vary with the size and depth of the inhomogeneity. For example, small air cavities located near the end of the electron range (where the angular distribution of electrons is very broad) are unlikely to lead to significant errors. The same may not be true of large inhomogeneities located near the surface of the scattering medium. Therefore, experiments which vary the size and depth of inhomogeneities are required to probe the performance of the depth evolution method.

The geometry and scattering properties of the tissues is generally inferred from computed tomography data. It is well known that the CT number of a given voxel does not uniquely define the density and atomic number of the material within the voxel. However, approximate methods have been developed (Huizenga and Storchi, 1985) which are sufficiently accurate considering the uncertainty in the dose calculations themselves. Once more accurate methods of dose calculation become available, it seems prudent to

re-investigate the adequacy of methods used to translate between CT number and the scattering properties of a material.

As discussed in Chapter 1, the semi-empirical dose calculation methods in current clinical use do not provide sufficiently accurate dose predictions for all situations of interest. This has, to some extent, limited the applicability of electron beams to a few specific sites. However, with more accurate dose calculation techniques at their disposal and once assured of the accuracy of the dose predictions, medical physicists and radiation oncologists will be better able to develop more complex electron irradiation techniques and (hopefully) more effective treatments.

References

Altschuler MD, Bloch P, Buhle EL and Ayyalasomayajula S (1992) "3D dose calculations for electron and photon beams." Phys. Med. Biol. **37**: 391-411

Almond PR, Wright AE and Boone MLM (1967) "High energy electron dose perturbations in regions of tissue heterogeneity. Part II: Physical models of tissue heterogeneities." Radiology **88**: 1146-1153

Andreo P (1990) "Depth-dose and stopping power data for mono-energetic electron beams." Nuclear Instruments and Methods **B51**: 107-121

Andreo P (1991) "Monte Carlo techniques in medical radiation physics." Phys. Med. Biol. **36**: 861-920

Andreo P and Brahme A (1984) "Restricted energy-loss straggling and multiple scattering of electrons in mixed Monte Carlo procedures." Radiation Research **100**: 16-29

Arfken G (1985) Mathematical Methods for Physicists 3rd Edition (Academic Press, San Diego)

Bagne F (1976) "Electron beam treatment planning system." Med. Phys. **3**: 31-38

Ballinger CT (1991) "The response history Monte Carlo method for electron transport." PhD Thesis, University of California, Lawrence Livermore National Laboratory

Battista JJ and Sharpe MB (1992) "True three-dimensional dose computations for megavoltage x-ray therapy: A role for the superposition principle." Australasian Physical and Engineering Sciences in Medicine **15**: 159-178

Berger MJ (1963) "Monte Carlo calculation of the penetration and diffusion of fast charged particles." in Methods in Computational Physics Volume 1, edited by A Berni, S Fernbach and M Rotenberg (Academic Press, New York) pp 135-215

Berger MJ (1969) "ETRAN Monte Carlo code system for electron and photon transport through extended media." CCC=107 (Oak Ridge National Laboratory, Oak Ridge, Tenessee)

Berger MJ and Wang R (1988) "Multiple-scattering angular deflections and energy-loss straggling." in Monte Carlo Transport of Electron and Photons edited by TM Jenkins, WR Nelson and A Rindi (Plenum, New York)

Bethe HA (1953) "Molière's theory of multiple scattering." Physical Review **89**: 1256-1266

Bichsel H (1988) "Straggling in thin silicon detectors." Reviews in Modern Physics **60**: 663-699

Bichsel H and Saxon RP (1975) "Comparison of calculational methods for straggling in thin absorbers." Physical Review **A11**: 1286-1296

Bielajew AF (1994) "Plural and multiple small-angle scattering from a screened Rutherford cross section." Nuclear Instruments and Methods in Physics Research B **86**: 257-269

Bielajew AF, Wang R and Duane S (1993) "Incorporation of single elastic scattering in the EGS4 Monte Carlo code system: tests of Moliere theory" Nuclear Instruments and Methods in Physics Research B **82**: 503-512

Bielajew AF and Roger DWO (1986) "PRESTA: the parameter reduced electron-step transport algorithm for electron Monte Carlo transport." National Research Council of Canada, PIRS No. 042

Bluck O and Leisegang S (1950) "Zum energieverlust schneller elektronen in dunnen schichten." Z. Phys. **128**: 500-505

Boone MLM, Jardine JH, Wright AE and Tapley NV (1967) "High energy electron dose perturbations in regions of tissue heterogeneity. Part I: In vivo dosimetry." Radiology **88**: 1136-1145

Borsch-Supan W (1961) "On the evaluation of the function $\phi(\lambda) = \frac{1}{2\pi i}\int_{\sigma-i\infty}^{\sigma+i\infty} e^{u\ln u+\lambda u}du$ for real values of λ." Journal of Research of the National Bureau of Standards **B65**: 245-250

Brady LW, Simpson LD, Day JL and Tapley N (1992) "Clinical applications of electron-beam therapy." in Principles and Practice of Radiation Oncology Second Edition, Edited by CA Perez and LW Brady (J.B. Lippincott Company, Philidelphia)

Brahme A (1984) "Dosimetric precision requirements in radiation therapy." Acta Radiologica Oncology **23**: 379-391

Brahme A, Hulten G and Svensson H (1975) "Electron absorbed dose distribution for a 10 MeV clinical microtron." Phys. Med. Biol. **20**: 39-46

Brahme A, Kraepelien T and Svensson H (1980) "Electron and photon beams from a 50 MeV racetrack microtron." Acta Radiologica Oncol. **19**: 305-319

Brigham EO (1974) The Fast Fourier Transform (Prentice-Hall, Englewood Cliffs, NJ)

Bruinvis IAD, Van Amstel A, Elevelt AJ and Van der Laarse R (1983) "Calculation of electron beam dose distributions for arbitrarily shaped fields." Phys. Med. Biol. **28**: 667-683

Bruinvis IAD, Mathol WAF and Andreo P (1989) "Inclusion of electron range straggling in the Fermi-Eyges multiple scattering theory." Phys. Med. Biol. **34**: 491-507

Burman C, Kutcher GJ, Emami B and Goitein M (1991) "Fitting of normal tissue tolerance data to an analytic function." Int. J. Radiation Oncology Biol. Phys. **21**: 123-135

Cobb JH, Allison WWM and Bunch JN (1976) "The ionization loss of relativistic charged particles in thin gas samples and its use for charged particle identification." Nuclear Instruments and Methods **133**: 315-323

Cormack J and Shuter B (1991) "Computer generation of random deviates." Australasian Physical and Engineering Sciences in Medic. **14**: 86-96

Cygler J, Battista JJ, Scrimger JW, Mah E and Antolak J (1987) "Electron dose distributions in experimental phantoms: a comparison with 2D pencil beam calculations." Phys. Med. Biol. **32**: 1073-1086

DeMarco JJ, Solberg TD and Estes GP (1994) "An analysis of the Monte Carlo code MCNP as a radiotherapy treatment planning tool." Med. Phys. **21**: 884 (abstract)

Duderstadt JJ and Martin WR (1979) Transport Theory, (Wiley, New York)

Emami B, Lyman J, Brown A, Coia L, Goitein M, Munzenrider JE, Shank B, Solin LJ and Wesson M (1991) "Tolerance of normal tissue to therapeutic irradiation." Int. J. Radiation Oncology Biol. Phys. **21**: 109-122

Ermilova VC, Kotenko LP and Merzon GI (1977) "Fluctuations and the most probable values of relativistic charged particle energy loss in thin gas layers." Nuclear Instruments and Methods **145**:555-563

Evans RD (1982) The Atomic Nucleus, Reprint Edition (Krieger, Malabar, Florida)

Eyges L (1948) "Multiple scattering with energy loss." Phys. Rev. **74**: 1534-1535

Fano U (1963) "Penetration of protons, alpha particles, and mesons." Annual Reviews in Nuclear Science **13**: 1-66

Findlay DJS and Dusautoy AR (1980) "Improvements to the Blunck-Leisegang energy straggling distribution." Nuclear Instruments and Methods **174**: 531-533

Gikhman II, Skorochod AW and Yadrienko (1979) Teorio Vieroyatnostei i Matematicheskaya Statistika (Vischa Shkola, Kiev)

Gosselin M, Podgorsak EV, Evans MDC, Pla M and Shenouda G (1993) "A technique using parallel-opposed high energy electron beams for reirradiation of tumours near the spinal cord." Int. J. Radiation Oncol. Biol. Phys. **27**: 1207-1214

Goudsmit S and Saunderson JL (1940) "Multiple scattering of electrons." Physical Review **57**: 24-29

Hall G (1984) "Ionization energy losses of highly relativistic charged particles in thin silicon layers." Nuclear Instruments and Methods **220**: 356-362

Hanson AO, Lanzl LH, Lyman EM and Scott MB (1951) "Measurement of multiple scattering of 15.7 MeV electrons." Physical Review, **84**: 634-637

Hemmer PC and Farquhar IE (1968) "Multiple scattering in the Gaussian approximation: systematic improvement of the small-angle treatment." Physical Review **168**: 294-301

Hogstrom KR, Mills MD and Almond PR (1981) "Electron beam dose calculations." Phys. Med. Biol. **26**: 445-459

Holmes MA, Mackie TR, Sohn W, Reckwerdt PJ, Kinsella TJ, Bielajew AF and Rogers DWO (1993) "The application of correlated sampling to the computation of electron beam dose distributions in heterogeneous phantoms using the Monte Carlo method." Phys. Med. Biol. **38**: 675-688

Huizenga H and Storchi PRM (1985) "The use of computed tomography numbers in dose calculations for radiation therapy." Acta Radiologica Oncology **24**: 509-519

Huizenga H and Storchi PRM (1989) "Numerical calculation of energy deposition by broad high-energy electron beams." Phys. Med. Biol. **34**: 1371-1396

ICRU (1972) "Radiation Dosimetry: electrons with initial energies between 1 and 50 MeV." Report 21 of the International ommission on Radiation Units and Measurements, Washington DC

ICRU (1976) "Determination of absorbed dose in a patient irradiated by beams of X or gamma rays in radiotherapy procedures." Report 24 of the International Commission on Radiation Units and Measurements, Washington DC

ICRU (1984a) "Radiation dosimetry: electron beams with energies between 1 and 50 MeV." Report 35 of the International Commission on Radiation Units and Measurements, Bethesda, MD

ICRU (1984b) "Stopping powers for electrons and positrons." Report 37 of the International Commission on Radiation Units and Measurements, Bethesda, MD

Jackson JD (1962) Classical Electrodynamics (John Wiley & Sons, New York)

Janssen JJ, Riedeman DE, Morawska-Kaczynska M, Storchi PRM and Huizenga H (1994) "Numerical calculation of energy deposition by high-energy electron beams: III. three-dimensional heterogeneous media." Phys. Med. Biol. **39**: 1351-1366

Jette D, Pagnamenta A, Lanzl LH and Rozenfeld M (1983) "The application of multiple scattering theory to therapeutic electron dosimetry." Med. Phys. **10**: 141-146

Jette D (1985) "Second-order multiple-scattering theory for charged-particle teletherapy beams." Med. Phys. **12**: 178-182

. tte D and ielajew A (1989) "Electron dose calculation using multiple-scattering theory: second-order multiple-scattering theory." Med. Phys. **16**: 698-711

Jette D and Walker S (1992) "Incorporation of Moliere scattering theory into the Fermi-Eyges theory for electron dose calculations." Med. Phys. **19**: 792 (abstract)

Karlin S and Taylor HM (1981) A Second Course in Stochastic Processes (Academic Press, San Diego)

Karzmark CJ, Nunan CS and Tanabe E (1993) Medical Electron Accelerators (McGraw-Hill, New York)

Kellerer AM (1969) "Analysis of patterns of energy deposition: A survey of theoretical relations in microdosimetry." in Proceedings of the Second Symposium on Microdosimetry edited by HG Ebert (EURATOM, Brussels) pp 107-135

Kessaris ND (1966) "Penetration of high energy electron beams in water." Physical Review **145**: 164-174

Kessaris ND (1970) "Spectra of high energy electron beams in water." **43**: 281-287

Landau L (1944) "On the energy loss of fast charged particles." Journal of Physics **8**: 201-205

Laughlin JS (1965) "High energy electron treatment planning for inhomogeneities." Brit. J. Radiol. **38**: 143-147

Lax I (1986) "Inhomogeneity corrections in electron dose planning: limitations with the semi-infinite slab approximation." Phys. Med. Biol. **31**: 879-892

Lax I and Brahme A (1985) "Electron beam dose planning using Gaussian beams: energy and spatial scaling with inhomogeneities." Acta Radiologica Oncology **24**: 75-85

Lax I, Brahme A and Andreo P (1983) "Electron beam dose planning using Gaussian beams: improved radial dose profiles." Acta Radiologica **Supp 364**: 49-59

Lewis HW (1950) "Multiple scattering in an infinite medium." Physical Review **78**: 526-529

Lillicrap SC, Wilson P and Boag JW (1975) "Dose distributions in high energy electron beams: production of broad beam distributions from narrow beam data." Phys. Med. Biol. **20**: 30-38

Mackie TR (1987) "Calculating electron dose using a convolution/superposition method." in The Use of Computers in Radiation Therapy Edited by I.A.D. Bruinvis et al., (Elsevier Science Publishers B.V., North-Holland)

Mackie TR (1990) "Applications of the Monte Carlo method in radiotherapy." in The Dosimetry of Ionizing Radiation, Volume III ed KR Kase, BE Bjarngard and FH Attix (Academic Press, New York) pp 541-620

Mackie TR and Battista JJ (1984) "A macroscopic Monte Carlo method for electron beam dose calculations: a proposal." in The Use of Computers in Radiation Therapy (IEEE Computer Society Press, Silver Springs, Maryland)

Mah E, Antolak J, Scrimger JW and Battista JJ (1989) "Experimental evaluation of a 2D and 3D electron pencil beam algorithm." Phys. Med. Biol. **34**: 1179-1194

Malamut C, Rogers DWO and Bielajew AF (1991) "Calculation of water/air stopping power ratios using EGS4 with explicit treatment of electron-positron differences." Med. Phys. **18**: 1222-1228

Matthews JL, Findlay DJS and Owens RO (1981) "The distribution of electron energy losses in thin absorbers." Nuclear Instruments and Methods **180**: 573-579

McLellan J, Papiez LS, Sandison GA, Huda W and Therrien P (1992) "A numerical method for electron transport calculations." Phys. Med. Biol. **37**: 1109-1125

McLellan J, Sandison GA, Papiez L and Huda W (1991) "A restricted angular scattering model for electron penetration in dense media." Med. Phys. **18**: 1-6

McLellan J, Sawchuk S, Battista JJ, Sandison GA and Papiez LS (1994) "A method for the calculation of electron energy straggling spectra." Med. Phys. **21**: 367-378

McParland BJ (1989) "A derivation of the electron mass scattering power for electron dose calculations." Nuclear Instruments and Methods **A274**: 592-596

McParland BJ, Cunningham JR and Woo MK (1988) "The optimization of pencil beam widths for use in an electron pencil beam algorithm." Med. Phys. **15**: 489-497

Migdal AB (1956) "Bremsstrahlung and pair production in condensed media at high energies." Physical Review **103**: 1811-1820

Molière G (1947) "Theorie der streuung schneller geladener teilchen I: Einzelstreuung am abgeschirmten Coulomb-feld." Z. Naturforschg **2a**: 133-145

Molière G (1948) "Theorie der streuung schneller geladener teilchen II: Mehrfach- und vielfachstreuung." Z. Naturforschg **3a**: 78-97

Morawska-Kaczynska M and Huizenga H (1992) "Numerical calculation of energy deposition by broad high-energy electron beams: II. multi-layered geometry." Phys. Med. Biol. **37**: 2103-2116

Mott NF (1929) "The scattering of fast electrons by atomic nuclei." Proceedings of the Royal Society (London) **A124**: 425-442

Nelson WR, Hirayama H and Rogers DWO (1985) SLAC Report 265: The EGS4 Code System (Stanford University, Stanford, CA)

Neuenschwander H and Born E (1992) "A macro Monte Carlo method for electron beam dose calculation." Phys. Med. Biol. **37**: 107-125

Neuenschwander H, Mackie TR and Reckwerdt PJ (1995) "MMC - a high performance Monte Carlo code for electron beam treatment planning." Phys. Med. Biol. **40**: 543-574

Nigam BP, Sundaresan MK and Wu T-Y (1959) "Theory of multiple scattering: second Born approximation and corrections to Molière's work" Physical Review **115**: 491-502

Ning X (1994) "Multiple scattering of electrons as a compound Poisson process." PhD Thesis, Purdue University, *in preparation*

Ozdemir A, Shi-Ping Teng, Lindstrom DG and Anderson DW (1985) "Calculations for distributions in water for 10-MeV electrons." Radiation Research **101**: 213-224

Osman G (1976) "Dose distribution of therapeutic electron beams and automation of treatment planning." Journal of Medicine **7**: 143-167

Papiez LS, McLellan J, Sandison GA, Sawchuk SP and Battista JJ (1994) "Energy and pathlength straggling in a numerical method for electron dose calculations." Med. Phys. **21**: 1591-1598

Papiez LS and Sandison GA (1990) "A diffusion model with loss of particles." Advances in Applied Probability, **22**: 533-547

Papoulis A (1984) Probability, Random Variables, and Stochastic Processes (McGraw-Hill, New York)

Perry DJ and Holt JG (1980) "A model for calculating the effects of small inhomogeneities on electron beam dose distributions." Med. Phys. **7**: 207-215

Press WH, Flannery BP, Teukolshy SA and Vettering WT (1988) Numerical Recipes in C: The Art of Scientific Computing (Cambridge University, Cambridge)

Raeside DE (1976) "Monte Carlo principles and applications." Phys. Med. Biol. **21**: 181-197

Rhoades WA and Childs RL (1988) "The DORT two-dimensional discrete ordinates transport code." Nuclear Science and Engineering **99**: 88-89

Rhoades WA and Childs RL (1991) "TORT: a three dimensional discrete ordinates neutron/photon transport code." Nuclear Science and Engineering **99**: 88-89

Rogers DWO and Bielajew AF (1986) "Differences in electron depth-dose curves calculated with EGS and ETRAN and improved energy-range relationships." Med. Phys. **13**: 687-694

Rogers DWO and Bielajew AF (1988) "20-MeV electrons on a slab of water." in Monte Carlo Transport of Electron and Photons edited by TM Jenkins, WR Nelson and A Rindi (Plenum, New York)

Rogers DWO, Faddegon BA, Ding GX, Ma C-M, We J and Mackie TR (1995) "BEAM: A Monte Carlo code to simulate radiotherapy treatment units." Med. Phys. **22**: 503-524

Rossi B (1952) High Energy Particles, (Prentice-Hall, New Jersey) pp 69-71

Rossi B and Greissen K (1941) "Cosmic ray theory." Rev. Mod. Phys. **13**: 240-309

Rotondi A and Montagna P (1990) "Fast calculation of Vavilov distribution." Nuclear Instruments and Methods **B47**: 215-223

Sandison GA, Huda W, Savoie D and Battista JJ (1989) "Comparison of methods to determine electron pencil beam spread in tissue-equivalent media." Med. Phys. **16**: 881-888

Sandison GA and Papiez LS (1990) "Dose computation applications of the electron loss model." Phys. Med. Biol. **35**: 979-997

Sawchuk SP, McLellan J, Papiez LS, Sandison GA and Battista JJ (1992) "Alternative scoring and bremsstrahlung suppression techniques for use with the EGS4 Monte Carlo code." Med. Phys. **19**: 792 (abstract)

Schiff LI (1951) "Energy-angle distribution of thin target bremsstrahlung." Physical Review **83**: 252-253

Seltzer SM (1988) "An overview of ETRAN Monte Carlo methods." in Monte Carlo Transport of Electron and Photons edited by TM Jenkins, WR Nelson and A Rindi (Plenum, New York)

Shiu AS and Hogstrom KR (1991) "Pencil-beam redefinition algorithm for electron dose distributions." Med. Phys. **18**: 7-18

Shiu AS, Tung S, Hogstrom KR, Wong JW, Gerber RL, Harms WB, Purdy JA, Ten Haken RK, McShan DL, and Fraass BA (1992) "Verification data for electron beam dose algorithms." Med. Phys. **19**: 623-636

Shortt KR, Ross CK, Bielajew AF and Rogers DWO (1986) "Electron beam dose distributions near standard inhomogeneities." Phys. Med. Biol. **31**: 235-249

Shulek P, Golovin BM, Kulyukina LA, Medved SV and Pavlovich P (1966) "Fluctuations of ionization loss." Soviet Journal of Nuclear Physics **4**: 564-566

Storchi PRM and Huizenga H (1985) "On a numerical approach of the pencil beam model." Phys. Med. Biol. **30**: 467-473

Storchi PRM and Van der Linden RJ (1989) "A numerical method for the calculation of the diffusion of high energy electrons in a heterogeneous medium." Journal of Computational Physics **85**: 417-433

Svatos MM, Mackie TR, Hartmann-Siantar CL and Chandler WP (1994) "The macro response electron transport method." Med. Phys. **21**: 895 (abstract)

Tabata T and Ito R (1979) "Approximations to Landau's distribution functions for the ionization energy loss of fast electrons." Nuclear Instruments and Methods **158**: 521-523

Van Gasteren JJM (1987) "The influence of primary electron loss on the pencil beam width in the calculation of electron beam dose distributions." in The Use of Computers in Radiation Therapy Edited by I.A.D. Bruinvis et al., (Elsevier Science Publishers B.V., North-Holland)

Vavilov PV (1957) "Ionization losses of high-energy heavy particles." Journal of Experimental and Theoretical Physics USSR **32**: 920-923

Weinhous MS and Nath R (1984) "An improved energy-loss straggling algorithm for Monte Carlo transport codes." Med. Phys. **11**: 254-258

Werner BL (1985) "The perturbation of electron beam dose distributions at medium interfaces." Med. Phys. **12**: 745-763

Werner BL, Khan F and Deibel F (1982) "A model for calculating electron beam scattering in treatment planning." Med. Phys. **9**: 180-187

Werner BL, Walker S and Jette DA (1994) "How to choose AE in EGS4 Monte Carlo." Med. Phys. **21**: 894 (abstract)

Williams EJ (1929) "The straggling of beta particles." Proceeding of the Royal Society (London) **A125**: 420-445

Yu CX, Ge WS and Wong JW (1988) "A multiray model for calculating electron pencil beam distribution." Med. Phys. **15**: 662-671